THE DEVELOPMENT AND VALIDATION OF A QUALITY ASSURANCE PROGRAM FOR INTENSITY MODULATED RADIATION THERAPY

YOUSIF, YOUSIF A M

This thesis is submitted to comply with the requirements for the doctor of philosophy degree in Medical Physics, at the Faculty of Health Sciences, School of Medicine, Department of Radiation Oncology of The University of Pretoria, PRETORIA, South Africa.

Advisor: Prof. A. J. Van Rensburg

April 2012

Declaration by author

I declare that this thesis which I am submitting to the University of Pretoria for the doctorate degree in Medical Physics, represents my own work and has never been submitted by me to any other tertiary institution for any other degree

Signed in Pretoria

Yousif A M, Yousif

Support from Promoter

To whom it may concern

As supervisor of Mr. Yousif A M, Yousif, in his PhD studies in Medical Physics, I hereby declare that I support the submission of his thesis to the Faculty of Health Sciences.

Yours Sincerely,

Prof: Ado J van Rensburg

Date: April 2012

Director: Medical Physics
Department of Radiation Oncology
University of Pretoria

Dedication

This thesis is dedicated with love to my parents

Yousif. A. M. Yousif

ACKNOWLEDGEMENTS

Firstly I would like to thank God Almighty for the opportunity he has granted me, for the blessing and Mercy.

With a deep sense of gratitude, I would like to express my sincere thanks to my promoter Prof. A. J. van Rensburg for his expert guidance, advice, availability and interesting discussions during the research and revision of the thesis. He was always there for the help whenever I asked and whatever I asked for… your support is highly appreciated.

My gratefulness to all the staff members and colleagues in the Department of Radiation Oncology, Division of Medical Physics, Steve Biko Academic Hospital (formally Pretoria Academic Hospital)/ University of Pretoria for help directly or indirectly enabling the compilation of my thesis. I would like to thank Prof. J. Wilson who was the head of the Radiation Oncology Department (may her soul rest in a peace) for her support concerning evaluation of IMRT clinical plans. Special thanks to my research our research group at Steve Biko Academic Hospital.

I sincerely thank the radiographers at the Radiation Oncology Department for their co-operation, especially Mrs Zebeth Cronje the chief radiographer, Mrs Juanita Schoeman for the assistance in treatment planning system and help in LANTIS network in many aspects. Furthermore my sincere thanks to the students, interns and colleagues, at the Medical Physics Division, Steve Biko Academic Hospital/ University of Pretoria. Thanks for the support and kindness.

Pretoria offered me the chance to meet special people. I really enjoyed their company and the great time that we have spent together. Especially, Dr. DS Mshelia, my neighbour at Jabulani residence; thanks for helping me in language editing of the thesis, spending his time and being patient with me. I am grateful for his providing mentor support. I am extremely thankful to my friend Husam Ali for his advice and encouragement. I can't forget his support, kindness and humble personality. Also I would like to extend my warm gratitude to Dr. O Ali, for sharing your great knowledge in this field, helping in research and for good advice.

I would like also to thank Robert Poling, David Taleghani from Radiological Imaging Technology Company (RIT), Inc, for their help with the software and the analysis of EPID results. I would also like to acknowledge Ms Evelyn Tshehla for the English editing, help and great personality. Thanks to colleagues and friends for the support, Dr. Alfred, M. Al-Nagashi, A. Bashir, M. Ahmed, A. Elnour, M. Issa, S. Ibrahim and Sammy Nugud…

I also would like to thank the Ministry of Higher Education and Scientific Research, Sudan, for sponsoring me all the way. Furthermore special thanks are due to all my seniors and colleagues at Al-Neelain University-Khartoum-Sudan, for affording me the opportunity to complete my research in the Republic of South Africa. Not forgetting also to thank the University of Pretoria for the Postgraduate bursary.

Most importantly also, I extend my sincere and heartfelt thanks to my family for the underlying support and encouragement. I am thankful for the advice and encouragement.

Finally, I thank everyone else in or outside the department who contributed to making this research possible.

It is good to have an end to a journey, but it is the journey that matters in the end.

Contents

Declaration i

Support from promoter ii

Dedication iii

Acknowledgment iv

1. Introduction 1

1.1 Cancer treatment modalities 1

1.2 Conformal radiotherapy (CRT) 3

1.3 Intensity modulated radiation therapy (IMRT) 5

1.4 Patient-specific QA for IMRT 8

1.5 A novel use of IMRT 11

1.6 The aim of the study 12

1.7 Contribution of the study 13

2. The validation of a 2D-Array Seven29 ionization chamber for IMRT quality assurance 15

2.1 Introduction 15

2.2 Materials and methods 17

2.2.1 Calibration of the 2D-Array 20

2.2.1.1 Reference calibration 21

2.2.1.2 Absolute calibration 23

2.2.2 Reproducibility 24

2.2.3 Linearity and energy dependence 25

2.2.4 The output factor 25

2.2.5 Sensitivity 26

2.2.5.1 MLC movements 26

2.2.5.2 Leaf coverage 27

2.2.6 Clinical applications 28

2.3 Results and discussion 29

2.3.1 Calibration of the 2D-Array 30
2.3.1.1 Reference calibration 30
2.2.1.2 Absolute calibration 30
2.3.2 Reproducibility 30
2.3.3 Linearity and energy dependence 32
2.3.4 The output factor 33
2.3.5 Sensitivity 35
2.3.5.1 MLC movements 35
2.3.5.2 Leaf coverage 36
2.3.6 Clinical applications 37
2.4 Summary and conclusion 40

3.0 The dosimetric properties of an amorphous silicon electronic portal imaging device for IMRT verifications 42
3.1 Introduction 42
3.2. Materials and methods 44
3.2.1 Routine calibration of the a-Si EPID 46
3.2.2 Detector reproducibility 46
3.2.3 The a-Si EPID response as a function of applied monitor units 47
3.2.4 Field-size dependence 48
3.2.5 Dose-rate linearity 49
3.2.6 The ghosting effect of the a-Si EPID 49
3.2.7 The build-up effect of the a-Si EPID 50
3.2.8 The a-Si EPID response versus the thickness of solid water 50
3.2.9 An electronic portal imaging device as a dosimeter 51
3.2.9.1 Calibration of the EPID 51
3.2.9.2 The evaluation of the fluence maps measured with EPID 53
3.3 Results and discussion 54
3.3.1 The routine calibration of the a-Si EPID 54
3.3.2 Detector reproducibility 55
3.3.3 The a-Si EPID response as a function of applied monitor units 56

3.3.4 Field-size dependence 57
3.3.5 Dose-rate linearity 58
3.3.6 The ghosting effect of the a-Si EPID 59
3.3.7 The build-up effect of the a-Si EPID 63
3.3.8 The a-Si EPID response versus the thickness of solid water 64
3.3.9 An electronic portal imaging device as a dosimeter 67
3.3.9.1 Calibration of the EPID 67
3.3.9.2 The evaluation of the fluence maps measured with EPID 70
3.4 Conclusion 72

4. A comparative investigation of IMRT fluence maps measured with the Kodak EDR2 and 2D-Array Seven29 detection systems 74
4.1 Introduction 74
4.2 Materials and methods 75
4.2.1 IMRT delivery and fluence map generation 75
4.2.2 Kodak ERR2 film measurements 76
4.2.3 2D-Array measurements 79
4.2.4 IMRT dose matrix registration and analysis 80
4.2.5 Gamma evaluations and acceptance criteria 81
4.2.6 Testing the pass-rate criteria 81
4.3 Results and discussion 82
4.3.1 Kodak ERR2 film measurements 82
4.3.3 2D-Array measurements 91
4.3.4 Testing the pass-rate criteria 98
4.3.5 Kodak EDR2 film dosimetry versus 2D-Array dosimetry systems 103
4.4 Conclusion 105

5. The application of an amorphous silicon electronic portal imaging device for IMRT pre-treatment verification 108
5.1 Introduction 108
5.2 Materials and methods 109

5.2.1 IMRT dose maps 109
5.2.1.1 EPID dose maps 109
5.2.1.2 CMS XiO TPS dose maps 111
5.2.2 Dose-map comparison methods 112
5.3 Results and discussion 113
5.3.1 IMRT dose maps 114
5.3.2 Dose-map comparison methods 114
5.3.2.1 Isodose color wash 114
5.3.2.2 Gamma evaluations 117
5.3.2.3 Subtraction histogram 122
5.3.2.4 Relative dose profile 123
5.4 Conclusion 128

6. Absolute dosimetry and verification of the monitor units for intensity modulated radiation therapy 130
6.1 Introduction 130
6.2 Theory 131
6.3 Materials and methods 134
6.3.1 The IMRT plans used 134
6.3.2 Absolute dose measurements 134
6.3.3 The Monitor Unit Check Program (MUCP) 136
6.4 Results and discussion 138
6.4.1 The IMRT plans used 138
6.4.2 Absolute dose measurements 138
6.4.3 The Monitor Unit Check Program (MUCP) 139
6.4.3.1 Calculations of the MU_{avg} 139
6.4.3.2 Calculations of D_{target} 143
6.4.3.3 Dose verifications for the IMRT plans 143
6.5 Discussion and conclusion 144

7. Conclusions and future work 145

Summary **149**

References **152**

Abbreviations

IMRT	Intensity Modulated Radiation Therapy
MLC	Multileaf Collimator
CRT	Conformal Radiation Therapy
SPECT	Single-Photon-Emission-Computed Tomography
PET	Positron-Emitted Tomography
CT	Computed Tomography
MRI	Magnetic Resonance Imaging
2D	Two-Dimensional
3D	Three-Dimensional
TV	Target Volume
DVH	Dose Volume Histogram
MU	Monitor Units
SSD	Source to Surface Distance
OAR	Organ-At-Risk
TCP	Tumor Control Probability
NTCP	Normal Tissue Complications Probability
IGRT	Image-Guided Radiotherapy
TPS	Treatment Planning System
Linac	Linear Accelerator

1. Introduction

1.1 Cancer treatment modalities

Cancer has long plagued humankind; however, scientific attempts to understand the causation and epidemiology of this disease and the development of therapeutic approaches have only been made in the past hundred years. For centuries, cancer was merely viewed as a mass of tissue with the potential for uncontrolled growth and spread. Although a few cancers occur during childhood, over 90% of all cancers occur in adulthood, and their incidence rises sharply with advancing age. Adult cancers are often lifestyle related. The role of ionizing radiation, certain chemicals, tobacco and viruses in inducing malignant transformation has become well established through epidemiological in vitro and in vivo studies.

The detection and diagnosis of cancer is crucial to the successful treatment of the disease. The earlier a tumor is discovered, the lower the likelihood that it will spread to other parts of the body. Screening tests are performed to identify tumors in their earliest stages. When a tumor is suspected, a work-up, or series of diagnostic examinations, is initiated. The purpose of the work-up is to determine the general health status of the patient and to collect as much information about the tumor as possible (the type, location and size of the tumor; the extent to which the tumor has invaded normal tissues; the occurrence of spread to distant sites; and the involvement, if any, of the lymph nodes) to aid in the effective treatment of the patient. The assessment of a tumor must be confirmed using a variety of diagnostic procedures, such as computed tomography (CT) and magnetic resonance imaging (MRI). With the recent advancements in technology, more information is available to the physician than ever. Various diagnostic devices, such as CT, MRI, fluoroscopy, ultrasound, radiotherapy simulators and SPECT/PET-CT scanners, have proven to be useful in the information-gathering process and have improved the effectiveness of treatment.

The effective treatment of cancer patients involves a multimodal approach that combines surgery, radiation therapy, chemotherapy and hormonal therapy to produce optimal results with minimal toxicity. Radiation therapy is used both as a curative treatment and

as a palliative treatment to control symptoms or to improve quality of life if a cancer is too advanced to be cured. Radiation therapy treatments can be classified as external (teletherapy) or internal radiotherapy (brachytherapy); these classifications refer to the location of the source of radiation relative to the patient. In brachytherapy, the radioactive sources are either introduced inside of the body cavities using a technique called intracavitary or intraluminal radiotherapy, or the sources are inserted into the patient's tissue using a technique called interstitial radiotherapy (Williamson *et al.,* 1995). Radiation therapy can be performed with teletherapy or brachytherapy; in some radiation treatment protocols, both of these techniques are used.

Teletherapy uses linear accelerators (Linacs), Co-60 machines and kilovoltage machines (Karzmark and Pering, 1973; Karzmark 1984; Khan 2003), and brachytherapy utilizes small sealed sources of radioactive nuclides. The common sources of these nuclides are *cesium*-137, *iridium*-192 and *iodine*-125 (Podgorsak 2004; AAPM 1997). In teletherapy machines, radiation is also carried out with other types of accelerators in addition to Linacs, such as betatrons and microtrons. These accelerators produce protons, neutrons and heavy ions (Wambersie and Gahbauer 2001). However, most contemporary radiotherapy is carried out with Linacs and Co-60 machines (Khan 2003; Podgorsak 2004). In the present study, our discussion will be on teletherapy machines, with a particular focus on the Linac.

Linacs produce two main types of radiation beams: photons and electrons. Photons are used for the treatment of deep-seated tumors, and electrons are used for the treatment of superficial tumors less than 5 cm thickness. In a Linac, the radiation beam is produced from the source, located at the Linac's head, and then passes through different components, such as the collimators, before it reaches the patient. The collimators confine the width of the radiation beam to protect the tissues surrounding the tumor. Each collimator contains two pairs of orthogonal blocks through which a rectangular field can be achieved (Metcalfe *et al.,* 1997; Khan 2003). To more accurately shape the field to the form of the treatment target, extra lead blocks can be positioned below the collimators. More modern Linacs are equipped with a multileaf collimator (MLC), which consists of

two sets of leaves that make it possible to shape the field almost automatically to conform to the shape of the tumor. This development led to the emergence of the concept of conformal radiotherapy in radiation oncology clinics.

1.2 Conformal radiotherapy (CRT)

In CRT, the beams are shaped exactly to conform to the target volume (TV); conformal radiation treatment plans are realized by using a large number of beams of various weights, sizes, shapes and orientations to hit the target (Touboul *et al.,* 1994; Touboul *et al.,* 1996; Cardinale *et al.,* 2000). If enough beams of the proper type are used to provide an accurate representation of the tumor shape and size, a dose distribution can be created with a shape that conforms to the TV. In this regard, all radiation therapy treatment plans are conformal; however, the degree of conformation varies greatly depending on the irradiation technique used.

Conformal therapy aims to achieve the delivery of a high dose of radiation to the TV (a high dose conformity) and minimize the irradiation of the normal tissue. The fields are used in a manner that enables normal-tissue irradiation to be balanced against the delivery of an adequate dose to the TV (Fraass 1995; Mackie *et al.,* 2003; Geinitz *et al.,* 2005).

Three-dimensional conformal therapy (3D-CRT) has been developed with the introduction of three-dimensional imaging techniques such as CT, MRI and positron emission tomography (PET) (Sannazzari *et al.,* 2002; Ling *et al.,* 2000; Van Dyk 2005). 3D-CRT delivers a combination of beams from different directions to the TV. The aperture of each beam is shaped by an MLC to conform to the projected contour of the TV (Bourland *et al.,* 1994; Mohan 2006). The beam fluence can be optimized using wedges, physical modulators (compensation filters), or MLC (Cadman and Sidhu 1999; Wendt *et al.,* 2006; Spirou *et al*., 1994; Carol 1995).

3D-CRT can be categorized into two classes of technique: the use of geometric field-shaping alone or the modulation of the fluence intensity across the geometrically shaped

field (Webb 1998; Webb 2001a; Webb 2001b) (see figure 1.1a and b). The aim is to increase the dose to the TV while sparing the healthy tissues. 3D-CRT treatment varies from patient to patient, and refinements in some of the treatment protocols have led to improved conformations that correlate with improvements in clinical outcomes (Armstrong *et al.,* 1993; Robertson 1997). Studies have demonstrated the results of the treatment outcomes for different cancer sites and the potential to customize the dose to individual patients (McNee *et al.,* 1998; Nahum *et al.,* 1998; Gale *et al.,* 2009). It has been argued that CRT treatment is not justifiable because the improvement in treatment outcome is not worth the increased cost and complexity (Schulz 1999). However, studies have reported evidence for increased cure rates with CRT and suggest that the development of the new techniques would, at a minimum, enable the generation of more data to support the dose-escalation hypothesis (Mohan *et al.,* 1998; Webb 1998; Mohan *et al.,* 1999).

CRT is used for the treatment of cancers at different sites. However, the treatment of concave surfaces, such as the prostate and brain, requires the implementation of intensity modulation therapy (Zelefsky *et al.,* 1998; Pollack *et al.,* 1999).

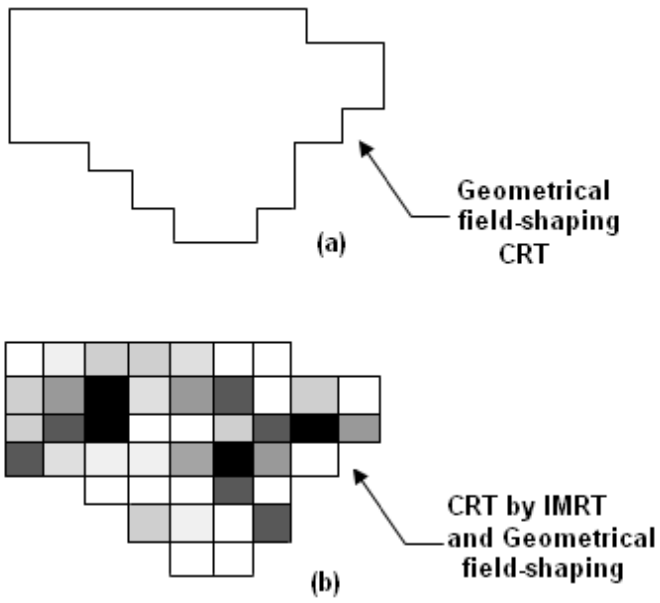

Figure 1.1 CRT with geometrical field shaping (a) and CRT by modulation through geometrical field shaping (b). (The illustrations are adapted from those of Webb 2001a).

Conformal avoidance (CA) describes the shaping of the dose to avoid OARs. This can be as important as obtaining an effective dose distribution in the TV, which requires a large number of beams (Graham *et al.,* 1994; Aldridge *et al.,* 1998; Aldridge *et al.,* 1999). It is imperative for conformal therapy to utilize the biological features of tumors to maximize treatment accuracy. Consequently, several studies have developed models for the biological prediction of tumor control probability (TCP) and normal tissue complication probability (NTCP) in the treatment outcomes of 3D-CRT (Yang and Xing 2005; Vanderstraeten *et al.,* 2006).

New technologies have clearly demonstrated a significant improvement in dose conformity to the TV and in sparing the OARs. Thus, the cost of advanced computer programs for inverse planning and intensity modulated radiation therapy (IMRT) can be justified (Wang *et al*., 2003; Zabel *et al.,* 2002; Didinger *et al.,* 2002; Young and Snyder 2001;Purdy 1999; Webb 2001a).

1.3 Intensity modulated radiation therapy

IMRT is considered to be one of the most advanced techniques for radiation therapy currently available. IMRT was developed independently by Cormack and Brahme (Brahme 1988; Cormack 1987; Bortfeld 2006) and has become widely accepted as a useful approach to the treatment of cancer patients.

IMRT refers to a form of 3D-CRT in which the intensity of the radiation beam is modulated across the treatment field (i.e., a non-uniform fluence is delivered to the patient to optimize dose distribution). Non-uniform fluence can be achieved by changing the MLC shapes and the intensity of each shape. Thus, different methods have been used to allow fluence variation within the field (Brahme 1988; Cormack 1987; Bortfeld 2006; Palter and Mackie 2003; Tong *et al.,* 2002; Sha *et al.,* 2004). IMRT is more complex than traditional 3D-CRT; it aims to achieve a highly conformal radiation dose by modulating the radiation beam's shape to achieve the desired dose distribution. Many important papers and reports on IMRT have been published (Webb 2003; Bortfeld 2006; Young and Snyder 2001; Francescon *et al.,* 2003; Chen-Shou *et al.,* 2000).

The concept underlying IMRT is that non-uniform beams can be used to deliver a desired dose distribution throughout the TV. The non-uniformity of each beam is based on anatomic features that are specific to the patient and permits a more complete avoidance of the nearby normal tissues than is possible with uniform-intensity radiation therapy. Thus, IMRT enables the delivery of minimal doses to all or part of the selected normal structures. In particular, one can create a concave irradiated volume that can spare much of an invaginating OAR, whereas uniform-intensity radiation therapy inherently creates convex irradiated volumes and cannot achieve such OAR sparing. This has enabled oncologists not only to shape the radiation beam, but, also to modulate it, giving higher doses to some parts of the tumor and lower doses wherever sensitive structures are nearby, with subsequent, increase in conformity to the target volumes, while further reducing the doses to the normal tissues (Bortfeld 2006).

To achieve the desired fluence distributions across the field for each incident direction of the radiation beam, the field for each gantry position or angle is opened differently for a set of small fields or "segments." This adjustment can be made by converting the initial dose/intensity map into a sequence of MLC shapes that can deliver the map. This conversion is the main purpose of setting the MLC sequencer program. Leaf sequencing is basically a process by which the complex non-uniform field is broken into subfields or segments of uniform fields (MLC shapes) that can be implemented by the MLC (Cormack 1987; Webb 1989; Xia and Verhey *et al.,* 2001). A number of computer methods have been developed to calculate the optimal intensity profiles (Mark *et al.,* 2001; Chen-Shou *et al.,* 2000; Francescon *et al.,* 2003). These methods are based on inverse planning, or optimization, which is an important step in IMRT. Optimization is a process by which the intensity distribution of each beam that is employed in a plan is determined so that the resultant dose distributions can best meet the criteria specified by the planner. These criteria are typically specified in terms of the dose and dose-volume requirements or according to biological indices such as TCP and NTCP.

The clinical implementation of IMRT requires at least two systems: (1) a treatment-planning computer system that can calculate non-uniform fluence maps for multiple beams directed from different directions to maximize the dose to the TV while

minimizing the dose to the critical normal structures, and (2) a system for delivering non-uniform fluences as planned (IMRT CWG 2001; Bortfeld 2006). The treatment-planning program divides each beam into a large number of small field "beamlets" and determines the optimal settings of their fluences, or weights. The optimization process involves inverse planning in which beamlet weights or intensities are adjusted to satisfy the predefined dose-distribution criteria for the composite plan.

IMRT is regarded as one of the most exciting treatment modalities in radiation therapy since the introduction of the imaging modalities in radiation treatment planning (IMRT CWG 2001; Van Dyk 2005). The technique provides higher dose conformity to the TV and conformal avoidance of the OAR. The obvious dosimetric advantage and increased reimbursement have motivated and increased the clinical demands of IMRT. Today, there are hundreds of publications on the use of IMRT in radiation oncology clinics and on the clinical impact of IMRT on cancer treatment. This impact is not limited to a certain cancer site but, is found in different treatment sites, such as breast, prostate, head-and-neck treatments. A study showed that approximately one-third of radiation oncologists use IMRT for different cancer sites to improve the delivery of conventional doses and to escalate the dose (Mell *et al.,* 2003). Improvements in dose conformation and in sparing OARs, as compared to the use of 3D-CRT, have been observed for different treatment sites, such as in breast, prostate, head-and-neck treatments (Gale *et al.,* 2009; Lire *et al.,* 2010; MacDonald *et al.,* 2007; Manuel *et al.,* 2011).

However, improvements in the IMRT delivery technique do not come without a risk. The use of IMRT is counterbalanced by the complexity of the IMRT planning and delivery process and the associated risk. The proximity of critical normal tissues to the TV and the need for sharp dose gradients in IMRT necessitate the accurate modeling of the radiation beam. Thus, IMRT requires a much greater understanding of the entire planning and delivery process, the associated quality assurance (QA) procedures and the tolerance limits with action levels. The IMRT process involve many steps, these increase potential errors from each one of these steps; as a result, rigorous QA procedures that ensure the process is carried out as prescribed and planned are highly essential.

Generally, IMRT QA consists of three aspects (Ezzell *et al*., 2009): (1) the commissioning and acceptance testing of the TPS and delivery systems, (2) routine QA of the delivery system, (3) and patient-specific QA. The first aspect is concerned with the reliability of the TPS in modeling the delivery system. The second aspect is concerned with the mechanical and dosimetric accuracy of the delivery system. The third aspect involves the dose delivery verifications used to ensure the safe and accurate treatment of the patient. The scope of the present study focuses on aspects of the patient-specific QA for IMRT.

1.4 Patient-specific QA for IMRT

The safe and effective delivery of IMRT requires a patient-specific QA program. Routine IMRT patient-specific QA programs usually involve the creation of a verification plan with which the dose distributions of an IMRT treatment are recalculated on the QA phantom geometry. The IMRT treatment is then delivered to the phantom to compare the measured doses to the TPS-calculated doses. The assumption is that if the TPS can accurately predict the dose to a phantom, then it can also accurately predict the dose to a patient. Therefore, patient-specific QA for IMRT serves several objectives:

I. to ensure that the TPS has accurately calculated the dose for the TV,
II. to ensure that the calculated IMRT plans are transferred accurately to the record-and-verify system,
III. to ensure that the delivery system is capable of delivering the modulated doses as planned.

The patient-specific QA process consists of verifying the absolute dose delivered to a reference point and the relative planar dose distribution (L´etourneau *et al.,* 2004). Verifying the relative dose distribution is more involved and is performed using two different methods: the *plan-related approach* and the *field-related approach*. In the first method, the entire plan (i.e., all fields with the correct beam entry directions) is transferred within the TPS to a verification phantom, and the dose distribution is calculated. Film has been the typical dosimeter of choice for this method (Zhu *et al.,*

2002; Zeidan *et al.,* 2006), although adequate diode arrays and ion-chamber arrays have recently been developed (Bedford *et al.,* 2009; Jursinic *et al.,* 2010).

The advantage of the *plan-related approach* is that all of the treatment parameters are identical to those for the treatment of the real patient; thus, the treatment delivered to the phantom is exactly what will be delivered to the patient. The plan can be verified within a single run. Effects such as those of treatment-couch attenuation are included in the QA delivery. However, with the increased use of 2D detector array systems, the inclusion of these effects in the QA could become less of an issue. In addition, the *plan-related approach* requires more sophisticated measuring phantoms. A potential drawback is that it may be more difficult to identify the sources of error when disagreement is found.

In the *field-related approach*, each single-treatment field is transferred separately to a verification phantom. All of the treatment parameters are the same as those for a real patient plan except that the gantry angle is set to 0° for all of the fields (Van Esch *et al*., 2002). The measurements usually can be done by using film, but, it has become increasingly common to perform the measurements with a 2D diode or an ion-chamber array (L´etourneau *et al*., 2004; Buonamici *et al*., 2007).

The advantage of the *field-related approach* is that being more comprehensive than the *plan-related approach*, in such a way that errors can easily be traced back to their sources. Dose measurements are always performed in a plane that is perpendicular to the central axis; hence, dosimetric problems are less critical than they are in the *plan-related approach*. The preparation and setup of the phantom is easy and less time consuming. The *field-related approach* is widely adapted to the use of various electronic 2D measuring systems. The *field-related approach* method is often criticized because the gantry is not rotated during the treatment delivery, meaning that every field is delivered from a single gantry angle. This removes effects that will be present during treatment, such as treatment-couch attenuation. In this study, the *field-related approach* was used for the patient-specific QA for IMRT because of the availability of the suitable dosimetric equipment.

In patient-specific QA for IMRT, the evaluation of the quality of the IMRT treatment plan is usually conducted through a comparison of the measured dose distributions and the calculated dose distributions. The dose matrix is then analyzed based on the dose difference (DD) and the distance-to-agreement (DTA) or gamma index criteria (Low *et al.,* 1998, 2003; Deptuydt *et al.,* 2002). Here, the percentage points of the area that passes a pre-selected criterion is used to indicate the quality of the entire planning and delivery process.

With the development of TPSs and delivery techniques for IMRT by different clinical and academic institutions, no standards have been clearly established for measuring equipment, measurement criteria or acceptable levels for the patient-specific QA for IMRT (Nelms and Simon 2007). As IMRT techniques have matured, the ion chamber and film measurements in the IMRT QA process have remained an accepted method of IMRT patient-specific QA (Low *et al.,* 2011). Other dosimetric tools for 2D dose distribution measurements include 2D ionization chamber arrays, 2D diode detectors and electronic portal imaging devices (EPIDs) (Masi *et al.,* 2010). Recently, 2D arrays of ionization chambers and 2D diode detectors have become the most popular devices for use in IMRT verification (Stathakis 2010; Gutiérrez and Calvo 2010; Masi *et al.,* 2010), and the use of EPIDs to perform verifications is currently being explored (Antonuk 2002; Wendling *et al.,* 2006; Van Elmpt *et al.,* 2008; Sabet *et al.,* 2010; Moran *et al.,* 2010; Pecharromán-Gallego *et al.,* 2011).

Although there are different choices of dosimeters for IMRT patient-specific QA, there is no agreement on the evaluation criteria for comparing the measured and calculated dose distributions (LoSasso *et al.,* 2001; MacKenzie *et al.,* 2002;Pawlick *et al.,* 2008; Sadagopan *et al.,* 2008; Yan *et al.,* 2009; Ezzell *et al.,* 2009; Rangel *et al.,* 2010). A survey study on planner IMRT QA analysis showed that a large number of institutions used a criterion of a dose difference and distance-to-agreement of 3% and 3mm respectively between the measured and calculated dose distributions (Nelms and Simon, 2007). The study reports that the number of points that passed the 3%/3mm dose difference and distance-to-agreement combined analysis was generally between 90% and

95% (Nelms and Simon 2007). The acceptable tolerances are dependent upon the disease site and the IMRT QA method. Basran *et al.* (2008) identified an agreement of greater than or equal to 95% for non-head-and-neck IMRT cases and an agreement of only 88% for head-and-neck cases. A recent study by the Radiological Physics Center (RPC) showed that 25% of institutions fail the credentialing test on the first attempt despite a generous verification criterion (7%/4mm) (Sakhalkar*et al.,* 2009). As a result, the report's authors suggested that the standard of IMRT QA could be improved if comprehensive 3D dosimetry were utilized. Palta *et al.* (2008) stated that "*each facility offering IMRT must develop its own guidelines and criteria for the acceptance and QA of IMRT*". These results lead to the question of what the acceptable criteria are and what guidelines will ensure an acceptable accuracy in dose delivery. Although recently published studies on IMRT QA provide general guidelines for tolerance limits and action levels, but, it does not seems to be practical to establish a standard across all the institutions with all these diversities in IMRT practice. The limited resources and experience in our institutions remain a challenge to the establishment of such guidelines.

1.5 A novel use of IMRT

In the developing world, setting IMRT can be used to save time and resources. Not only can the time required for the preparation, delivery and duration of the treatment be reduced, but, quality assurance can also be streamlined. At Steve Biko Academic Hospital (SBAH), cases of palliative head-and-neck cancer make up the majority of patients treated among the male population. Previously, parallel opposed fields with an electron boost field were used for the treatment of head-and-neck cancers. The use of this technique required a great deal of effort and time to prepare the compensating filters and shielding blocks at the mold room. This technique also required skilled personnel to produce the beam modifiers. Moreover, to generate a conformal dose distribution, experienced planners were needed. Currently, a three-field IMRT technique has been developed for the treatment of head-and-neck cancers but, we also do five field IMRT technique for radical treatment. A three-field IMRT plan with a concomitant boost delivers superior dose distributions, and with this approach, each fraction is faster and easier to treat. Furthermore, no boost is required, and, as a result, fewer fractions are

used. The use of IMRT technique for the treatment of head-and-neck cancers will save time and resources.

IMRT is an emerging technology with relatively few established QA guidelines. Thus, to ensure that the IMRT services consistently meet the highest clinical standard, each institute must invest in a comprehensive QA program for IMRT planning and delivery. Furthermore, IMRT utilizes more hardware and software, and adequate personnel and resources are necessary to implement and maintain the IMRT program. Unless the quality assurance program for IMRT can be streamlined, it will become a bottleneck that uses too many resources and too much time. The development of a quality assurance (QA) program for IMRT has been the final challenge for the implementation of this technique.

1.6 The aim of the study

The aim of this study is to develop and validate an IMRT patient-specific QA program at the Department of Radiation Oncology, Steve Biko Academic Hospital (SBAH).

This aim is realized through the following steps:

1. The study and evaluation of the dosimetric characterizations of the available detection system at Steve Biko Academic Hospital (a 2D-Array Seven29 ionization chamber) for IMRT QA verifications.

2. The study and evaluation of the dosimetric properties of an amorphous silicon electronic portal imaging device (a-Si EPID) and the validation of its clinical applications for IMRT QA.

3. The generation of an optimal IMRT plan using CMS XiO TPS, transfer the plan onto a standard IMRT phantom, perform comparisons of a relative dose measurement using the Kodak EDR2 and the 2D-Array Seven29 ionization chamber, and investigation of the comparison criteria for patient-specific QA.

4. An investigation of the feasibility of utilizing an amorphous silicon electronic portal imaging device (a-Si EPID) for IMRT pre-treatment verification.

5. The development of an independent monitor unit (MU) verification method to replace the absolute dose measurements for IMRT treatment and to verify the usefulness of the method for the patient-specific QA.

1.7 Contribution of the study

Intensity modulated radiation therapy (IMRT) aims to deliver highly conformal radiation dose to the target volume while sparing nearby critical organs as much as possible with the complex motion of multi-leaf collimator (MLC) leaves. The patient-specific quality assurance (QA) has become an essential part of IMRT in assuring that the delivered dose distributions agree with the planned ones. At Steve Biko Academic Hospital (SBAH), we use IMRT plans for radical as well as for palliative patients to save time and resources because a concomitant boost and simplified set-up can save time per fraction and for the total duration of the treatment. A cumbersome, time-consuming QA step can negate these advantages. This thesis aims to develop and validate an IMRT patient-specific QA program at the Department of Radiation Oncology, Steve Biko Academic Hospital (SBAH). The contribution of the research work from this study are; i) evaluation of the clinical impact of the deviations in step-and-shoot IMRT plans (chapter 4 and 5). ii) Development of an independent monitor unit check program for the IMRT patient-specific QA (chapter 6). For the evaluation of the clinical impact deviations; the routine QA picked up a systematic error from the treatment planning system (TPS) that could be rectified and proved that its necessary to be performed prior the delivery of the IMRT patient's plan. For the developed independent monitor unit verification method; the method is intended to be used as an independent verification method for the IMRT patient-specific QA. The independent monitor unit check program (MUCP) was found to be simple, fast, easy and accurate enough to be used in routine verifications for head-and-neck IMRT. The study proposed that the 2D-Array Seven29 dosimetry system and the developed monitor unit check program (MUCP) could be used in the department for the routine IMRT patient-specific QA program. This dosimetry system can be used for the

IMRT fluence map measurements with reasonable accuracy while maintaining the large number of IMRT plans in the department. When a plan fails to meet the 3%/3 mm criteria for more than 10% of the points inside the field, then the measured plan be used to calculate the actual delivered dose, and only if there is a clinically significant deviation from the prescribed plan must it be redone. The monitor unit check program can be used with the help of the absolute dosimetry for the point-dose verification for the step-and-shoot- IMRT deliveries.

2. The validation of a 2D-Array Seven29 ionization chamber for IMRT quality assurance

2.1 Introduction

The main goal of radiotherapy is to deliver a high radiation dose to the TV while further reducing the radiation dose to critical organs and healthy tissues. Therefore, the verification of the radiotherapy treatment plan is an essential step, particularly in complex radiotherapy techniques such as IMRT. Recently, a 2D detector array has become the standard device for the verification of IMRT measurements (Feygelman*et al.,* 2009; Janathan *et al.,* 2009; Gutiérrez*et al.,* 2010). Although radiographic film proved to be the most practical and cost-effective method overall, there are some obstacles to the use of radiographic film. The film is affected by the processor characteristics during development, which creates the need for a film calibration curve for each quality assurance analysis (Ju *et al.,* 2002; Bucciolini *et al.,* 2004; Jacob *et al*., 2008; Bouchard *et al.,* 2009). The film response is energy dependent and can cause dosimetry errors when measurements are performed for different energy spectra. In addition, film measurements are more time-consuming than 2D array measurements. Gafchromic films, which were developed for industrial radiation monitoring, have been refined for clinical radiotherapy dosimetry (Chu *et al.,* 1990; Devic *et al.,* 2004). These films are self-developing and require no physical or chemical processing. The optical density of the irradiated film is measured by using optical measuring systems such as densitometers and document scanners (Devic *et al.,* 2005; Ziedan *et al.,* 2006).

The 2D-array ionization chamber devices are easy to use and provide quality assurance results in real-time. Although 2D detector system arrays do have poorer spatial resolution than film and electronic portal imaging devices (EPID), the detection system provides direct measurements of doses with frequent calibration, and the measurements are in real-time. Furthermore, the detector is easy to handle for daily setup.

Two types of 2D detector system arrays for the primary use of providing patient-specific QA for IMRT are commercially available: ionization chamber arrays (with two

commercial models: ImRT MatriXX (Scanditronix Wellhofer GmbH, Germany) and Seven29 (PTW, Freiburg, Germany)) and MapCHECK diode arrays (Sun Nuclear Corp., Melbourne, FL). Several studies have been conducted on both types of detector arrays. Amerio *et al.* (2004) and Stasi *et al.* (2005) described the design principle and the dosimetric properties of a prototype 2D pixel ionization chamber array, which was the basis for the ImRT MatriXX ionization chamber. Jursinic and Nelms (2003) and L´etourneau *et al.,* (2004) investigated various characteristics of a 2D diode array for IMRT verification. The behavior and dosimetric characteristics of the 2D-Array Seven29 have been described by several authors (Poppe *et al.,* 2006; Spezi *et al.,* 2005; Wiezorek *et al.,* 2005). Recently, Janathan *et al.* (2009) studied the dosimetric characteristics of two different detector systems and recommended that each institution employing these devices for IMRT QA should validate the performance of the dosimetry system before its use in clinical verifications. Spezi *et al.* (2005) investigated the characterization of the 2D-Array Seven29 and its feasibility for use in radiotherapy verifications.

The study by Spezi *et al.* (2005) reported promising results regarding the use of the 2D-Array Seven29 for the verification of clinical radiotherapy beams. However, most of the studies were performed with only 6 MV photon beams. The IMRT technique is relatively new in South Africa; therefore, the device must be characterized before it can be used for patient verifications.

Most of the experimental procedures demonstrated by Spezi *et al.* (2005) were followed in the present study with the intention of implementing the 2D-Array Seven29 for routine QA for IMRT in our department. Many properties of the 2D-Array detector must be thoroughly understood before it can be applied for accurate IMRT verification.

The purposes of the phase of the study described in this chapter were as follows:

1. To characterize and evaluate the dosimetric properties of a 2D-Array Seven29 ionization chamber from PTW (Freiburg, Germany) with the objective of using the detector for IMRT QA verifications. The basic tests evaluated the calibration of the 2D-array, the reproducibility and start-up behavior of the 2D-array, the

linearity and energy dependence, the output factor, the sensitivity and the clinical application of the array for fluence map verifications.

2. To validate the results of the dosimetric properties of the 2D-Array Seven29 ionization chamber based on a comparison with the published literature prior to implementing the IMRT QA.

2.2 Materials and methods

The 2D-Array Seven29 model (PTW, Freiburg, Germany) (PTW type 10024) was used in this study. The 2D-Array consists of 729 air-filled ionization chambers arranged in a 27 × 27 matrix. The ionization chambers are separated from each other by a distance of 5 mm. The chamber center-to-center distance is 1 cm; these chambers cover an active area of 27 × 27 cm^2. Each single chamber has dimensions of 0.5 × 0.5 × 0.5 cm^3. The chamber sensitive point of measurement is located approximately 0.5 mm from the surface of the 2D-Array. The physical dimensions of the 2D-Array are 42.0 × 30.0 × 2.2 cm^3. The distance between the chamber centers is equal to one leaf pair of the most multi-leaf collimators (MLC), which is projected onto the isocenter. This allowed the projection of each pair of opposing leaves in the MLC to cover exactly one row of the chambers, in which it can reflect a clear reading of certain collimator pairs. The entrance plane of the array is usually perpendicular to the radiation field from the accelerator head.

The material surrounding the ionization chambers of the 2D-Array is PMMA. A 20-mm back-scatter material is also fixed behind the 2D-Array. The wall material of the 2D-Array chamber is made of graphite, and the area density above the chamber volume is 0.6g/cm^2. The air-filled ionization chambers were covered with a 5-mm-thick PMMA in the front plate, which was fixed as part of the array construction. The array interface dimensions are 8.0 × 25.0 × 30.0 cm^3, and the PTW-Array interface type is T16026 (see figure 2.1). The 2D-Array operated at a chamber voltage of 400 V. The 2D-Array accumulated the electric charge for each chamber on a capacitor that was read-out and reset every 400 ms. The 2D-Array made it possible to measure the absorbed dose (Gy) and the absorbed dose rate (Gy/min) to water in a continuous operation mode. The measurement ranges were specified by the manufacturer and were 200 mGy to 1,000 Gy

and 500 mGy/min to 8 Gy/min for the absolute dose and dose-rate measurements, respectively. The 2D-Array and the 2D-Array's multi-channel interface (PTW-interface type 16026) were calibrated by the manufacturer in terms of the absorbed dose to water using a certified ^{60}Co radiation source. Figure 2.2 shows the structure of the 2D-Array ionization chamber.

The radiation source that was used in this study was the Siemens ONCOR Linac (Siemens Medical Solutions, Concord, USA) with IMRT delivery mode. The accelerator was also equipped with a 160-leaf MLC OPTIFOCUS MLC. This accelerator has six electron energies (6, 9, 12, 15, 18 and 21 MeV) and is capable of producing X-ray energies of 6 and 15 MV. The 6 and 15 MV photon energies were investigated in this study because these energies are used for IMRT treatment.

Figure 2.1.The PTW 2D-Array Seven29 (PTW, Freiburg, Germany) and the 2D-Array interface (PTW, Freiburg, Germany).

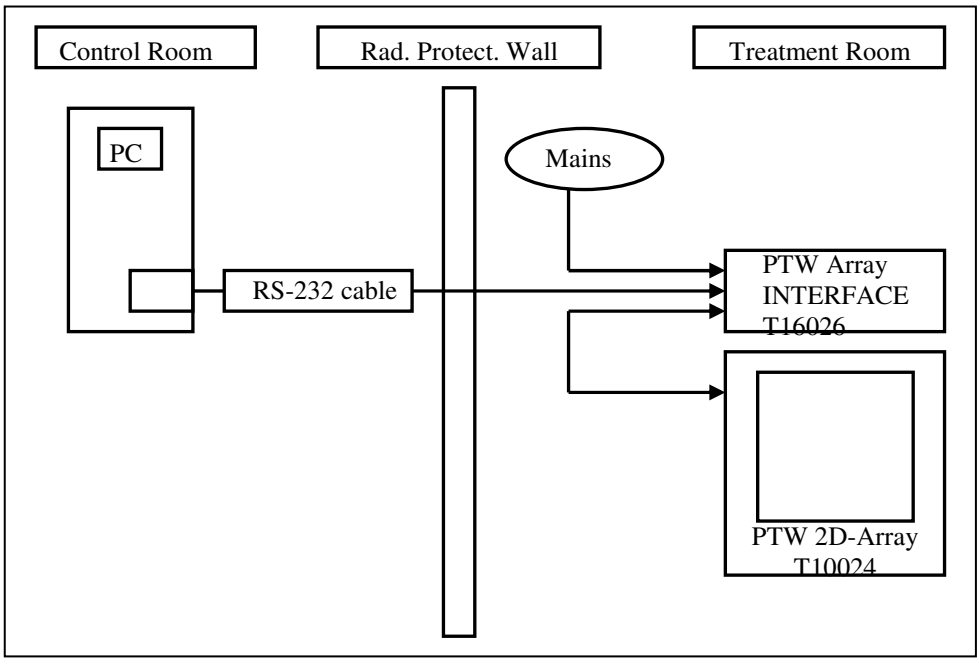

Figure 2.2.An overview of the structure of the system.

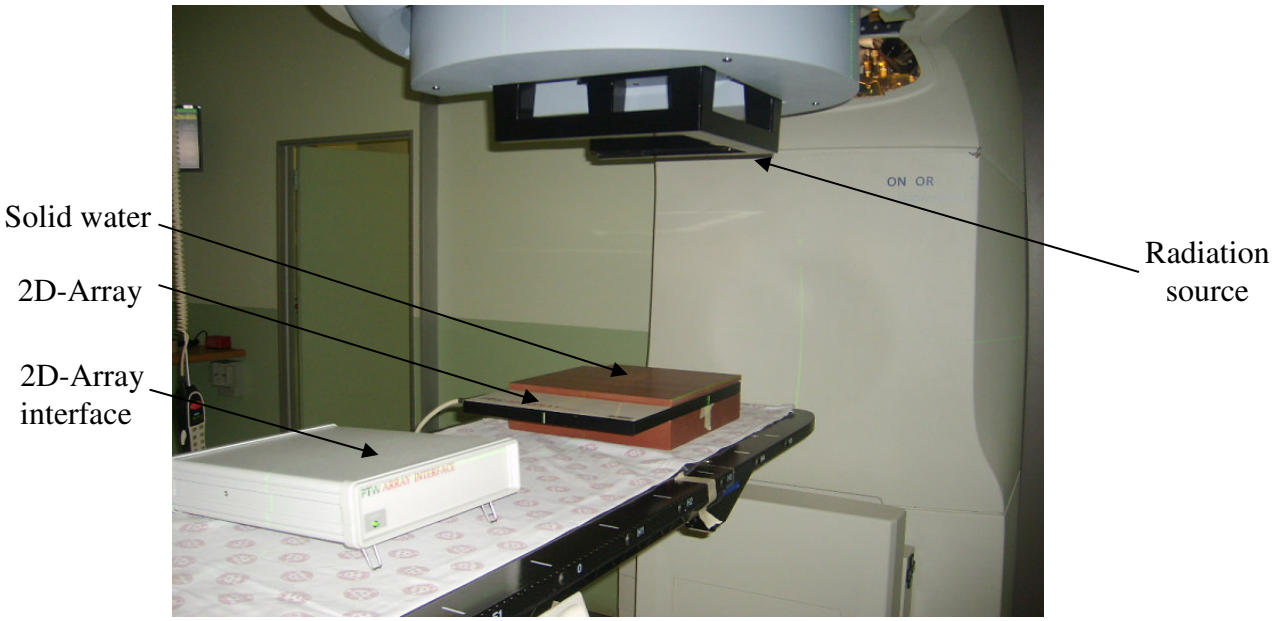

Figure 2.3.The experimental set-up of the 2D-Array Seven29 ionization chamber system.

2.2.1 Calibration of the 2D-Array

The 2D-Array was calibrated to determine the calibration factors to correct for the different responses of the single ionization chambers of the 2D-Array. With this method, an improvement of the dose homogeneity can be achieved. The calibrations were performed using a 6 MV photon beam. The 2D-Array was placed on top of the treatment couch as shown in figure 2.3. The geometry of the placement is given in figure 2.4. For the build-up and the backscatter materials, a set of solid-water phantom slabs was used (Gammex, RMI, Middleton, WI, USA). The slab sizes were 30 × 30 cm^2, with different thicknesses. The mass density of the solid-water material was 1.04 g/cm^2, and the electron density had a factor relative to water. The total thickness of the build-up was 4.5 cm, the thickness of the backscatter materials was 5.0 cm, and the source-surface distance (SSD) was set at 95.0 cm. Therefore, the 2D-Array reference point of the measurements was located at 100 SSD from the radiation source.

The calibration factors for each chamber in the 2D-Array were obtained from the measurements of two calibration matrices: one matrix was used for the reference calibration, and the other matrix was used for the absolute calibration. This was done with the aid of MatrixCal software. This software offers two options for calibration: a reference calibration and an absolute calibration.

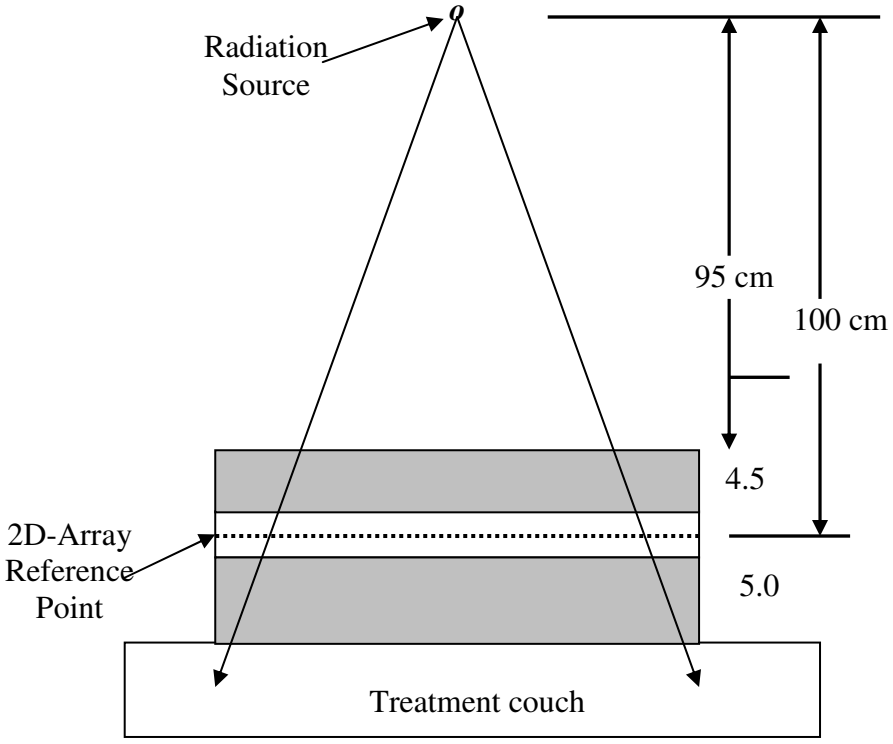

Figure 2.4.The placement geometry of the 2D-Array Seven29 ionization chamber.

2.2.1.1 Reference calibration

For the reference calibration, a maximum field size of 27 × 27 cm^2 was used. The experimental set-up is shown in figure 2.4. Prior to using the 2D-Array for calibration, a zero measurement of the complete measuring system was performed on the 2D-Array and its associated interface (the 2D-Array detection system). A period of approximately ten seconds was allowed to pass, and then the 2D-Array was irradiated with a dose of at least 100 cGy while the chamber voltage was on. This was done according to the manufacturer's recommendation (2D-Array user manual). The manual is the best guide for a step-by-step procedure for calibration. Figures 2.5. and 2.6 show a panel of the reference calibration procedures and the reference matrix for the 2D-Array system.

In the reference calibration, all of the chambers were calibrated relative to the center chamber by assigning an absolute value for the center chamber. First, the 2D-Array measured matrix (new reference matrix) values (M) were normalized to the center value

(M_z); then, the 2D-Array reference matrix (old reference matrix) values (R) were normalized to the center value (R_z). The reference calibration factor was calculated as the quotient of the 2D-Array measured matrix and the reference matrix. The obtained calibration factor (reference calibration factor) was multiplied by the absolute calibration factor. Finally, the absolute calibration factors are corrected by the total correction factor.

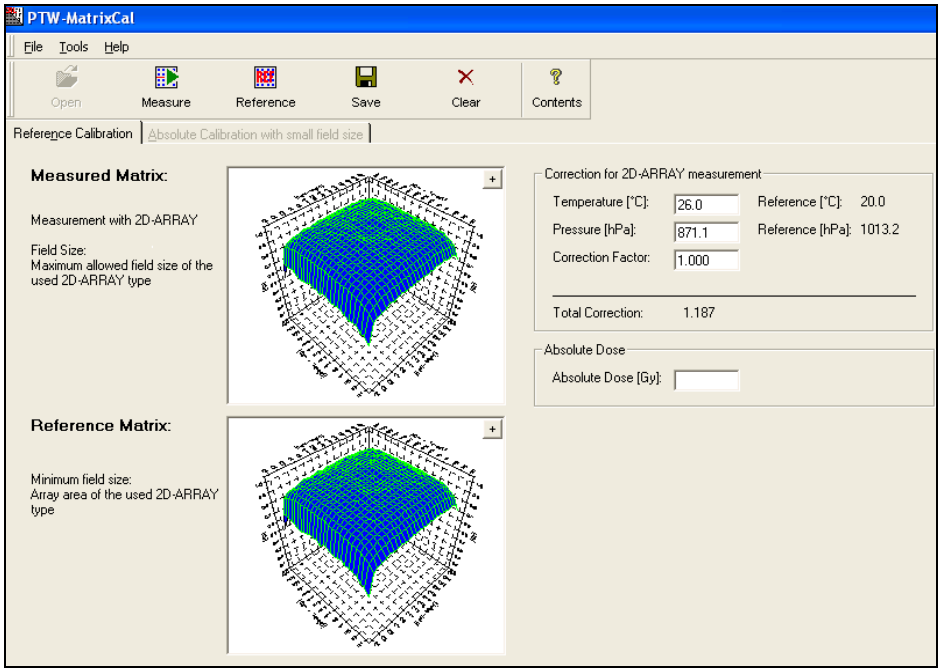

Figure 2.5.A panel of the procedure for obtaining the reference calibration matrix.

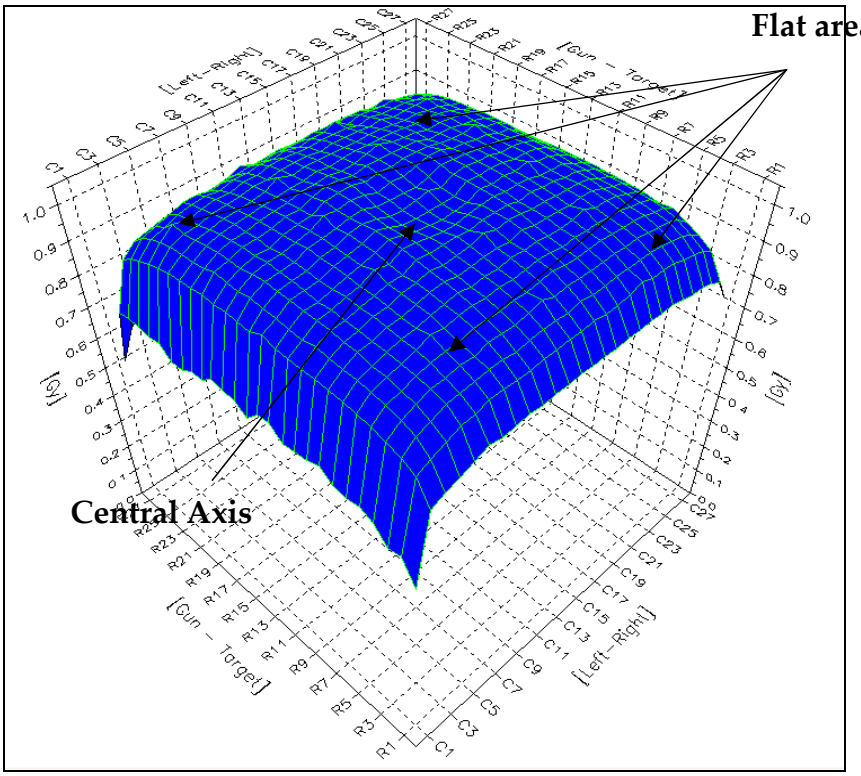

Figure 2.6.A 27 × 27 reference matrix for calibration of a 6 MV 2D-Array at 300MU/min.

2.2.1.2 Absolute calibration

For the absolute calibration, either the previously stored reference calibration matrix or a recently generated reference calibration matrix (from MatrixCal software) is required. A field size of 10 × 10 cm^2 is sufficient for absolute calibration because only the center chamber is adjusted to the absolute value.

The calibration factors for the remaining chambers were calculated relative to the center chamber depending on the calibration file or matrix loaded.

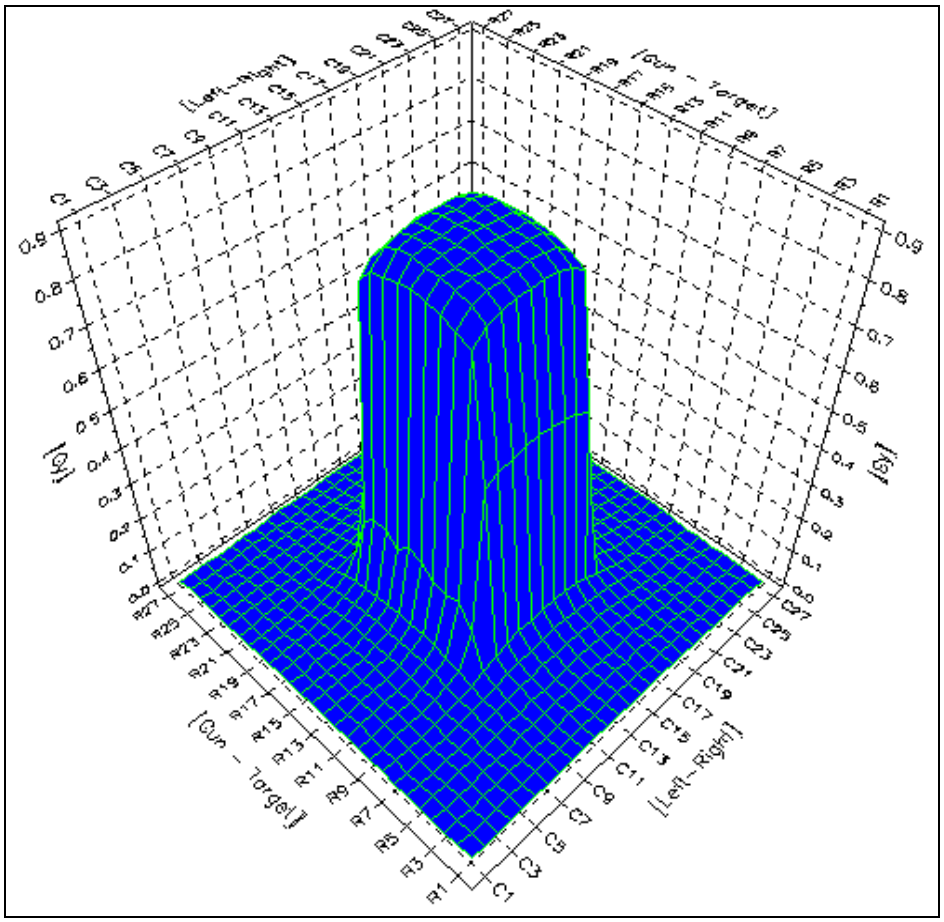

Figure 2.7.A 10 × 10 absolute matrix for calibration of a 6 MV 2D-Array at 300MU/min.

2.2.2 Reproducibility

The 2D-Array reproducibility checks were performed over a measurement session to check the performance and reproducibility of the output of the 2D-Array detector system. The test was done with the same set-up as that shown in Figure 2.4. An X-ray energy of 6 MV was used, and 100 MUs were delivered per reading with a fixed field size of 10 × 10 cm^2. The 2D-Array electronics were switched on for a period of 5 minutes prior to the irradiation, as recommended by the manufacturer. To check the reproducibility of the 2D-Array measurements, various sets of measurements were investigated. The first set was taken after a warm-up of the 2D-Array. The second set was taken after a break of 30 minutes during which the 2D-Array was switched-off. The third set was taken after a break of 30 minutes without switching off the 2D-Array. In each set of measurements, 20 consecutive readings were taken.

2.2.3 Linearity and energy dependence

The linearity tests of the 2D-Array were only performed for the central chamber of the 2D-Array (chamber 14 × 14) because the 2D-Array exhibits a uniform inter-chamber response once it is calibrated. Measurements were made using two different energies, 6 and 15 MV photon beams (Siemens ONCOR Linac, Siemens Medical Solutions, Concord, and USA), at 5-cm build-up, 95-cm SSD geometry and a 10 × 10 cm^2 field size. The dose linearity response of the 2D-Array of the central chamber of the 2D-Array was evaluated by measuring the output of the beam for 1, 2, 3, 5, 10, 20, 50, 100, 200, 300 and 500 MUs at the nominal operating accelerator dose rates, which were 300 and 500 MU/min for 6 and 15 MV, respectively. The measurements represented the average of ten consecutive irradiations for each MU. The 2D-Array results were validated through comparison measurements made with a Pin-Point ionization chamber CC13 (Scanditronix/Wellhöfer) and a Farmer ionization chamber (PTW type W30013) connected to a UNIDOS electrometer (PTW, Freiberg, Germany) under identical irradiation conditions.

2.2.4 Output factor

The output factor is a function of the energy and depth in the phantom, and the field-size-dependence of the output factor results from the contribution to the dose on the beam axis by photons scattered from peripheral parts of the beam toward the axis. Therefore, the performance of the 2D-Array when measuring the Linac radiation output factor as a function of field size was investigated. This test effectively assessed the scatter properties of the 2D-Array ionization chamber detectors, which depended on the internal design of the device. The response of the 2D-Array with small field sizes was of particular interest because of the potential applications in the verification of IMRT plans.

The output factors were measured at a depth of 5 cm; this depth was chosen because it is commonly used in radiotherapy of the head and neck regions. The output factor was measured for various square field sizes ranging from 1 × 1 cm^2 up to 27 × 27 cm^2 and for energies of 6 and 15 MV. This measurement was conducted for the set-up that is shown in figure 2.4. Larger field sizes were not possible for the 2D-Array under investigation

because its physical dimensions only allow a maximum field size of 27 × 27 cm^2. The results of the relative output factor derived from these measurements were compared to the measurements made with a Farmer ionization chamber (type W30013) and a Pin-Point chamber CC13 (Scanditronix/Wellhöfer) in a water phantom under identical irradiation conditions. The output factor results were normalized to the 10 × 10 cm^2 field-size output factor.

2.2.5 Sensitivity

The 2D-Array consisted of 729 ionization chambers that were equally spaced at a 1 cm center-to-center distance. The edges of the two adjacent chambers were separated by 0.5 cm. When the 2D-Array was irradiated, a lateral motion of the secondary particles produced by the photon interacted with the 2D-Array's chambers and the surrounding materials, which led to signal perturbation (Poppe *et al.* 2007). The 2D-Array sensitivity was investigated in these experiments and is described below.

2.2.5.1 MLC movements

The experimental setup of the 2D-Array positioning that was used in this test is shown in figure 2.8. This test was conducted to evaluate the effective detection area of the ionization chambers of the 2D-Array. The method used for MLC movements is the same as that described by Spezi *et al.* (2005). The initial field dimensions were set at 4 × 25 cm^2. The MLC leaves (X1-Leaf) were then gradually moved to close the field with an increment of 1 mm for 20 steps until the field size reached 2 × 25 cm^2. The 2D-Array was irradiated in a sequence measurement mode. The procedures are shown in different collimator positions in figure 2.8. The leaves were moved a distance of approximately 2 cm (from -2 to 0 cm), as shown in figure 3.8. At each step, 100 MUs were delivered.

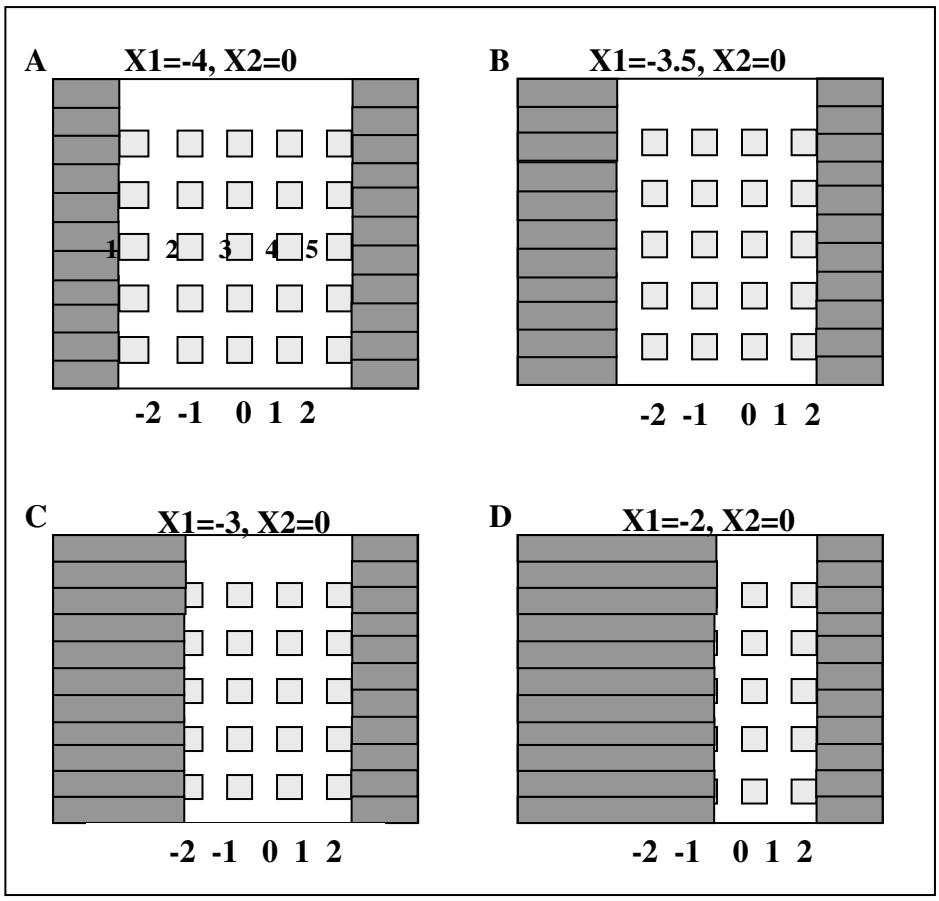

Figure 2.8.The experimental set-up for the investigation of the perturbation effect of the irradiated area of the 2D-Array and of the detector sensitivity to the positional changes of the MLC leaves.

2.2.5.2 Leaf coverage

The experimental set-up of this test is shown in figure 2.9; the SSD was 95 cm to the top of a build-up, which was 4.5 cm from the 2D-Array reference point of measurements. This test was arranged so that the four chambers of the 2D-Array overlapped or were covered by three leaves. Figure 2.9 gives an overview of the leaf positioning for the four selected chambers. In this figure, the first leaf (MLC 1) was positioned to cover chamber (A) entirely. The second leaf (MLC 2) was positioned or localized between two chambers, chamber (B) and chamber (C), in such way that the leaf partially covered each of the two chambers. The last leaf (MLC 3) was positioned to partially cover chamber (D) with less coverage than the second leaf (MLC 2).

The purpose of covering the chambers was to determine which arrangement would exhibit the highest sensitivity of the 2D-Array to the leaf position. After the arrangements were made, irradiations were performed in 1-mm steps, and a set of 15 consecutive measurements were taken. The start position was position zero, at which the leaf covered the entire chamber, and measurements were taken until the leaves reached the end position (position 15). The 2D-Array was irradiated with a dose of 100 MUs, and the readings were recorded for each chosen chamber.

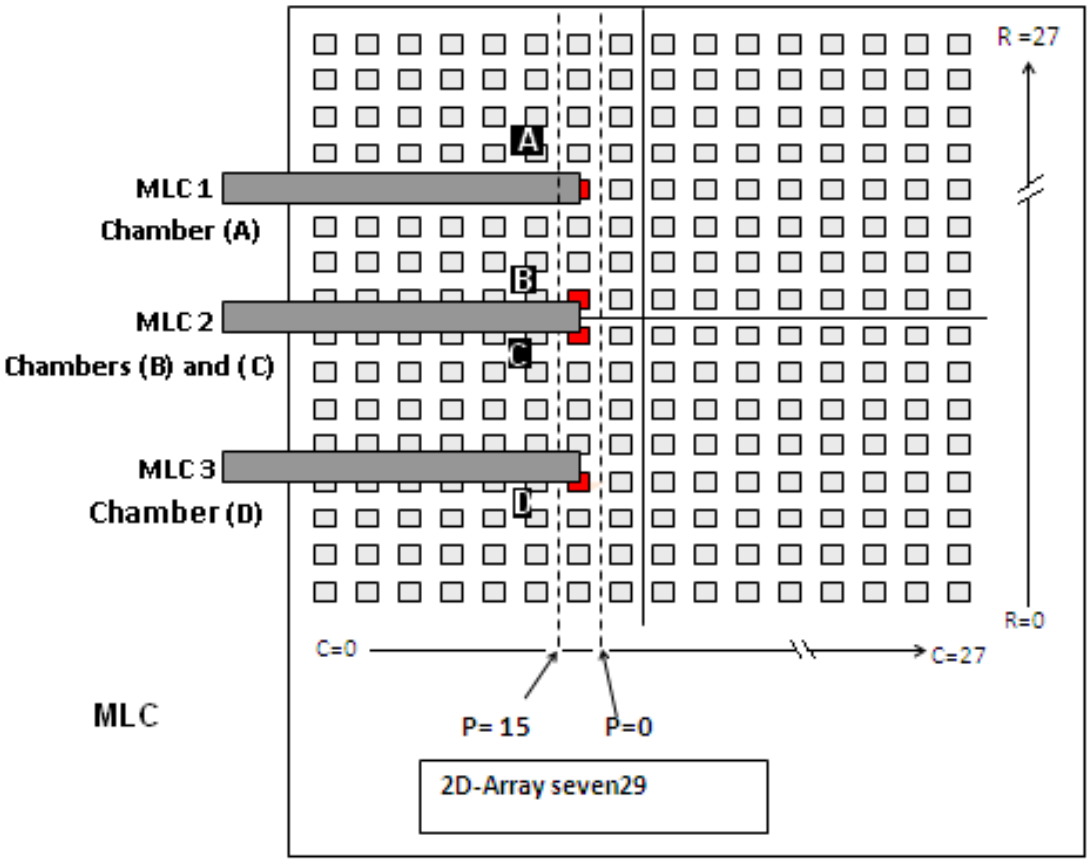

Figure 2.9.A schematic illustrates the MLC configurations on the 2D-Array. P=1 defines the start position of each leaf. P=15 illustrates the maximum leaf shift.

2.2.6 Clinical applications

For absolute dosimetry, the 2D-Array was calibrated with a given photon energy by delivering 100 cGy to the 2D-Array ionization chamber system with a field size of 10 ×

10 cm^2 and at an SSD of 100 cm. The MatrixCal software calculated the central chamber output to determine the dose correction factor. The correction factor and the inter-chamber responses were saved in a file that was loaded when the MatrixScan was used for subsequent dose measurements for a specific photon energy.

For the relative dose distribution that is delivered by any given beam, the measured or the calculated fluence maps can be loaded into the VeriSoft software for comparison with the fluence maps that are measured with the 2D-Array ionization chamber system. The agreement between the measured and calculated fluence maps was evaluated by determining the number of chambers that satisfied the tolerance dose difference and the distance to agreement that can be set by the user. Examples of clinical applications for the dose fluence maps will be discussed in chapter 5.

The clinical application of the 2D-Array was also verified with simple comparisons of the open and wedged beam profiles that were measured for different field sizes. The wedge angles that were used were at 15, 30, 45, and 60 degrees. The field sizes were set for 5 × 5 cm^2, 10 × 10 cm^2, 15 × 15 cm^2 and 20 × 20 cm^2. The beam profiles were measured with the Pin-Point ionization chamber (CC13 Scanditronix Wellhöfer) and the 2D-Array for both 6 and 15 MV photon energies. The 2D-Array reference point of measurements was set at 95 SSD on top of a build-up thickness of 5 cm. For the Pin-Point measurements, the beam profiles were obtained by scanning the chamber in the water tank at a depth of 5 cm in water and at 95 cm for the SSD. Plot comparisons of the results are shown in section 2.3.6.

2.3 Results and discussion

The experimental procedures for the 2D-Array ionization chamber characterization with the Siemens ONCOR Linac (Siemens Medical Solutions, Concord, USA) were described above. The characteristics were evaluated in terms of the response of the 2D-Array ionization chambers, the reproducibility of the output, the output of the 2D-Array, the dose linearity and energy dependence, the sensitivity of the 2D-Array and the clinical

applications of the use of the 2D-Array. In this section, the results of the experiments are presented.

2.3.1 Calibration of the 2D-Array

2.3.1.1 Reference calibration

The calibration matrix was obtained by dividing the measured matrix by the reference matrix. The calibration matrix was a matrix of correction factors that was used to correct the reading or the signal that was obtained from the 2D-Array ionization chambers during the measurements. The correction factors were different for each individual chamber; these correction factors will be used until the next calibration of the 2D-Array ionization chamber system is performed.

2.3.1.2 Absolute calibration

The absolute calibration was done for the 2D-Array ionization chamber system. The correction factor was found to be 1.101±0.001; hence, the total calibration factor was equal to 1.171±0.002. This factor was saved as a default calibration factor in the MatrixScan software; new measurements were based upon this default calibration factor.

2.3.2 Reproducibility

Figures 2.10 (a) and (b) show the results of the reproducibility test of the 2D-Array ionization chamber as a function of the number of measurements. The total number of measurement points was 60. This number was obtained in three phases of measurements. The experimental average of the 20 measurements with the associated standard deviation is displayed in both figures (see figures 2.10 (a) and (b)).

Figure 2.10 (a) shows the reproducibility results of the 2D-Array ionization chamber. The black points on the graph show the results that were obtained from the irradiations after the 2D-Array ionization chamber was warmed up. The red points depict the results of the 2D-Array irradiations after a break of 30 minutes, during which the 2D-Array was switched off. The 2D-Array signal seemed to be very stable during irradiation after the 2D-Array ionization chamber warmed up; the maximum standard deviation for the 2D-

Array and for the 20 consecutive measurements is 0.3%. A clear increase was observed in the 2D-Array signal during irradiation after a 30 minute break was taken and the 2D-Array ionization chamber system was switched off; this increment in the 2D-Array signal from the first irradiations up to 5 measurements (equivalent to 500 monitor units or 500 cGy) was approximately 2%.

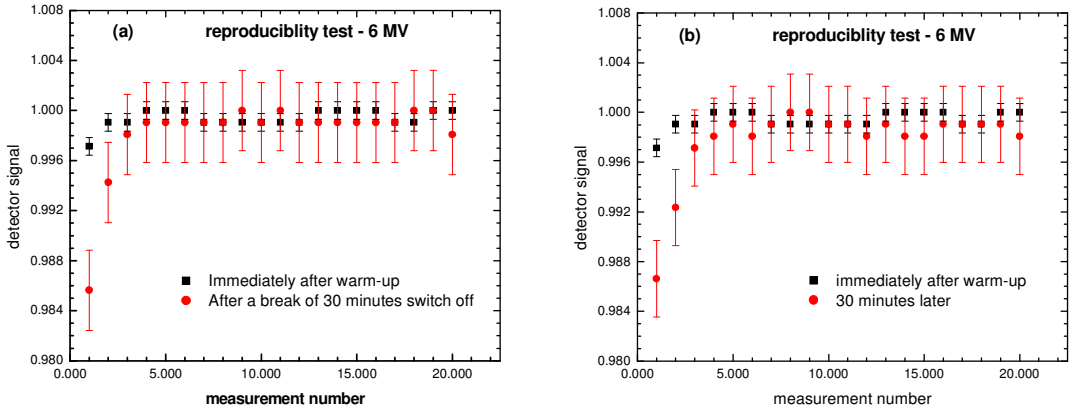

Figure 2.10.The obtained signal of the 2D-Array for 20 consecutive irradiations with 6 MV photons and 100 monitor units per irradiation. (a) One measurement was performed immediately after the 2D-Array ionization chamber system was warmed up (black points), and the other measurement was performed after a 30 minute break was taken, during which the 2D-Array system was switched off (red points). (b) One measurement was performed directly after the 2D-Array ionization chamber system was warmed up (blue points), and the other measurement was performed after a 30 minute break was taken without switching off the 2D-Array system (red points). The error bars is both figures represents the standard deviations.

Figure 2.10 (b) shows almost the same behavior of the 2D-Array detector system after a break of 30 minutes, during which the 2D-Array was turned on. In this case, the signal increased for the first 5 irradiation measurements by a value of 1.5%. The maximum standard deviation for 20 consecutive measurements was 0.3%. In general, the 2D-Array ionization chamber detector system must be pre-irradiated for at least 500 MUs or 500 cGy before measurements are taken after a break whether the system is switched-off or is left on; this pre-irradiation is necessary to stabilize the detector and to obtain reproducible

measured values. Based on the local percentage differences between the two situations, the maximum difference is approximately 0.8%, and the average difference is nearly 0.4%.

After the warm up, the detector reading became stable. However, when the detector was given a break of 30 minutes and was either switched off or left on, it was necessary to expose the detector to 500 MUs to ensure stable readings. Thus, an initiation dose of 500 cGy was necessary to stabilize the detector. Therefore, it is not advisable to take a break from taking measurements after the detector is warmed up; if a break is taken, a pre-irradiation dose of 500 cGy is necessary.

2.3.3 Linearity and energy dependence

From the linear response curves (figures 2.11. (a) and (b)), it is evident that the 2D-Array has a high degree of linearity within the range of 2 to 500 MU with a linear coefficient R^2 of 1.0 for both 6 and 15 MV photon energies.

In these figures, the slopes of the linear fit show that the linear relationship between the MU and the detector response is good down to the lowest delivered doses. The slope and the standard error were 0.998 and 0.001, respectively, for both photon energies. The standard deviation values were 0.003 for both photon energies.

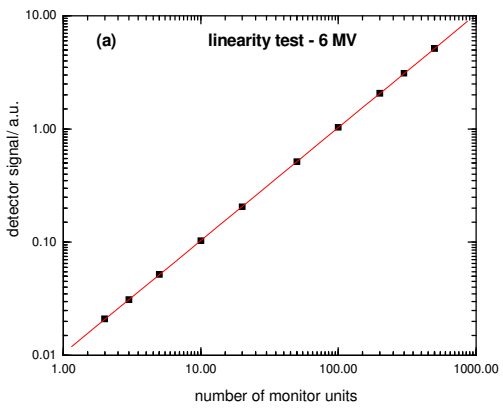

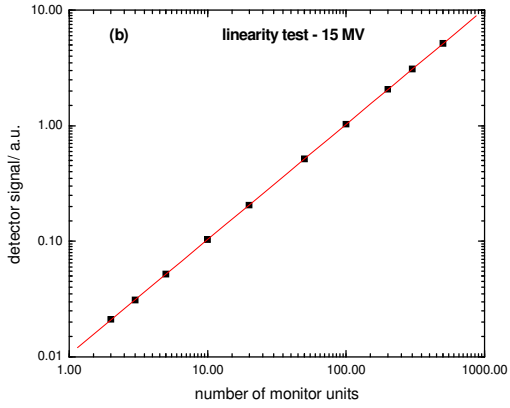

Figure 2.11. In (a) and (b), the signal of the 2D-Array is plotted against the number of monitor units for 6 and 15 MV photon beams, respectively. The central axis measurements are shown as symbols. The results of the linear regressions (solid line) are also shown. The monitor units were set from 2 to 500 MUs.

The 2D-Array signal is plotted against the dose for two different photon energies in figure 2.12. The detector had a linear dose response that was observed at 6 and 15 MV photon energies. The signal of the 2D-Array detector was dependent on the radiation beam energy in the range of 6 to 15 MV. The standard deviation values were 0.001 for both photon energies.

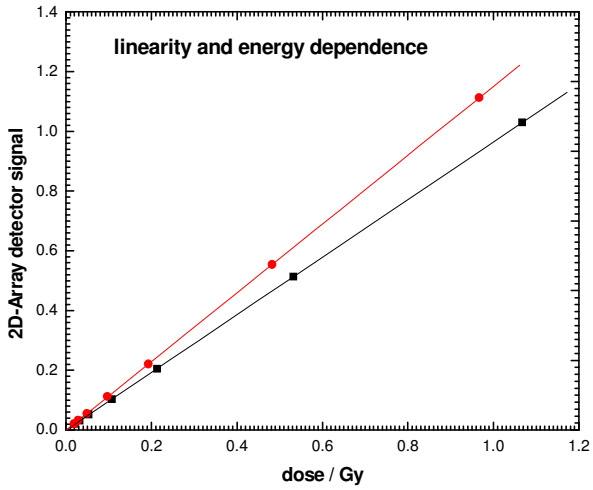

Figure 2.12.The signal of the 2D-Array versus that of the Farmer chamber at 6 MV and 15 MV photons and 100 monitor units per irradiation for different doses. The central axis measurements are shown as symbols.

2.3.4 Output factor

Figures 2.13. (a) and (b) show a comparison between the output factors of 6 and 15 MV photon beams that were measured for different field sizes with the 2D-Array central axis chamber, a Farmer ionization chamber (PTW type W 30013) and a Pin-Point chamber (Wellhöfer CC13, Scanditronix). Data from the results of the 2D-Array, the Farmer

ionization chamber (PTW type W 30013) and the Pin-point chamber (Wellhöfer CC13, Scanditronix) were normalized with respect to that of a 10 × 10 cm^2 field size output factor.

For field sizes equal to and larger than 4 × 4 cm^2, the 2D-Array ionization chamber and the Farmer ionization chamber (PTW, type W 30013) results were within 1.1% and 2.0% of each other for 6 and 15 MV energies, respectively. For field sizes between 25 × 25 cm^2 and 27 × 27 cm^2, in which the field size surpassed the 2D-Array, the 2D-Array underestimated the output factor by 1.3% for 6 MV and by 1% for 15 MV. The results also showed that for field sizes that were smaller than 4 × 4 cm^2, the Farmer ionization chamber tended to underestimate the output factor as a result of its larger volume (Laub and Wong 2003; Martens *et al.,* 2000).

The output factors that were measured with the Pin-Point chamber (Wellhöfer CC13, Scanditronix) and with the 2D-Array ionization chamber for small field sizes down to 2 × 2 cm^2 were within 2% of each other. For the 1 × 1 cm^2 field size, the Pin-Point chamber output factor value was 13.5%, which was lower than the 2D-Array ionization chamber output value for 6 MV. For small field sizes, the output factor that was measured with the 2D-Array ionization chamber was 2%, which was similar to the published data for the 6 MV photon beam measured with a 2D-Array (Martens *et al.,* 2000). The obvious discrepancy with the 2D-array can be interpreted as an overresponse to scattered radiation because the 2D-array is responsible for the field-size dependence of the output factor; this was shown to be particularly influential for the lower energy than for the higher energy.

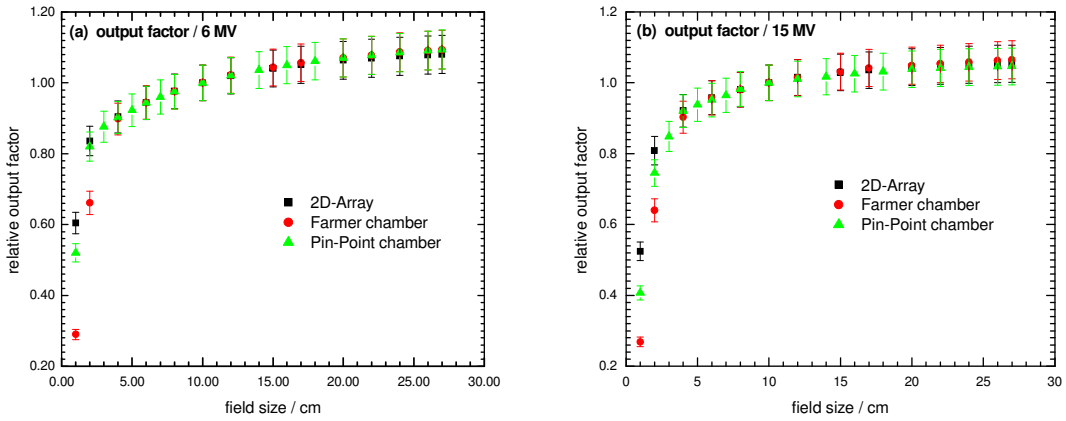

Figure 2.13. (a) and (b), the relative output factor as a function of the field size for 6 and 15 MV photon beams measured with the 2D-Array (black point), the Farmer chamber (red points) and the Pin-Point chamber (green points). The measurements were taken with the different detectors at a depth of 5 cm in solid-water equivalent slabs (a source-to-surface distance of 95 cm with 5 cm backscatter materials). Field sizes varied from 1 × 1 cm^2 to 27 × 27 cm^2.

2.3.5 Sensitivity

2.3.5.1 MLC movements

Figure 2.14 displays the results of the five chambers of the 2D-Array ionization chamber when one of the leaf banks (X1) of the MLC was moved from -2 to 0 cm (see figures 2.8, A - D). The obtained results for the chamber signal are from the acquisition of chamber 1 and chamber 5, which were partially covered by the leaf banks (X1 and X2), whereas chamber 2, chamber 3 and chamber 4 were all within the open portion of the field. Figure 2.14 shows the signals that were obtained from this acquisition. The 1-mm step movement of the MLC leaf bank (X1) was clearly detected by chambers 1 to 4, which were gradually irradiated with the field while the field decreased. The signal from chamber 5 was also influenced by the leaf position, which resulted from the Linac scatter components. The results show that the geometrical separation of the ionization chambers in the 2D-Array does not lead to a loss of sensitivity. The 2D-Array is sensitive to millimetric positional changes of the MLC systems. The results agreed well with the results that were obtained by Spezi *et al.* (2005).

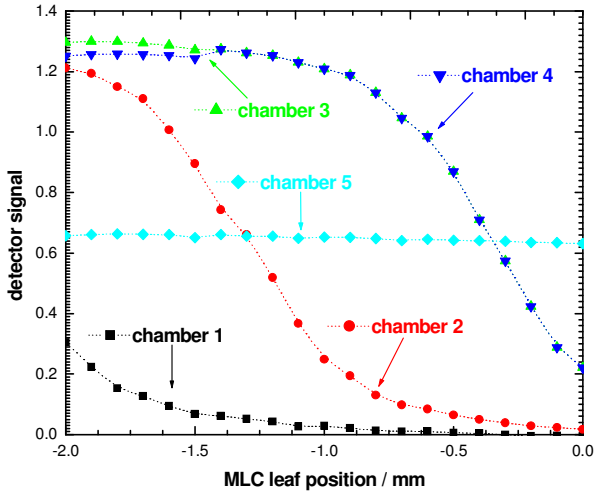

Figure 2.14.The 2D-Array detector sensitivity test; the results of the MLC movements of the 5 detectors that are shown in figure 3.8. The results from each detector are displayed for the entire position of the MLC leaves. The X1 leaf moves from -2 cm to 0 cm with 1-mm steps.

2.3.5.3 Leaf coverage

Figure 2.15 shows the plot curves of the 2D-Array signal from the four chosen chambers (A, B, C and D) that were covered by the MLC leaves against their positions. The curves show that the signals increased slightly as the positions of the chambers increased from the first position until approximately position 8. From position 8, it is clear that the slope of each signal curve as a function of the position is not constant for the four chosen chambers (A, B, C and D). The slopes from these positions reach their maxima between leaf positions 8 and 15. This behavior is common to all four chambers, which means that the sensitivity is greatest when the leaves are in the mid-position of any of the chambers.

The results also show that the highest gradient was obtained by chamber A; chamber B had the second highest gradient, chamber C had the second lowest gradient, and chamber D had the lowest gradient. The differences in the gradients for these chambers show that the leaf on the chamber A coverage position results in the maximum sensitivity to the dose measurements. Therefore, the best geometry positions the leaves in the middle of

each chamber and covers the chamber from the middle position up to the entire chamber. From the middle position, a deviation of 1-mm from both sides of the chamber can be useful to achieve the highest sensitivity. Therefore, the detection of the leaf can only be achieved by the leaf coverage position shown in chamber A; this position will be the best configuration for any MLC-position test.

The experiment also showed some geometric restrictions between the leaf position and the 2D-Array chambers; i.e., the leaf projections at 100 SSD on the 2D-Array chambers cannot be properly overlaid across all of the chambers; some of the leaves cover the chambers entirely, whereas other leaves are shifted to cover the chamber properly.

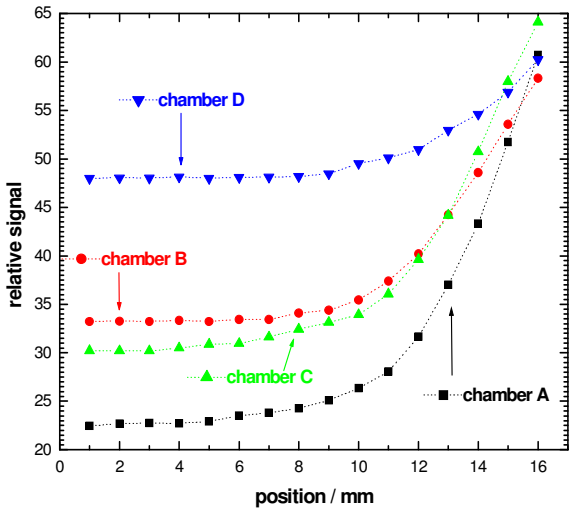

Figure 2.15. A plot of the detector signal against the position of the MLC leaves; the responses of the four chambers with different coverage configurations as the leaves moved from the initial position (p=1) to the end position (p=15) are shown.

2.3.6 Clinical applications

Figures 2.16 to 2.27 show the relative beam profiles for different wedge-modulated fields (15, 30, 45, and 60 degree wedges). The profiles for field sizes of 5 × 5 cm^2, 10 × 10 cm^2, 15 × 15 cm^2 and 20 × 20 cm^2 that were measured with the 2D-Array ionization chamber were compared with those measured with the Pin-Point chamber CC13 (Scanditronix/Wellhöfer) for 6 and 15 MV photon beam energies.

Figures 2.16 (a) and (b) depict a comparison between the wedge profiles for 5 × 5 cm^2 field sizes measured for 6 and 15MV photons, respectively. From these small fields, it can be observed that the 2D-Array ionization chamber has some limitations in its sampling capabilities. However, for these small field sizes, the relative percentage dose for the sharp edge of the wedge field is not accurately measured. This is because the field edges fall between two chambers in the 2D-Array as a result of the geometric configuration of the detector, which has an approximate chamber-to-chamber distance of 1 cm.

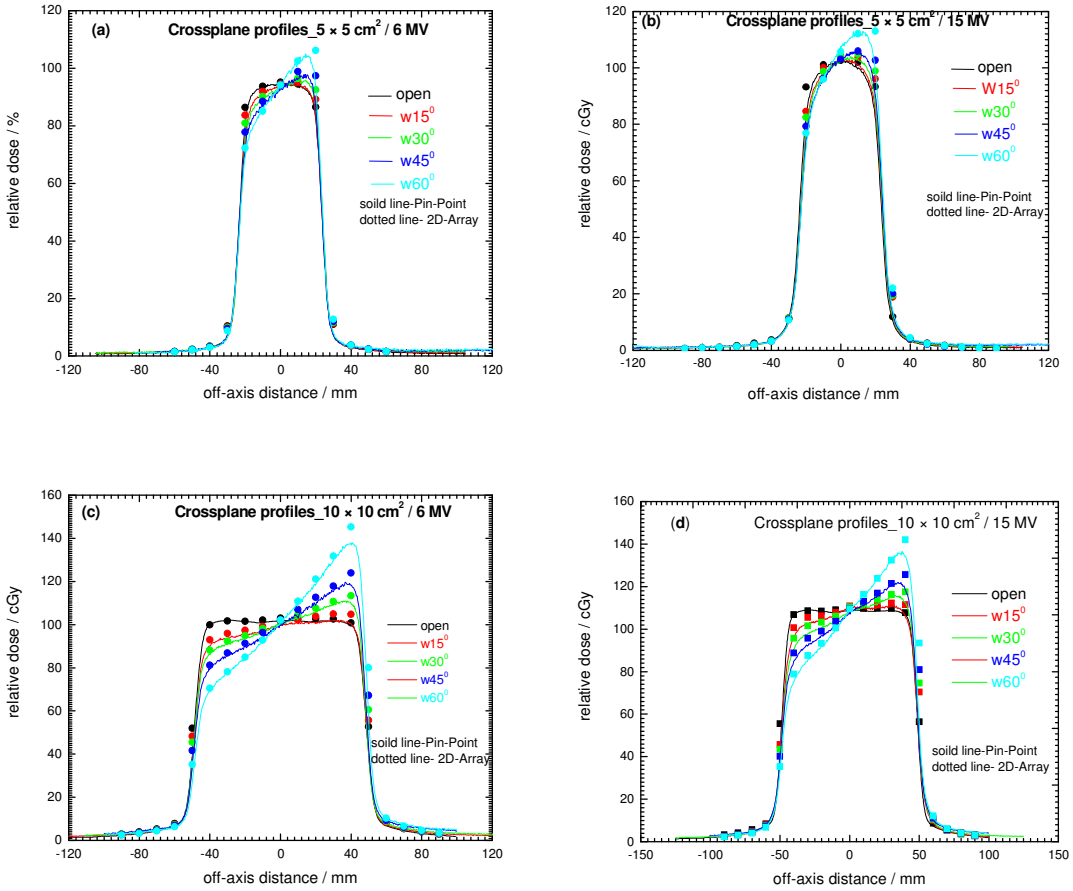

Figure 2.16. (a) – (d) Comparisons between the crossplane beam profiles for 5 × 5 cm^2 and 10 × 10 cm^2 fields measured with the 2D-Array (dotted lines) and the Pin-Point Chamber (solid line) for 15, 30, 45, and 60 degree wedges angles with 6 and 15 MV photon beams.

Figures 2.16 (c) and (d) show a comparison of the relative beam profiles for the 10 × 10 cm^2 field sizes measured with the 2D-Array and the Pin-Point chamber. The data agreed within a value of 1% for both the 6 and 15 MV energies for 15 and 30 degree wedges. For the 45, and 60 degree wedges, discrepancies at the 6 MV photon energy were 2% and 3%, respectively. The results for the 15 × 15 cm^2 field size are shown in figures 2.17 (a) and (b). Both 6 MV and 15 MV showed a difference of approximately 3% for all of the wedge profiles except for the 15 degree wedge profile, which showed a difference of 1.2%.

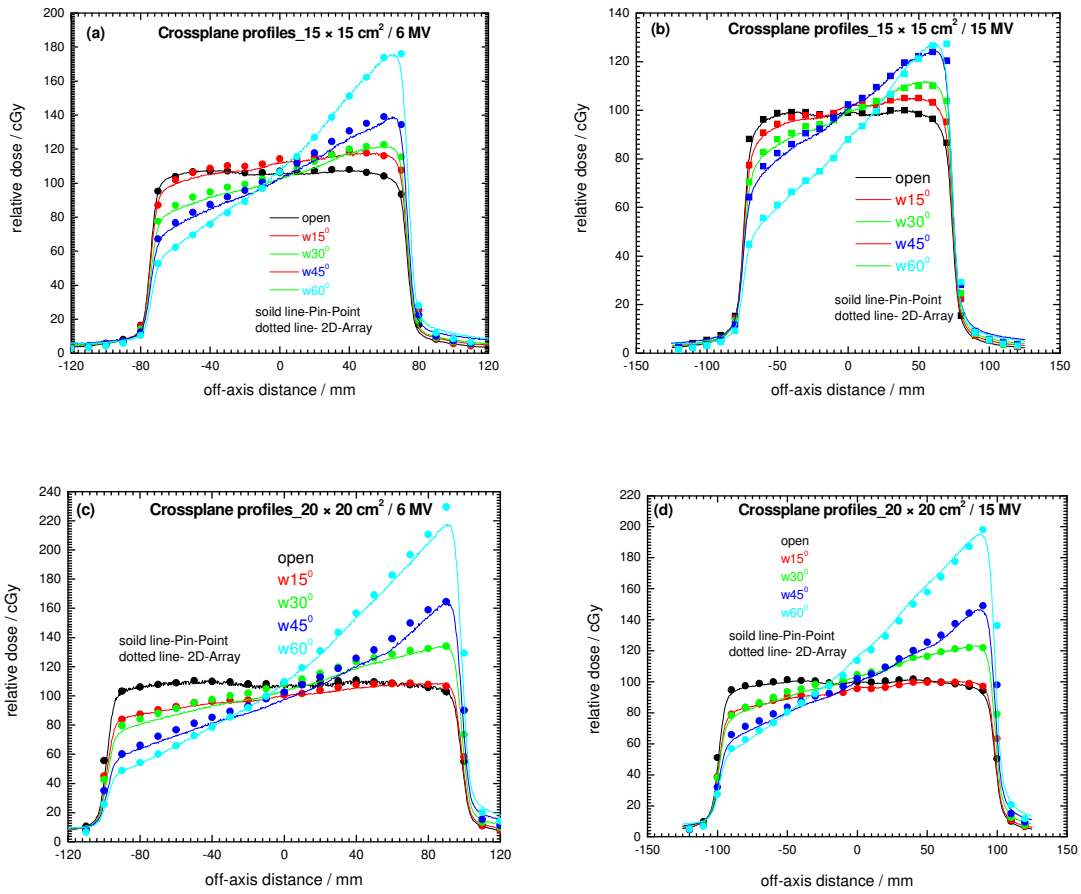

Figure 2.17. (a) –(d) comparisons between the crossplane beam profiles for 15 × 15 cm^2 and 20 × 20 cm^2 fields measured with the 2D-Array (dotted lines) and the Pin-Point chamber (solid line) for 15, 30, 45, and 60 degree wedges angles with 6 and 15 MV photon beams.

Figures 2.17 (c) and (d) show comparisons between the wedge profiles for a 20 × 20 cm^2 field with 6 and 15 MV photon beams measured with the 2D-Array and the Pin-Point chamber at a depth of 5 cm and an SSD of 95 cm. The measured beam profiles are shown for 15, 30, 45, and 60 degree wedges angles. The agreement between the 2D-Array and the Pin-Point chamber was good for all of the wedges. The profile that was produced by the 60° degree wedge with 6 MV showed a 4% discrepancy. For 15 MV, the comparison of the beam profiles measured with the two detectors showed differences of approximately 3% for all of the wedges. Nevertheless, the agreement among all of the datasets was very close, and the 2D-Array ionization chamber data accurately matched the Pin-Point ionization chamber relative beam profiles.

2.4 Summary and conclusion

As a part of the quality assurance of intensity-modulated radiation therapy (IMRT) using different dosimetric modalities, the dosimetric characterization of the 2D-Array Seven29 ionization chamber model (PTW, Freiburg, Germany) (PTW type 10024) was investigated. The results were validated, and the dosimetric characterization of the 2D-Array showed the suitability of the 2D-Array as a dosimetric tool in IMRT verifications. Based on the results, several conclusions can be drawn:

- The 2D-Array Seven29 ionization chamber model was very light (2.4 kg), and it was easy to handle and setup for accurate dosimetric verification. The entire process for setting up and warming up the 2D-Array took approximately 15 minutes.
- Calibration of the 2D-Array is important before it can be used for relative dosimetry (i.e., fluence maps verification) or for absolute dosimetry. The measurement results showed that the 2D-Array Seven29 ionization chamber response is reproducible within 1.5%.
- The responses of the 2D-Array ionization chamber were linear, with monitor units ranging from 2 to 500 for both 6 and 15 MV. The linear fit correlation coefficient was R^2=1. The determined signal of the detector was dependent on the radiation beam energy in the range of 6 to 15 MV. The 2D-Array results were confirmed with the data measured with the Farmer chamber (PTW type W30013).

- The output factor that was obtained with the 2D-Array was accurate in comparison with other detectors, especially for small field sizes, which was important because of the importance of these field sizes in IMRT applications. For the larger field sizes, the 2D-Array showed good results in comparison with other detectors.
- The 2D-Array demonstrated good sensitivity in the output of the Linac that was equipped with the MLC system for IMRT treatment. The methods that were used to verify the leaf position with the 2D-Array showed good results; therefore, these methods can be utilized to check the MLC position for quality assurance for the IMRT.
- The 2D-Array measured beam profiles closely matched the ion chamber measurements that were performed in a water tank for open and wedged modulated beams.

3. The dosimetric properties of an amorphous Silicon electronic portal imaging device for IMRT verifications

3.1 Introduction

Electronic portal imaging devices (EPIDs) have become an essential part of modern linear accelerators. Formerly, EPIDs were introduced to verify patient position. Recently, EPIDs have been employed for dosimetric verification purposes. This use of EPIDs is based on the conversion of the EPID signal into doses (Heijmen *et al.,* 1995; Chen *et al.,* 2006; Partridge *et al.,* 2002; Chang *et al.,* 2000; Pasma *et al.,* 1998). Another application of EPIDs is for Linac QA (Nicolini *et al.,* 2006a; Greer and Barnes 2007).

The evaluation of the dosimetric properties of EPID is important if EPIDs are to be used for dosimetric purposes. The dosimetric behaviors of a-Si EPIDs have been studied by several research groups. However, most of these groups have focused on two commercially available types of the a-Si EPIDs: the Elekta *iView GT system* and the Varian *PortalVision aS500/1000*. The dose-response behaviors of these types of a-Si EPIDs have been investigated by several authors. The stability of the response of the *iView*-type a-Si EPID has been studied for over two years and has been found to be equal to 0.5% for both 4 and 6 MV photon beams (Louwe *et al.,* 2004). In addition, the dose-response relationship is independent of the dose rate and is approximately linear with the integrated dose (Antonuk *et al.,* 1998; El-Mohri *et al.,* 1999). Winkler *et al.* (2005) studied the dosimetric properties of the *iView* a-Si EPID with respect to three photon beam qualities 6, 10 and 25 MV. McDermott *et al.* (2006) conducted a comparison study for the signal-to-monitor-unit ratio for three different types of a-Si EPIDs and found that all EPIDs exhibit under-responses for beams of few MUs. McDermott *et al.* (2004) and Louwe *et al.* (2004) investigated the use of the *iView* a-Si EPID and determined the amount of build-up needed for portal dosimetry.

The dosimetric characteristics of the *aS500* EPID support its use for IMRT verification (Greer *et al.,* 2003). Grein *et al.* (2002) also investigated the dosimetric properties of the

aS500 EPID for transit dosimetry and reported that the relationship between the EPID signal and the dose is linear for different field sizes and SSDs. The study concluded that more than 1% accuracy could be achieved when using certain dosimetric procedures. The basic dosimetric characteristics of the *aS500* EPID, such as the detector dose response, reproducibility, memory effect and field-size dependence, have been investigated by Van Esch *et al.* (2004). The short- and long-term reproducibility was were found to be excellent, and the memory effect was clinically insignificant.

Today, most modern radiation oncology clinics use Linacs that are equipped with EPIDs that can be used for imager verification. However, due to the increasing use of IMRT techniques in these clinics, there is a need for efficient methods for QA; EPID dosimetry may serve as an alternative to film dosimetry. Nicolini *et al.* (2006b) investigated IMRT dose verifications with an a-Si EPID and found that the EPID can be used for absolute dose measurements. A global calibration model for the use of an a-Si EPID for transit dosimetry has been developed by Nijsten *et al.* (2007a). Studies have shown that the a-Si EPID can be used for the dosimetric verification of dynamic IMRT fields (Greer *et al.,* 2007).

In general, EPIDs are complicated systems that need to be specially configured for dosimetry purposes, are not independent of the Linac control system that is being tested, and require substantial quality assurance (QC) (Van Elmpt *et al.,* 2009). Although a great deal of work has been done on the a-Si EPID dosimetric characterization, the lack of integrated software tools limits the usefulness of a-Si EPID detectors as standard dosimeters for performing QA dosimetric tasks in radiation oncology clinics. However, research efforts to enable EPID dosimetry to serve as an effective component of IMRT QA have been increasing (Nijsten *et al.,* 2007b; Van Elmpt *et al.,* 2008). Therefore, the dosimetric properties of amorphous silicon EPIDs and their applicability for IMRT verification are of current interest.

The aim of this chapter was to study and evaluate the dosimetric properties of our newly installed a-Si EPID for portal dosimetry purposes. The Siemens OptiVue EPID

(1000ART) was used for the measurements. The standard automatic calibration procedure of the a-Si EPID using dark images and flood-field images was conducted before the experimental procedure was performed. The properties assessed included the reproducibility, the a-Si EPID response as a function of the applied monitor units, the field-size dependence, the ghosting effect, the effect of the build-up, and the effect of the absorber thickness. In addition, the relationship between the EPID signal and the portal dose was explored. The method is an empirical approach to investigate the possibility of using the a-Si EPID for IMRT pre-treatment verification of step-and-shoot IMRT fields.

3.2 Materials and methods

The electronic portal imaging device (EPID) used in this study was an amorphous silicon (a-Si) flat panel portal imager (OPTIVUE 1000ART) attached to the Siemens ONCOR linac (Siemens Medical solutions, Concord, USA). The accelerator was equipped with 160MLC and 160 leaves. The accelerator operates at 6 and 15 MV under two dose-rate modes: A low dose-rate mode (50 MU/min for both photon energies) and a high dose-rate mode (300 MU/min for 6 MV and 500 MU/min for 15 MV). The dose-rate can be changed by varying the pulse repetition frequency. The flat imager detector used was a Perkin-Elmer XRD 1640-AG9detector with an active imaging area of 40 × 40 cm^2. The detector utilized 1024 × 1024 pixels, with a pixel size of 0.8 mm. The panel movements were limited to the vertical direction with variable distances that ranged from a 115 up to 160 cm source-to-detector distance (SDD). Lateral and longitudinal movements were not possible.

The panel could also be used to obtain a megavoltage cone-beam CT acquisition. The acquisition software used was Siemens Coherence Therapist Workspace software, version 2.0.09 (OPTIVUE 1000ART). The flat panel images were stored in a 2D cumulated grayscale value distribution averaged into a single conformal image from the subframes. A single frame could not be stored because the software collected all of the single frames and calculated the final image. The OPTIVUE 1000ART flat panel used an integration time of 80 milliseconds per frame. This enabled the manual delivery of several monitor units (MU) to form a portal image. Each image was then corrected for

pixel sensitivity before it was subtracted from the reference dark-field image. The dead-pixel map correction was also applied; with this method, a signal from a defective pixel was replaced by the main signal from neighboring non-defective pixels. For the correction of individual pixel sensitivities, profiles were obtained by making use of the flood-field images. These images were acquired for each beam energy, dose-rate and different source-to-detector distance (SDD).

The flat panel imager measurements were conducted at a source-to-detector distance (SDD) of 145 cm. This distance was used because most of the imager verifications for IMRT treatment are conducted at this level. The images were acquired after the completion of the treated field and were stored for later manipulation. Measurements were also conducted using different standard dosimeters as reference measurements. The point-dose measurements were performed using a Farmer ionization chamber (type 30013) connected to a UNIDOS electrometer (PTW, Freiberg, Germany). The "blue" water phantom system, which had scanning dimensions of $48 \times 48 \times 41$ cm^3, was used to measure the dose distributions. The SDD was set to 145 cm for all of the measurements and to a depth of maximum dose (d_{max}) for the corresponding energies under investigation. For the 2D relative dose measurements, a 2D-Array Seven29 ionization chamber detector was used. The Array consisted of 729 air-filled ionization chambers that formed a 27×27 matrix of detectors with an effective area of measurement of approximately 26×26 cm^2 (for more details, see chapter two). For all of the measurements, the relative EPID response (G_{EPID}/D_p) was set as the quotient of the average grayscale value (G_{EPID}) in the region of interest (ROI) of a 10×10 pixel area around the portal dose (D_p) measured at the same point for the same set-up. The average grayscale pixel value was calculated in the ROI of 10×10 pixels with ImageJ software. Both the EPID and ionization chamber measurements were conducted on the central axis. All of the ionization chamber measurements were corrected for temperature and pressure variations.

3.2.1 Routine calibration of the a-Si EPID

The calibration of the a-Si EPID usually requires the acquisition of two images: a flood-field (FF) image and a dark-field (DF) image. These images are also part of the configuration process for standard imaging with the EPID. For dosimetric purposes, a further correction for the response of the EPID must be made. The dark-field (DF) image was used to correct for the dark current in each pixel, and it was acquired without radiation to record the pixel offsets. The flood-field (FF) image was acquired while irradiating the EPID with an open "uniform" field. The flood-field image was used to correct for sensitivity differences between the individual pixels and to correct for the beam profile with the acquisition software. The calibration procedure was conducted periodically with 6 and 15 MV photons at a low dose rate (50 MU/min for both energies) and at a high dose rate (300 MU/min for 6 MV and 500 MU/min for 15 MV) for different ranges of source-to-detector distances (SDDs), which ranged from 120 to 160 cm. A dead-pixel map correction was also applied. The dead-pixel map correction indicates the replacement of the signal value of faulty pixels with the mean signal value of the normal pixels neighboring the faulty pixels.

3.2.2 Detector reproducibility

A reproducibility test of the flat panel imager was necessary before the panel could be used for dosimetric comparisons of the delivered dose in terms of the dose difference and the distance to agreement. This was important because the EPID had to be used to record not only the relative dose measurements but, also the absolute dose variations. Therefore, the detector reproducibility had to be proven over both a short and long period (Winkler *et al.,* 2005; Talamonti *et al.,* 2006). In the present study, the short-term reproducibility was evaluated on the basis of 20 subsequent measurements in which 20 MU were delivered using a 10 × 10 cm^2 field size and 6 and 15 MV photon beams. The long-term reproducibility was evaluated by acquiring 10 consecutive measurements. The EPID was exposed under identical conditions using a 6 MV photon beam. The experiment was repeated every two weeks for a period of 3 months. For long- and short-term reproducibility, the average grayscale pixel value was measured within an ROI of 10 × 10 pixels. For the experimental set-up, see figure 3.1.

3.2.3 The a-Si EPID response as a function of applied monitor units

The calibration methods of the EPIDs are based on the assumption that the reading of the EPID is proportional to the delivered dose. This relationship has been investigated by several authors (Greer *et al*., 2003; Chen *et al.,* 2005; Winkler *et al.,* 2005; and Nijstein *et al.,* 2007). The a-Si EPID response, G_{EPID}/D_p, as a function of the applied monitor units (MU) were investigated. G_{EPID} was the average grayscale value in an ROI of 10 × 10 pixels around the beam axis. The portal dose,D_p, was measured at the beam axis at a depth of maximum dose (d_{max}) in a water phantom using a Farmer ionization chamber (PTW type 30013). The distance from the source to the detector surface was 145 cm, which was equal to the source-to-detector distance (SDD) of the EPID. Because the EPID and portal doses could not be measured simultaneously, both the ionization chamber and the EPID measurements were performed sequentially at all times. The EPID was positioned at a fixed source-to-detector distance (SDD) of 145 cm, and a varying dose was delivered with monitor units (MUs) in the range of 5 to 1000 MUs. The low starting values were used because for the application of the EPID for the dosimetry of IMRT fields, low MUs are possible. In the case of the step-and-shoot technique, a field can be composed of segments as short as a few MUs. The corresponding irradiations were also performed in one session by using the maximum available nominal dose-rate (i.e., 300 MU/min at 6 MV and 500 MU/min at 15 MV). Images were acquired at 10 × 10 cm^2 and centered at the central axis for all of the measurements. The collimator angle and the gantry angle were both set to zero degrees.

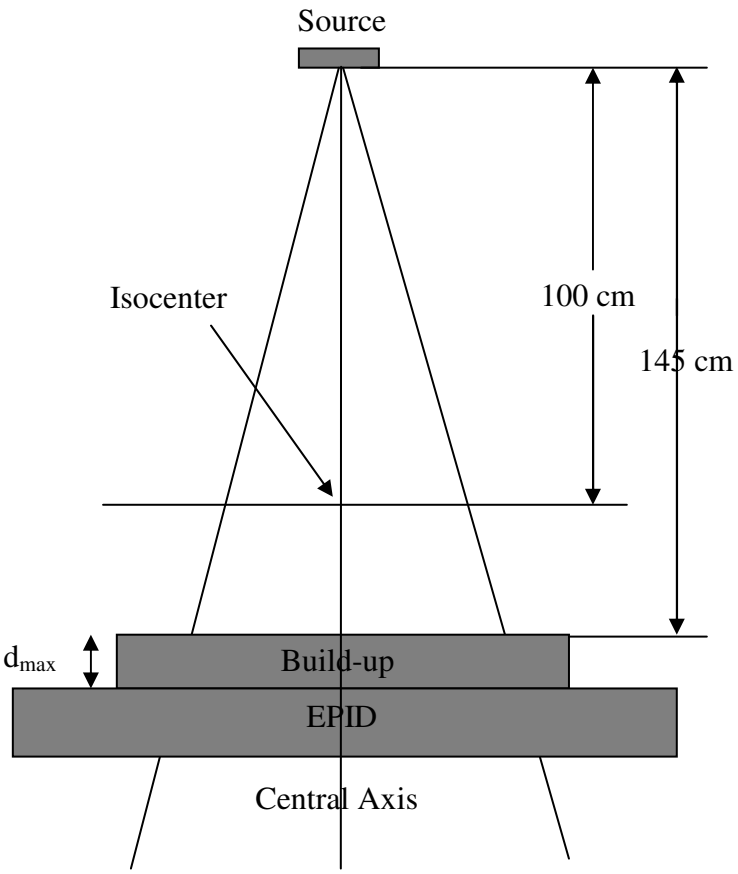

Figure 3.1.The geometric set-up of the experiment.

3.2.4 Field-size dependence

The field-size dependence was determined to assess the response of the a-Si EPID as a function of the field size. G_{EPID}/D_p, ratios were determined for a set of square fields defined by the MLC starting at 1 × 1 cm^2 and increasing up to 25 × 25 cm^2 without an absorber in the beam. Measurements were conducted at a source-to-detector distance (SDD) of 145 cm for 6 and 15 MV photons. All irradiations were performed by delivering 100 MU. For each setting, two EPID images were acquired with no build-up added on the EPID. The average grayscale value was recorded from the average of the region-of-interest (ROI) as described above. To calculate the EPID response, integrated readings were obtained in a water phantom on the central axis using the Farmer ionization chamber (0.13 cm^3 PTW, Freiburg, Germany) for each field size. This calculation was performed at the corresponding depth of maximum dose for each energy

level and at the SDD of 145 cm. Both sets of measurements were normalized to 10 × 10 cm^2 field-size values.

3.2.5 Dose-rate linearity

The linearity of EPID to dose-rate variations was investigated by monitoring the grayscale value on the beam axis for a static field. To modify the dose rate, the SDD was varied by the distance of the EPID below the isocenter. The EPID was placed at 15, 20, 25, 30, 30, 40, 45, 50, 55, and 60 cm below the isocenter. At each distance, a dose of 100 MU was delivered to a 10 × 10 cm^2 open field. The EPID images were collected, and the average grayscale pixel value was calculated in the region of interest (ROI) of the 10 × 10 pixel area at the center of the field around the beam axis for 6 and 15 MV photons.

3.2.6 The ghosting effect of the a-Si EPID

The ghosting effect of the a-Si EPID, which is also referred to as the memory effect, is generally defined as artifacts in the image caused by signals being present in frames following the frame in which the image was generated (McDermott *et al.,* 2003; Winkler *et al.,* 2005). The a-Si EPID experiences a ghosting effect, and this effect has been investigated by several authors (Greer *et al.* 2003; McDermott *et al.,* 2003; Winkler *et al.,* 2005; Nijsten *et al.,* 2007a). The ghosting effect of the a-Si EPID was performed as follows: an image with a small field size of 5 × 5 cm^2 was acquired, followed by the acquisition of two images with a large field size of 15 × 15 cm^2. Each field was delivered as soon as possible after the previous field. An image was acquired for each field, and the acquired images of the two large fields were compared to determine whether the pixel value was high as a result of the ghosting effect. The time applied between the irradiations was a few seconds. The ghosting measurements were performed for both 6 and 15 MV photons. The SDD was set at 145 cm for all the measurements. The test was repeated in several groups of measurements:

i) 500 MUs was delivered to the small field (5 × 5 cm^2), and 10 MUs was delivered to each of the large fields (15 × 15 cm^2). This group of measurements was intended to determine the maximum extents of the ghosting effects. ii) Next, 50 MUs was delivered

to the small field (5 × 5 cm^2), and 10 MUs was delivered to each of the large fields (15 × 15 cm^2). This group of measurements, together with the previous group, would show the extent to which the ghosting effects depend on the dose of the previous irradiation. iii) Finally, 50 MUs was delivered to each field.

The acquired images from the different sets of measurements were analyzed by measuring the grayscale values using ImageJ software at the center of the field for the large field sizes and making comparisons. The signal values were recorded and then normalized to the highest value at the field center. Line profiles were also drawn horizontally for the two images to evaluate the ghosting effect. The ghosting signal was calculated as a percentage difference between the obtained profiles along the images.

3.2.7 The build-up effect of the a-Si EPID

The response of the a-Si EPID as a function of the amount of build-up onto the detector surface was investigated in this section using 6 and 15 MV photon beams. The EPID measurements were conducted with the outer surface of the EPID at a source-to-detector distance (SDD) of 145 cm. A field of 10 × 10 cm^2 at the isocenter was projected at the extended SDD to give a field of 14.5 × 14.5 cm^2. The dose was 100 MUs, and the dose-rates were 300 and 500 MU/min for 6 and 15 MV photons, respectively. The build-up material used was the solid-water phantom (GAMMEX rmi, Middleton, WI), which was positioned at the EPID surface. A series of measurements were obtained with depths ranging from 0.1 cm to 4.0 cm on the EPID. Comparative measurements were performed in a solid-water phantom with an ionization chamber (PTW type 30013) positioned on the beam axis at a distance of 145 cm. Solid water was used to provide a range of build-up similar to that used on the EPID. The ionization chamber measurements were acquired with 100 MUs exposures. Figure 3.1 shows the experimental set-up.

3.2.8 The a-Si EPID response versus the thickness of the solid water

The response of the EPID can be changed with spectral changes in the photon beam by introducing an absorber in the beam path. This will be present for different patient thicknesses in the path of the radiation field. The response of the EPID was investigated

using a solid-water phantom for a range of thicknesses varying from 2 to 40 cm. The solid water was placed on the table at an SSD of 100 cm. Measurements were performed for a 10 × 10 cm^2 field-size with 100 MUs and dose rates of 300 MU/min and 500 MU/min for both 6 and 15 MV photons, respectively. The center of the absorber was located at the isocenter of the treatment unit at all times. The a-Si EPID at a distance of 145 cm without using any build-up material on the panel and the surface of the EPID was considered as a detector surface.

The measurements were also conducted using a Farmer ionization chamber with the same configuration to compare the results. The response of the a-Si EPID for various thicknesses of the solid-water phantom could then be evaluated by comparison with the ionization chamber measurements. The EPID and the ionization chamber data were normalized to the maximum reading obtained. The transmission curves were measured by analyzing a 10 × 10 pixel region of interest (ROI) along the central axis of the beam for the 6 and 15 MV photons and the field size of 10 × 10 cm^2.

3.2.9 An electronic portal imaging device as a dosimeter

EPIDS were purposely developed for on-line patient setup verifications. However, the acquired image information is related to the dose delivered to the EPID, and EPIDs are currently used as dosimeters. A study was conducted to evaluate the EPID as a dosimeter by comparing its response with that of an ionization chamber.

3.2.9.1 Calibration of the EPID

The calibration procedure of the a-Si EPID aimed to convert the EPID images into a 2D water equivalent dose distribution measured in the detector plane at a depth of the maximum dose (d_{max}). The setup of the calibration experiment of the EPID was as shown in figure 3.2a. Solid water (GAMMEX rmi, Middleton, WI) equivalent slabs of approximately 30 × 30 cm^2 were added as build-up layer materials at the top surface of the EPID. Slab thicknesses of 0.7 and 2.0 cm were used for the 6 and 15 MV photon beams, respectively. The EPID calibrations were determined for 6 and 15 MV photons, and all of the EPID images were acquired by using a field size of 10 × 10 cm^2 using 6 and

15 MV photons operating under high dose-rate mode. The EPID images were acquired for a range of source-to-detector distances (SDDs); no attenuator was used for these images. The EPID positioning range was varied from 115 to 145 cm, and at each position, 100 MUs were delivered. Thus, the radiation dose was varied by moving the EPID for a range of distances. The EPID images were collected, and the average grayscale pixel value was calculated in the region of interest (ROI) of the 10 × 10 pixel area at the center of the field around the beam axis.

To determine the relationship between the dose and the measured EPID grayscale value, the ionization chamber measurements were performed using a Farmer ionization chamber (PTW type 30013) and a UNIDOS electrometer (PTW, Freiburg, Germany).The ion chamber was placed at corresponding SDDs at the same as the EPID and inserted in solid water slabs (30 × 30 cm^2 in area) (GAMMEX rmi, Middleton, WI) to a depth that would achieve the maximum dose; approximately10 cm of solid water was also placed underneath to provide backscatter, as shown in figure 3.2b. For the relationship between the dose measured and the EPID grayscale pixel values at the central axis, a linear plot relation between the measured dose and EPID grayscale values was obtained. This plot "calibration curve" was used to convert the EPID response into an absolute dose response.

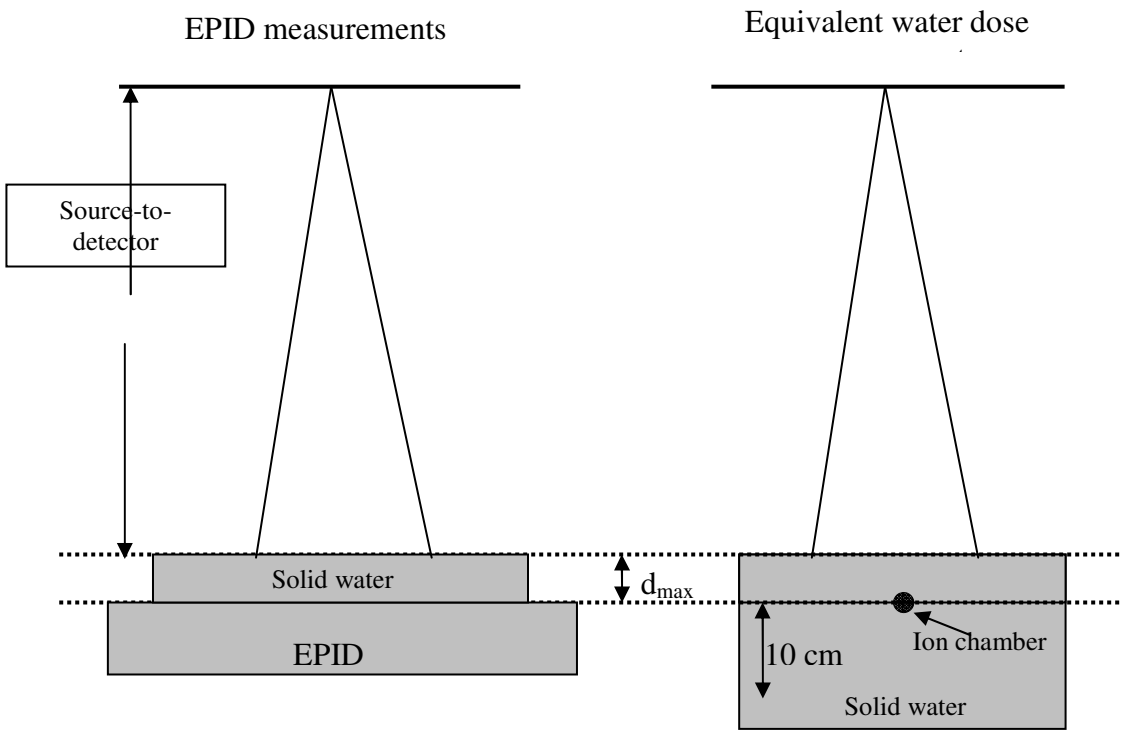

Figure 3.2. The experimental set-up of the position of the (a) EPID and (b) ion chamber. The ion chamber is embedded in solid water with 10 cm of backscatter.

For the calibration of the EPID as a 2D dosimeter, the EPID images were acquired at an SDD of 145 cm for a 10 × 10 cm^2 and 15 × 15 cm^2 field sizes at the isocenter for 6 and 15 MV photons operating under the high dose-rate mode. The 2D-Array Seven29 detector was irradiated at the same setup and under the same conditions. Subsequently, a table was created between the measured dose and the EPID grayscale pixel values. The EPID images' grayscale values were converted into absolute dose values using the calibration curve. This was done by plotting the datasets using VeriSoft software. Both EPID and 2D-Array Seven29 detector dose profiles were normalized to the dose value on the central axis.

3.2.9.2 The evaluation of the fluence maps measured using EPID

For the 2D dose evaluations, a head and neck IMRT plan was evaluated by using an a-Si EPID and the 2D-Array Seven29 ionization chamber. The plan contained three fields, and each field in the plan was calculated separately using a field-related approach. The SSD selected was approximately111.5 cm, and 3.5 cm was selected for the build-up of the

thickness to deliver the dose at 115 cm SDD, which was equivalent to the depth of the maximum dose for the 15 MV photon energy. For the EPID measurements, the EPID images were acquired separately for each field. The EPID was positioned at 115 cm SSD, with an extra build-up on the top surface of approximately 2.2 cm. The build-up was chosen according to the energy used for the intensity-modulated field. For the 2D-Array measurements, the same EPID setup was used to acquire the IMRT fluencies. A 2.5 cm thickness was used as build-up layer so that the effective point of measurement of the 2D-Array fell at the depth of the maximum dose. For the comparisons of the fluence maps, the acquired EPID fluence images were converted to relative fluence maps according to the calibration procedures. Subsequently, the data were calibrated and normalized to the maximum obtained dose for the comparisons. The obtained fluence maps were aligned and then rescaled. The gamma evaluation criterion was used to evaluate the agreements in dose values from the EPID and the 2D-Array Seven29 detector. The distance to agreement was set at 3 mm and the dose difference at 3% for comparisons.

3.3 Results and discussion

The experimental procedures for determining the dosimetric properties of the a-Si EPID attached to the Siemens ONCOR Linac (Siemens Medical Solutions, Concord, USA) were described above. The dosimetric properties were evaluated in terms of the calibration of the a-Si EPID, the reproducibility, the a-Si EPID response as a function of applied monitor units, the field-size dependence, the dose-rate linearity, the ghosting effect, the build-up effect, the a-Si EPID response versus solid water thickness and the use of EPID as a dosimeter for measuring the dose; comparisons of the a-Si EPID with the 2D-Array Seven29 were used to evaluate the IMRT fluence maps. This section presents the results of the experiments.

3.3.1 The routine calibration of the a-Si EPID

The standard automatic calibration of the EPID using a flood-field image with a uniform radiation field and the dark image (non-irradiated image) was performed using the Siemens Coherence Therapist Workspace software, version 2.0.09 (OPTIVUE

1000ART). This procedure was conducted according to the protocol recommended by the manufacturer and according to the calibration guidelines (ONCOR Impression operator's manual). The dosimetric measurements of the a-Si EPID were performed after the calibration.

3.3.2 Detector reproducibility

Figures 3.3 (a) and (b) show the results of the reproducibility tests for the a-Si EPID. The graph shows measurements versus a-Si EPID average grayscale pixel values for 10 ×10 pixels of the acquired EPID images. The a-Si EPID short-term reproducibility characteristics were similar for both beam qualities, as shown in figure 3.3 (a). For the same number of MUs applied, average grayscale values did not vary significantly and were approximately 0.99 and 0.97%, and the standard deviation values of the detector were 0.2% and 0.3% for 6 and 15 MV, respectively. Figure 3.3 (b) shows the long-term reproducibility test for 10 consecutive measurements obtained over a period of 3 months. The long-term reproducibility was found to be within ±1.7% over a period of 3 months for the 6 MV photon beam.

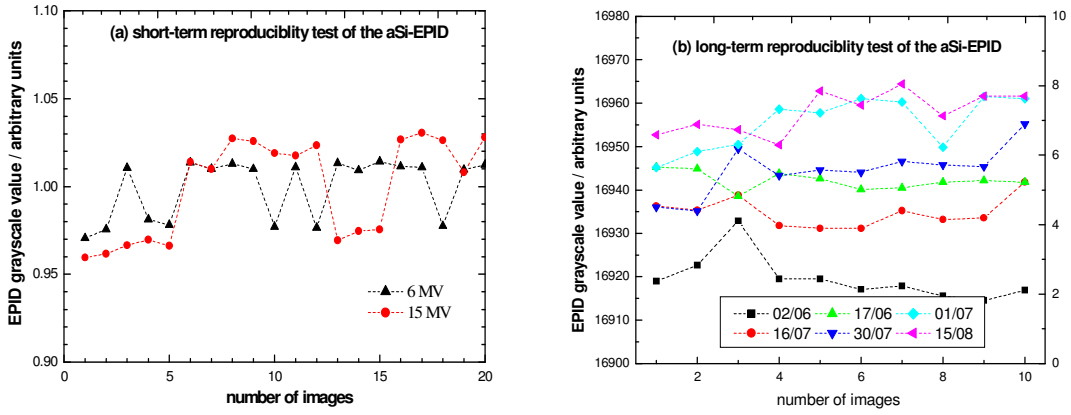

Figure 3.3 (a) The variation in the average grayscale values for 20 consecutive measurements of short-term reproducibility. (b) The variations in grayscale values for 10 consecutive measurements of long-term reproducibility over a 3-month period.

3.3.3 The a-Si EPID response as a function of applied monitor units

The relationship between the dose responses of the a-Si EPID as a function of the applied MUs was investigated. Figure 3.4 shows the relationship between the EPID response and the applied MUs for a range of 5 to 1000 MUs. The data were fitted in a semi-log graph. The results showed almost identical behavior for both beam qualities; 6 and 15 MV photons. In addition, the response of the a-Si EPID decreased in the region of low doses for both energies, and this was more obvious for the 15 MV. The a-Si EPID response (relative to the normalization value of 30 MUs) was higher by 2.1, for 6 MV photons and 2.8% for 15 MVphotons for 1000 MUs, whereas for the doses at 10 MU, the reduction in the a-Si EPID response was 4.8% and 5.8% for the 6 and 15 MV photons, respectively. The a-Si EPID response across the panel became stable at an MU greater than 200, and in agreement with Greer *et al.* (2007). The a-Si EPID responses are similar to those reported by previous studies conducted by *Greer et al.* (2007) and McDermott *et al.* (2006) for Varian a-Si EPIDs and Winkler *et al.* (2005) for Elekta iView^{GT}. Winkler and George (2006) reported an increase in detector sensitivity of 1.7 – 2.8% for Elekta iView^{GT} in a range of 30 to 500 MUs. At lower than 20 MUs, the a-Si EPID reduced the sensitivity, which is attributable to the instability in the accelerator dose-rate and the energy during start-up (Winkler *at al*., 2005).

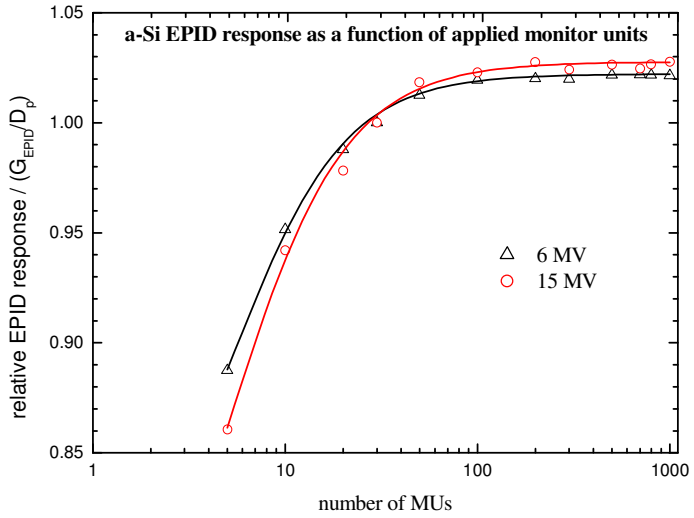

Figure 3.4. The a-Si EPID response as afunction of applied monitor units (MU) for 6 and 15 MV photons. The results were normalized to 30 MUs.

3.3.4 Field-size dependence

Figure 3.5 shows the results of the relative EPID response with the field size of the a-Si EPID for the 6 and 15 MV photons. The measurements were corrected for the changes in output using the Farmer readings, and the results were normalized to the values of the 10 × 10 cm^2 field size. The resultant graphs were evaluated. In figure 3.5, both under-response and over-response areas (relative to a 10 × 10 cm^2 field) can be distinguished. For small field sizes, the EPID response shows less response dependence on the field size up to the 10 × 10 cm^2 field; as the field size increases, the EPID response shows a clear dependency on the field size and energy. This effect is caused by changes in scatter with increased field size. Scatter has a low energy component; its effect on the EPID's phosphor response is enhanced (due to presence of high atomic number component in the phosphor material) (Van Esch *et al.,* 2004; Greer *et al.,* 2003).

The pattern is the same for the two energies with an under-response for small fields and an over-response for the bigger field ranges. This result is caused by the scatter contributions from the head, in which the head scatter is more for the lower energy than for the higher energy. The under-response reach 10.0 ± 0.7% and 5.7 ± 0.4% for the 6

MV energy for the smallest square field sizes of 1 × 1 cm and 3 × 3 cm, respectively. For the 15 MV the values were 8.5 ± 0.6% and 5.2 ± 0.6% for the 1 × 1 cm^2 and 3 × 3 cm^2 field, respectively. The over-response values for the largest square field were 4.7 ± 0.3% and 7.4 ± 0.4% for the 6 and 15 MV energies, respectively.

The EPID response was also in close agreement with other studies for different field sizes. Greer *et al.* (2003) measured an under-response of 2.0% for a 4 × 4 cm^2 field and 2.5% for a 24 × 24 cm^2 field (relative to a 10 × 10 cm^2 field) but, did not correct for EPID off-axis response. Van Esch *et al.* (2004) studied the response of the EPID for varying field sizes and fitted the field size for the two different energies separately using a second-order polynomial. Their approach also depended on the source-to-detector distance (SDD).

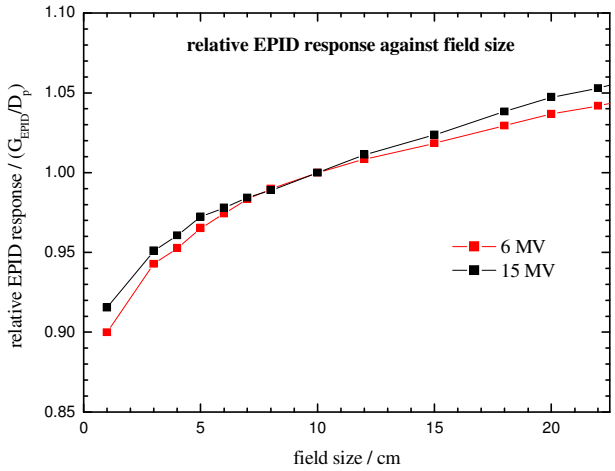

Figure 3.5. The relative response of the a-Si EPID (the ratio of the grayscale value, G_{EPID}, divided by the portal dose, D_p as a function of the field size for the 6 and 15 MV photons. Results were normalized for a 10 × 10 cm^2 field.

3.3.5 Dose-rate linearity

The images were obtained at different SDDs delivering 100MU at a repetition rate of 300 and 500MU/min for 6 and 15 MV. These images were analyzed, and the mean value of the central 10 × 10 pixel region was calculated and plotted. The distance from the source to the detector gives an inverse square factor that can then be converted into a dose-rate

(Gy/min). These data are plotted as shown in figures 3.6 (a) and 3.6 (b). A linear function was fit to the data. The linear regression analysis produced a coefficient of determination $R^2 = 0.999$ for all the fits. The linear fits also indicated proportionality constants showing that the detector is proportional over the entire measured range and does not deviate from the inverse square behavior. The dose-rate linearity of the EPID has been previously reported (Van Esch *et al.,* 2004). Thus, only verification was performed in this thesis to establish that the EPID at SBAH performs as expected.

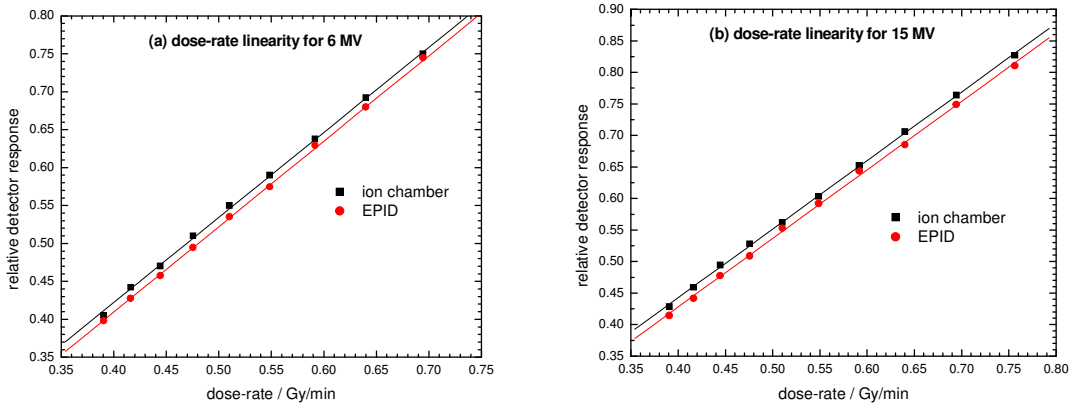

Figure 3.6. The variation of the dose values as a function of the source-to-detector distance (SDD) measured using the ion chamber and the a-Si EPID for the (a) 6 MV and (b) for 15 MV photons.

3.3.6 The ghosting effect of the a-Si EPID

The ghosting effect of the a-Si EPID was investigated. A comparison of the images for the measurements of series a, b and c for the ghosting effect is shown for the two different beam qualities; 6 and 15 MV photons. Figures 3.7 and 4.9 depict the acquired images with lines displayed for the profiles obtained along the horizontal direction or along the axis of the images for the 6 and 15 MV photons. A 15 × 15 cm^2 treatment field was acquired immediately after exposing the flat panel using a 5×5 cm^2 field. Within the central area of the 15 × 15 cm^2 field, the grayscale values were increased and compared to the values of the flat panel imager that acquired after a period of 15 seconds without image acquisitions. Figures 3.8 and 3.10 depict the obtained profiles along the EPID images for the different series of measurements. For series a, the average differences in

the grayscale values in the central area were 0.40 ± 0.20 % and 7.00 ± 1.00% for 6 and 15 MV, respectively, whereas the differences in grayscale values outside the small-field area were 0.20 ± 0.01% and 0.70 ± 0.20% for 6 and 15 MV, respectively. For series b and c, the signal values were considerably lower for both beam qualities. Overall, the 15 MV grayscale profile showed the ghosting effect more clearly than the 6 MV grayscale profiles, which was caused by the higher dose-rate for the 15 MV photons (because of a shorter period of time to deliver the dose) than for the 6 MV photons. The differences in the responses emphasize the necessity of individualized calibrations for EPID for each energy if they are to be used for dosimetry purposes (Winkler and George *et al*., 2006).

Overall, the ghosting effect for 15 MV was very clear at the first set of measurements (a); for the b and c sets of measurements, the effect is considerably smaller. The results also showed that the ghosting effect of the imager is greater for a short interval between images. From the obtained results, we can observe that the ghosting effect is small and that it is negligible in short time intervals such as 15 seconds. The results also showed that the amount of ghosting is dependent on the number of MUs used in the previous irradiation.

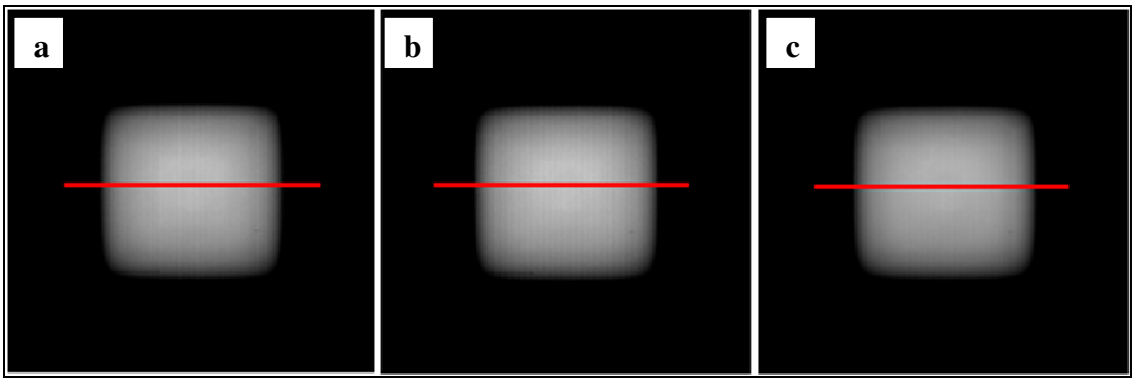

Figure 3.7. A comparison of the acquired images for MV photons; images a, b and c are from measurements of series a, b and c, respectively.

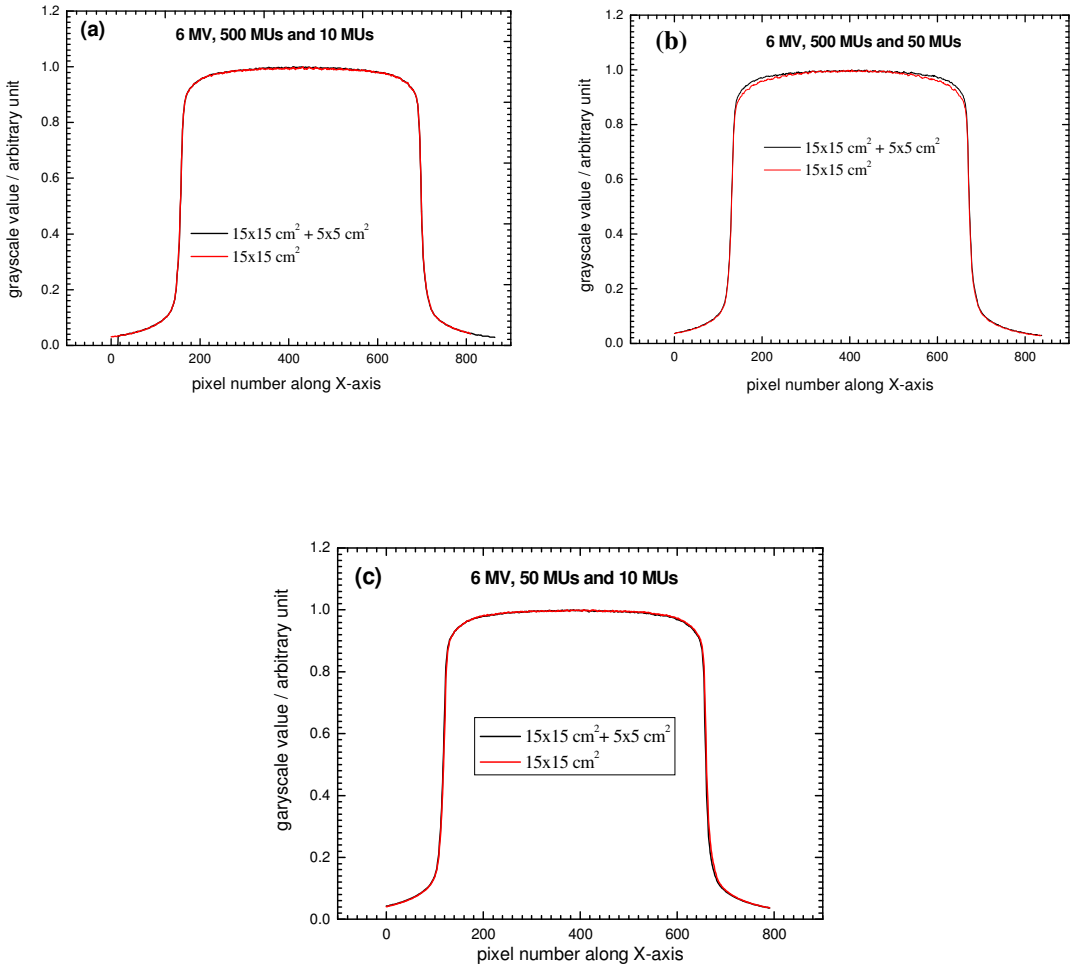

Figure 3.8. A plot profile measured along the image showing the a-Si EPID grayscale values versus the pixel number for the two large fields after the delivery of the small field for 6 MV photons.

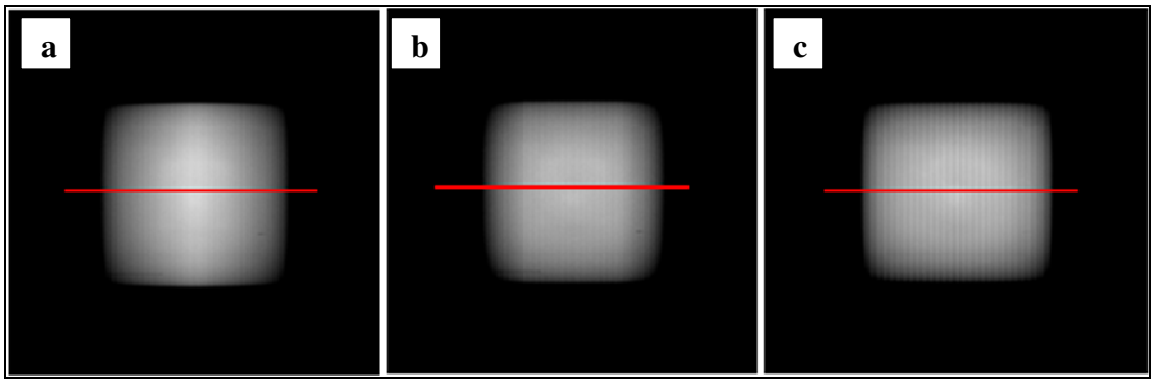

Figure 3.9. A comparison of the acquired images for 6 MV photons; images a, b and c are from measurement series a, b and c, respectively.

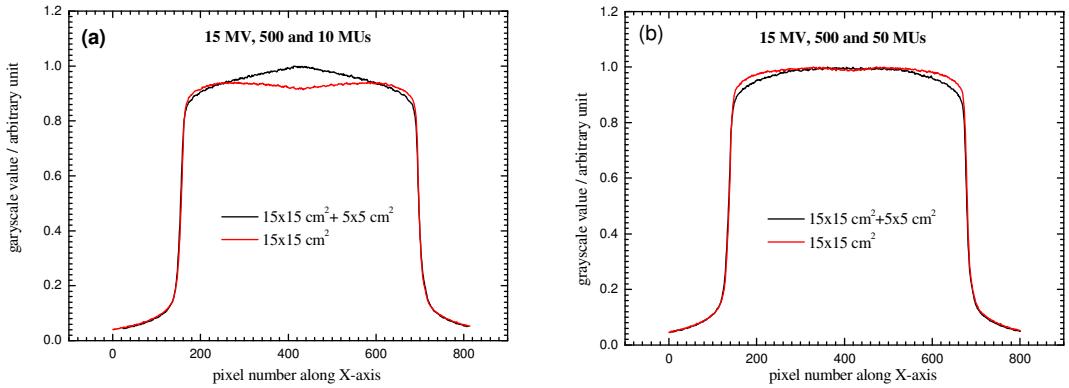

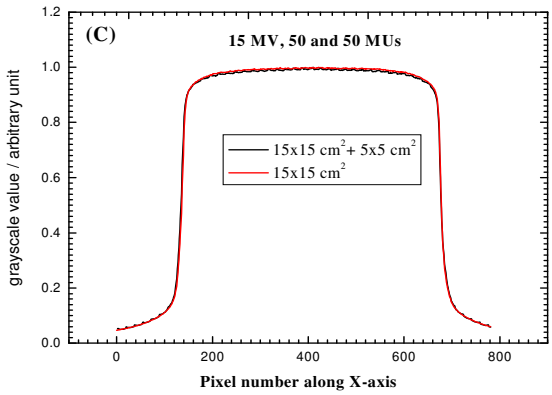

Figure 3.10. A plot of a line profile showing the EPID grayscale values versus the pixel number for the two large fields after the delivery of the small field for 15 MV photons.

3.3.7 The build-up effect of the a-Si EPID

The a-Si EPID/ion chamber measurements as a function of absorbing material are normalized to their maximum values. For both energies, the a-Si EPID behavior deviates significantly from the dose-to-water measurements: the dose maximum is obtained in a shallower depth for the a-Si EPID measurements compared to the ionization chamber measurements. In addition, the dose maximum plateau region is wider in the a-Si EPID measurement series. Figures 3.11(a) and (b) show a plot of the EPID grayscale value/signal response versus the depth for 6 and 15 MV, respectively. This depth acted as a build-up and was placed on the top of the EPID. As expected, the signal from both instruments increases as a build-up material is placed above until a certain depth, where the signal reaches a maximum. After the maximum is reached, the signal and dose received decreases with depth. Ion chamber measurements are known to be proportional to the dose received; thus, the depth at which the maximum ion chamber signal occurs will be the depth at which the maximum dose is imparted to the material. Because the EPID has some inherent build-up, it gives the maximum signal with less extra build-up materials added on top. The difference between the two depths of the maximum signal can be considered the amount of water-equivalent material that the inherent build-up of the EPID is contributing. This can be determined for each photon's energy under investigation.

Figure 3.11 (a) shows the EPID grayscale value/signal response as a function of depth for 6 MV photons for both detectors. The maximum depth value for EPID occurs at 0.71 cm; the stated average value with standard deviation is 0.71 ± 0.03 cm, whereas for the ion chamber results, the d_{max} was found to be 1.11 ± 0.09 cm. Figure 3.11 (b) shows the EPID grayscale value/signal response as a function of depth for 15 MV photons for both detectors. The maximum depth value for EPID occurs at 2.02 cm; the stated value is 2.02 ± 0.05 cm, whereas for the ion chamber results, the d_{max} was found to be 2.48 ± 0.04 cm. By subtracting the EPID's maximum grayscale value depth from the d_{max} of the ionization chamber, the effective water-equivalent depth inherent in the build-up material on the a-Si EPID can be calculated as follows:

For 6 MV: 1.11 ± 0.09 - 0.71 ± 0.03 = 0.40 ± 0.06 cm;

For 15 MV: 2.48 ± 0.04 - 2.02 ± 0.05 = 0.46 ± 0.01 cm.

The inherent build-up on the a-Si EPID was found to be 0.40 ± 0.06 cm for 6 MV and 0.46 ± 0.01 cm for 15 MV. The results show that the water-equivalent depth values of the inherent build-up of the EPID are the same with the uncertainty for different photon energies. This build-up must be considered when adding a solid-water phantom material on top to achieve the depth of the maximum dose of the detector. The results will be useful for the a-Si EPID calibration for dosimetric purposes.

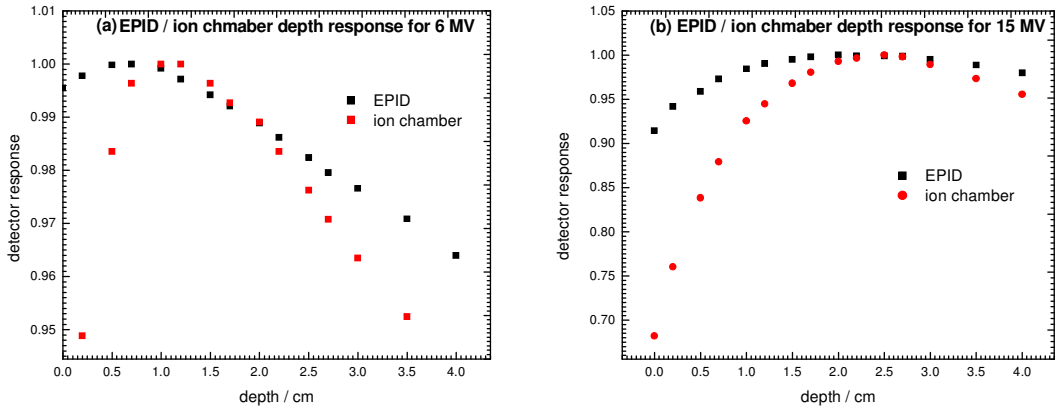

Figure 3.11. (a) and (b) present the grayscale values measured by the a-Si EPID versus the water-equivalent depth (cm) for 6 and 15 MV photons. The depth was placed on the top of the EPID.

3.3.8 The a-Si EPID response versus the thickness of the solid water

The intensity of a photon beam is reduced as the absorbing material thickness is increased. Figure 3.12 (a) and figure 3.12 (b) show the reduction in photon intensity measured with the EPID and ion chamber responses when solid-water phantom materials of various thicknesses were placed between the source and the detectors (EPID and ion chamber). At each phantom thickness, both detectors were exposed to the same radiation conditions.

An exponential relationship between the measured dose/grayscale value and the thickness for 6 and 15 MV photons is shown in figures 3.12 (a) and (b). The relative transmission (T) was obtained from measurements of the average grayscale values as a quotient of the measurement of the thickness divided by the grayscale value measured without the attenuator on the beam. The relative transmission (T) can be written as follows:

$$T_{EPID} = \frac{G}{G_0} \text{.....3.1}$$

where G,the average grayscale value, is measured with the attenuator in the beam, and $G_0$is the grayscale value without attenuators. The corresponding dose values measured with the ion chamber are given by

$$T_C = \frac{D}{D_0} \text{.....3.2}$$

The transmission through the solid-water thickness situated at 100 cm SSD from the source with the flat panel positioned at 145 cm SSD. The transmission measured with the flat panel was compared to the transmission measured with the ion chamber. T decreases with the increase of the solid water thickness for both detectors. The EPID clearly responds differently to changing thicknesses of solid water when compared to the ion chamber.

Figure 3.12 (a) shows the results for 6 MV. The graph was fitted for the depth using an exponential fit. For the ion chamber, the transmission (T_C) equation was,

$$(T_C = 0.983\, e^{-0.048x} \text{... ... ... 3.3})$$

and the R^2 value for the fit was 0.999. For the EPID, the transmission (T_{EPID}) equation was,

$$(T_{EPID} = 0.963\, e^{-0.058x} \text{... ... ... 3.4})$$

and the R^2 value for the fit was 0.997. Figure 3.12(b) shows the results for 15 MV, the graph was fitted for depth using an exponential fit. The transmission (T_C) equation was,

$$(T_C = 0.997\, e^{-0.001x} \text{... ... ... 3.5})$$

and the R^2 value for the fit was 0.999 for the ion chamber. For the EPID, the transmission (T_{EPID}) equation was,

$$(T_{EPID} = 0.998\, e^{-0.051x} \ldots\ldots\ \ldots\ 3.6)$$

and the R^2 value for the fit was 0.999.

where x is required thickness of the absorber material.

Figure 3.12 (a) shows that the EPID responds 8.0% less for the 6 MV beam at a larger thickness than the ion chamber. The same behavior was observed in figure 3.12 (b) for 15 MV; however, the average percentage difference between the two detectors was 2.0% compare at 6 MV. The EPID is less sensitive to the low-energy photons (6 MV) and is more sensitive to the higher-energy photons (15 MV) with increasing thickness.

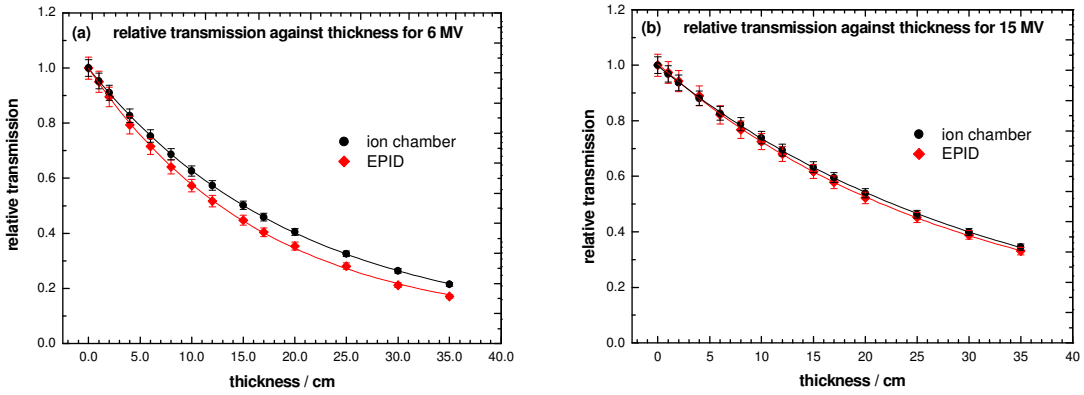

Figure 3.12. The relative transmission through a solid-water phantom measured with the a-Si EPID and compared to that measured with the ion chamber for (a) 6 MV and (b) 15 MV photon beams with the field sizes of 10 × 10 cm^2 for the EPID and ion chamber positioned at a source-to-detector distance (SDD) of 145 cm.

The T measured with the EPID for 6 MV was smaller than that measured with the ion chamber. The maximum deviation in transmission between the EPID and the ion chamber was 10%, occurring for a solid-water thickness of 30 cm. At 15 MV at the measured value of T with the EPID, the maximum deviation in transmission was found to be within 4.5% of that measured with the ion chamber of solid water thickness up to 30 cm.

The results showed that the radiation intensity can decrease when the patient is positioned at the isocenter of the beam, which has an impact on the amount of the dose that reaches the EPID. The results using the EPID measurements were within 10% of those measured with the ion chamber for the distance of the detector at 145 cm and the 10×10 cm^2 field size.

In general, for both beam qualities, increasing the solid water thickness both attenuates and hardens the beam. Because the EPID is more sensitive to lower energy photons, its response decreases more rapidly than the ion chamber as a function of attenuator thickness. Another possible explanation for this effect could be that low-energy scatter (secondary photons) is generated in the attenuating material, affecting the EPID response.

3.3.9 Electronic portal imaging devices as a dosimeter

3.3.9.1 Calibration of the a-Si EPID

Figures 3.13 (a) and (b), below, show the calibration curves of the a-Si EPID for 6 and 15 MV photons. The relationship between the EPID grayscale value on the beam central axis and the dose delivered to the EPID was evaluated based on the ion chamber measurements. The grayscale value of the EPID was proportional to the dose value measured using the ionization chamber for the 6-MV and 15 MV photons. The data were fitted with a linear function as follows:

$$D_P = C \times G_{EPID} + K \quad \text{..... (3.7)}$$

where D_P is the portal dose (this is the dose delivered to the point at the central axis of the EPID) and G_{EPID} is the EPID grayscale value at the same point. C and K are the proportionality constants. The different corresponding values for the constant C and K are shown in table 3.1. The fitted data show a linear relationship for a dose range up to approximately 90 cGy.

Figure 3.13 (a) shows the calibration curve for the 6 MV. The graph was fitted by making use of a linear function, the equation was,

$$(D_p = 3.26 \times 10^{-3} \times G_{EPID} + 2.47 \text{..... 3.8}).$$

The constant c and κ were 3.26×10^{-3} and 2.47, respectively. The correlation was good and the R^2 value was 0.999. Figure 3.13 (b) shows the calibration curve for the 15 MV. The graph was fitted using a linear function, the equation was,

$$(D_p = 2.26 \times 10^{-3} \times G_{EPID} + 3.33 \ldots\ldots\ldots \; 3.9).$$

The constant C and K were 2.26×10^{-3} and 3.33, respectively. The correlation was good and the R^2 value was 0.999.

Table 3.1. The variation of C and K constants in equation (1) and R^2 values for fits to the measureddata.

Energy/Dose rate	C	K	R^2 value
6 MV/300 MU/min	$3.26 \times 10^{-3} \pm 0.057 \times 10^{-3}$	2.47 ± 0.98	0.999
15 MV/500 MU/min	$2.26 \times 10^{-3} \pm 0.06 \times 10^{-3}$	3.33 ± 0.78	0.999

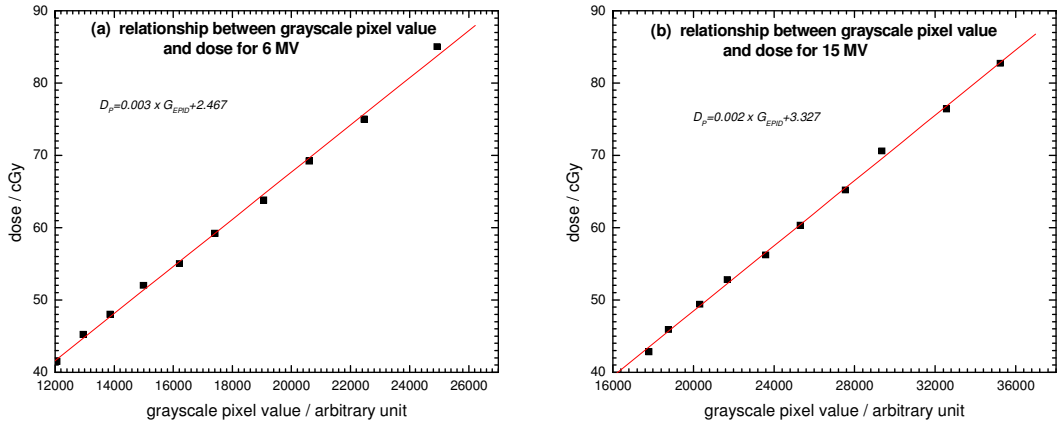

Figure 3.13.The variation in the EPID grayscale pixel values as a function of the dose delivered to the EPID for the (a) 6 and (b) 15 MV photons.

Figures 3.14 (a) to (d) show the crossplane relative beam profiles measured using the a-Si EPID and the 2D-Array Seven29 detector for 6 and 15 MV photons. These profiles were

for field sizes of 10 × 10 cm^2 (14.5 × 14.5 cm^2 projected on the detector plane) and 15 × 15 cm^2 (21.75 × 21.75 cm^2 projected on the detector plane) at an SDD of 145 cm. For the EPID profiles, the obtained 2D grayscale image responses were converted using the calibration procedureto obtian the 2D dose response. In each of the obtained graphs, the distance from the central axis was represented by the X axis; the Y axis showed the relative dose value (%) as a primary axis, and the dose-difference values displayed as a secondary Y axis.

Significant differences (maximum of 11%) were observed between the line profiles measured using EPID and 2D-Array for 15 × 15 cm^2 at 6 MV. The corresponding relative dose differences between EPID and 2D-Array were found to be less than 5% in the central part of the radiation field. However, at the edge of the field, including the penumbra region, several differences of more than 7% were observed.The results also showed maximum discrepencies around the edges of the fields and within a 10% local percentage difference (lpd). This was due to the sampling capabilities of the 2D-Array Seven29 detector (see chapter 3, section 3.6).

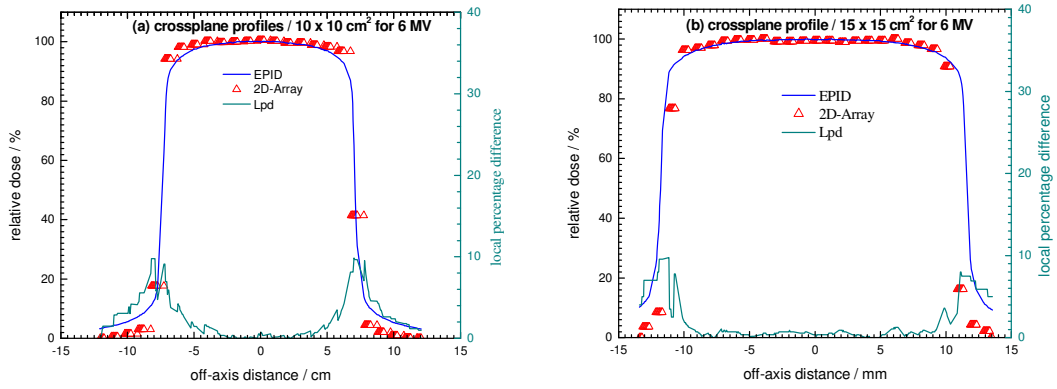

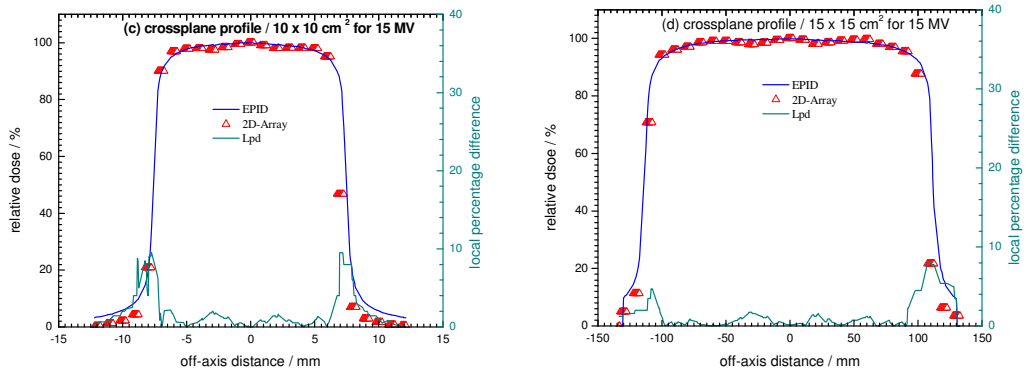

Figures 3.14 (a) to (d) show the crossplane beam profiles that were measured with the electronic portal imaging device (EPID) and the 2D-Array Seven29 at a 145-cm source-to-detector distance (SDD) for 10 × 10 cm^2 and 15 × 15 cm^2 field sizes. The crossponding gamma function values are also shown in each graph.

3.3.9.2 The evaluation of the fluence maps measured using EPID

Figures 3.15 (a) to (c) show the comparisons between the fluence maps measured using the 2D-Array detector and the a-Si EPID for three IMRT fluence fields: the left-posterior field, the anterior field and the right-posterior field. These figures the isodose overly for comparison of the fluence maps from the two detectors. The a-Si EPID measurements are represented by a solid line, and the 2D-array measurements are represented by dotted lines. A quantitative evaluation of the agreement between the datasets is represented by a line profile across the IMRT fields. Figure 3.16 shows typical crossplane profiles measured along the central axis of the field and the corresponding dose-difference values for comparisons between the a-Si EPID and the 2D-Array detector. The results of the EPID dose values generally agreed with those measured with the 2D-Array detector, especially in and around the central area. However, there were several discrepancies observed in the region around the edges. The percentages of the area in figure 3.18 in which the gamma index (3% DD and 3mm DTA) failed were 2.2, 2.5 and 1.9% for the left-posterior, anterior and right-posterior fields, respectively.

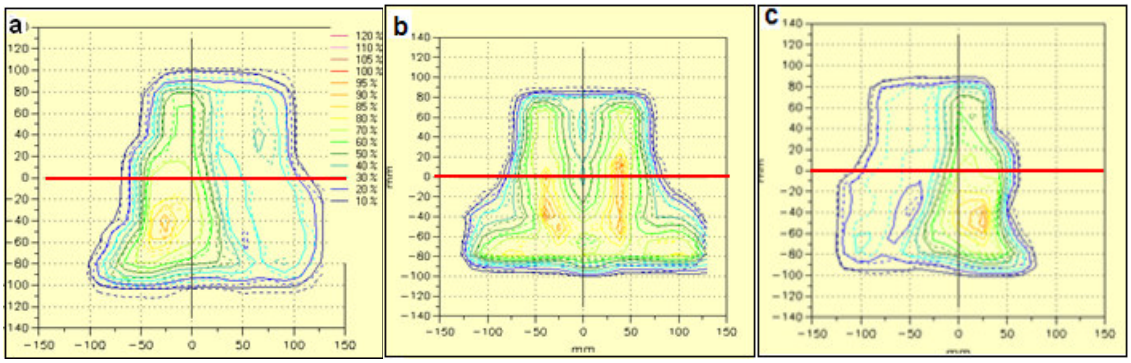

Figure 3.15. The isodose overlay comparing the 2D-Array Seven29 and the electronic portal imaging device (EPID) for three fluence map fields using the 3 mm and 3% criteria: a) the left-posterior field, b) the anterior field and c) the right-posterior field.

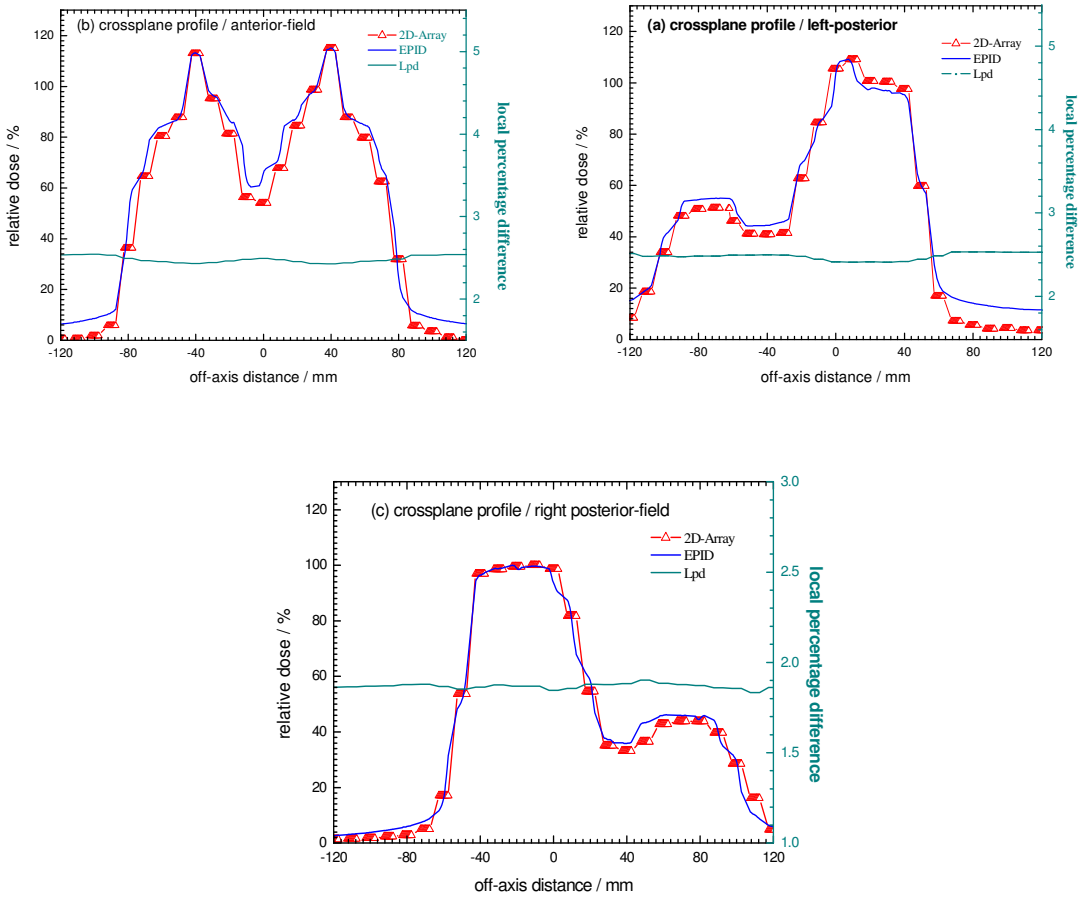

Figure 3.16. The crossplane relative dose profiles measured with an electronic portal imaging device (EPID) and the 2D-Array Seven29 detector system and the corresponding dose differences.

3.4 Conclusion

In this chapter, some dosimetric properties of the a-Si EPID detector and its potential applications for use for IMRT pre-treatment verification have been described.

The a-Si EPID proved to be convenient for portal dosimetry with the current acquisition software. Although the behavior of the a-Si EPID is not equal to the dose-to-water measurements, the a-Si EPID is an attractive dosimeter for radiotherapy treatment verification. The EPID grayscale values were reproducible; the maximum observed deviation in the grayscale value was 4% for the 15 MV photon beam. The a-Si EPID response to the applied MUs increased linearly up to 100 MUs, and then the response became stable for MUs higher than 200. Therefore, the detector should be calibrated in this range. The field-size dependence requires further investigation to understand the optimal calibration for accurate dosimetry. In addition, the discrepancy on the profiles' edges needs further investigation. The ghosting effect for the image acquisition time was negligible in the short time interval of 15 seconds. The EPID was also suitable for the measurements of the transmission dose.

Consequently, the verification of the measurements showed that the dosimetric calibration can be used for calculations of the dose from the EPID images. The relative planer dose difference between EPID and the 2D-Array was found to be within 5% in the central axis, with noticeable discrepancies at the edges of the field. The a-Si EPID dose distributions showed significant differences comparable to the 2D-Array ion chamber using the current criteria. Because of the large discrepancies observered between the EPID and 2D-Array detector doses, a proper calibration model for EPID is required before it can be used for the IMRT pre-treatment verification.

To summarize, a better understanding of the dosimetric properties of the a-Si EPID detector is necessary before it can be utilized for portal dosimetry. Recognizing the limitations of EPID and working around those limitations is necessary. The portal dosimetry system still has some challenges to resolve before accurate dosimetry can be performed using EPID. Future work requires improved calibration methods to be

incorporated, algorithms for dosimetric verification to be developed and some resolved dosimetric issues to be implemented in the commercially available system. Better software analysis tools would be highly beneficial to the routine use of this technique.

4. A comparative investigation of the IMRT fluence maps measured using Kodak EDR2 and 2D-Array Seven29 detection systems

4.1 Introduction

The use of the IMRT technique increased rapidly in radiation oncology centers. This increased use has accelerated the need for quantitative verification tools of intensity modulated dose distributions. Therefore, efficient dosimetric and geometric methods for performing patient-specific QA are required. Phantoms have been developed for individual patient dose verification, and several IMRT phantoms are commercially available for QA. Some of these phantoms use film alone, whereas others use film in combination with ionization chambers or diode detectors. Although these phantoms have been demonstrated to be useful in evaluating the IMRT plan qualitatively, their clinical use was found to be limited by the resources and time required for analysis.

Previously, ionization chamber measurements were the devices that were commonly used to commission IMRT TPS and to determine the absolute doses at specified points within the irradiation field. Here, manual methods have been used to compare calculated and measured doses; however, manual methods do not provide a comprehensive quantitative assessment of the accuracy of the calculation. Radiographic films have been widely used to measure the 2D dose distributions in IMRT. Kodak EDR2 film has been widely used to acquire a 2D dose distribution in a detector plane. X-Omatic Verification film (XV) was first used to measure the dose distributions. Later, EDR2 film was used extensively for patient-specific QA for IMRT. EDR2 film has proven to be a quality dosimeter that results in measurements with relative differences of between 2 - 5% of the calculated plans (Childress *et al.,* 2005). Another option for 2D dosimetry is a 2D-array system (Jursinic and Nelms 2003; Li *et al.,* 2009; Low *et al.,* 2011). Several studies have been conducted on the use of 2D-Array dosimetry systems for IMRT QA, and they have shown promise for use in IMRT fluence map verification. However, a comparison of Kodak's EDR2 film and a 2D-Array system for fluence map measurements needs to be performed to evaluate the accuracy of the dosimetry system.

The work reported in this chapter shows that the 2D-Array Seven29 systems can assist in accelerating the QA process. For the purposes of this study, IMRT head-and-neck plans derived from CMS XiO TPS were delivered to both EDR2 film and 2D-Array Seven29 dosimetry systems. The 2D-Array Seven29 ionization chamber and the EDR2 film relative isodose distribution were quantitatively compared to that of the isodose distribution generated by the CMS XiO IMRT plan. The efficiency, in terms of operator time, of the two 2D verification methods was also compared.

4.2 Materials and methods

4.2.1 IMRT delivery and fluence map generation

Inverse treatment planning was performed using CMS XiO version 4.3.1, IMRT TPS (CMS, XiO, St. Louis, MO, USA). Photon beams of 6 and 15 MV were used, and step-and-shoot IMRT was delivered with a Siemens ONCOR Impression Linac (Siemens Medical solutions, Concord, USA). The Linac was equipped with an OPIFOCUS MLC with 82 leaves. Three head-and-neck IMRT plans were generated using CMS XiO TPS. The IMRT fluence maps were generated using the head and neck IMRT treatment sites.

In the TPS for QA calculation purposes, the TPS allows the user to apply a patient-specific plan to a user-defined phantom, which can be created with either an image-based or a non-image-based dataset. A homogenous water-density phantom was created, and all of the IMRT QA plans were performed using isocentric techniques. To compare the calculated and measured fluences, a field-related approach was used in which all of the treatment parameters were the same as those in real patient plans except for the gantry angles, which were set to 0° for all beams. Each treatment field was reset to deliver the dose perpendicular to the phantom and an SSD of 95 cm. The weight of each beam was recalculated to deliver the dose at a depth of 5 cm in water while maintaining the same number of monitor units as those that were found in the original patient plan. After the IMRT plan was calculated, the saved plan file was transferred by using DICOM RT through the LANTIS network. Each treatment field was treated separately with a verification phantom.

4.2.2 Kodak EDR2 film measurements

Radiographic film dosimetry was performed using Kodak EDR2 Film (Kodak, Rochester, NY). EDR2 film has been used because of the dosimetric properties of the extended dose, the reduced energy dependence and the better linearity (Zhu *et al.,* 2003; Jacob *et al.,* 2008; Olch 2002).

Before the use of the film for the fluence map measurements, a calibration curve of the film must be established to relate the film optical density to the dose. The calibrations and fluence map measurements were performed with a single irradiation and developing session. Single sheets of Kodak EDR2 film with the Kodak X-Ray film processor Model 319 were used. The film processor was warmed up with six blank films. The processor QC checks were conducted on a regular basis, and the processor's chemicals were changed every three months. All of the working conditions that ensure the stable functioning of the developer were used. These include the developer, fixer, and dryer temperatures, which were set to 32.2 ± 0.5 ^{o}C.

The film characteristic curve was determined as follows: single sheets of EDR2 film were irradiated on the Linac with a 10×10 cm^2 field at an SSD of 100 cm and on the top of the solid-water phantom (GAMMEX rmi, Middleton, WI), with a thickness of 10 cm. The films were placed perpendicular to the beam central axis at a depth of 5 cm, and a photon energy of 6 MV was used. To establish the characteristic curve of the film, the calibration procedure delivered seven uniformly spaced dose levels of MUs to the film that ranged from 50 to 600 MUs (see figure 4.1). This was done to convert the film's optical density values to a dose and to characterize the film dosimetry system's reproducibility. All of the calibration curves and measurements were processed and scanned sequentially. All of the optical density values were converted to the net optical density by subtracting the optical density of non-irradiated films from the measured optical density.

The statistical errors of the film's characteristic curves were determined by consecutively repeating the irradiation procedure three times on the Linac. All of the films were processed at the same time. The optical density of each level and the background optical

density were recorded for each film and averaged over all of the films. The overall statistical error for the film's characteristic curves was calculated as follows: the average value and the standard deviation of the optical density at each level of three films were determined. The statistical errors were indicated by error bars in the calibration curve. The uncertainty varies from one department to another with different equipment and techniques.

For the fluence map measurements, the RMI solid-water phantom (GAMMEX rmi, Middleton, WI) and film were set up with the same geometry used to generate the QA plan at the Linac couch (see figure 4.2). The calculated plans from the TPS were downloaded to the Linac and used to irradiate the film with the same fields as those for the patient with all of the gantry angles set to zero. This was done by placing the films at the Linac couch with appropriate build-up and backscatter while maintaining the same SSD as calculated.

After the irradiation of the films, all of the films were developed in one session, and all of the film optical densities were measured by the VIDAR VXR-12 (Vidar Company, Herndon, VA) film scanner (see figure 4.3) and were analyzed with the *VeriSoft* V 2.11 software (PTW, Fiebureg, Germany). The film optical densities were converted to 2D dose distributions by using the calibration curve data. The film's scanner usually calibrated when a new scan is performed. The film's scanner was calibrated with a calibrated step wedge reference film that had 33 strips 0.73 cm wide and of certified optical density steps that ranged from 0.07 to 3.79. The calibration enables the conversion of the scanner numbers to optical density values.

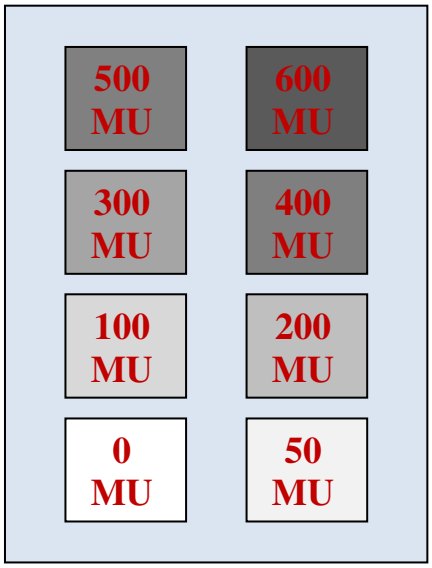

Figure 4.1 A schematic representation of the different monitor unit levels that were applied to the radiographic Kodak EDR2 film to establish a calibration curve.

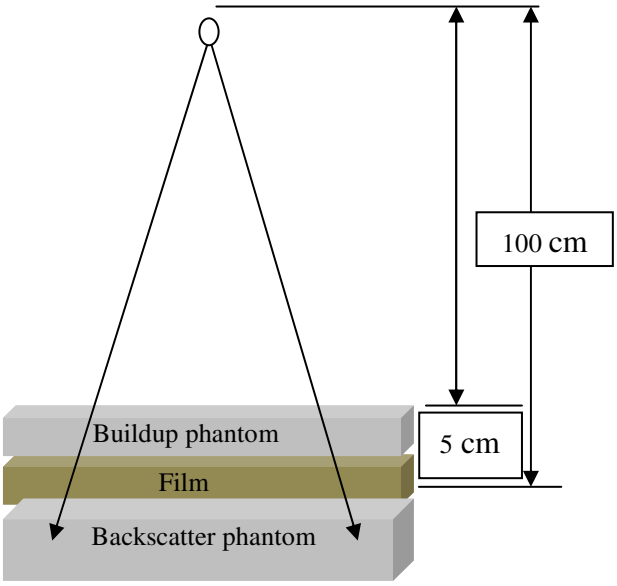

Figure 4.2.The set-up geometry for film dosimetry.

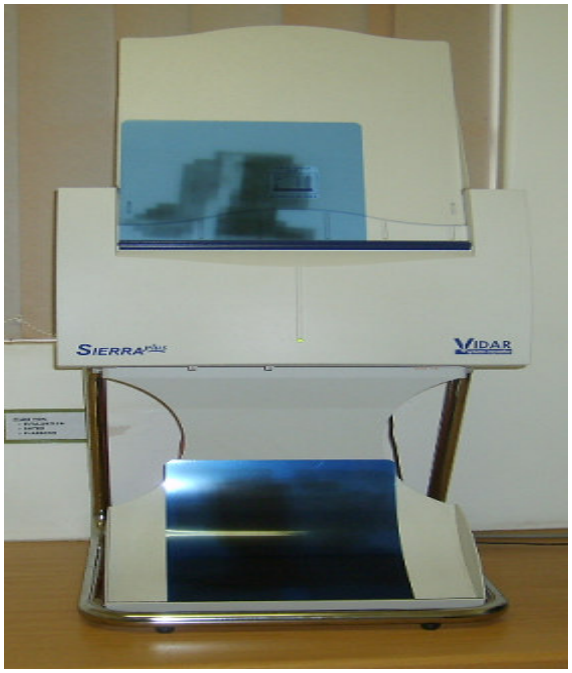

Figure 4.3.The VIDAR (VXR-12) film scanner.

4.2.3 2D-Array measurements

A 2D-Array Seven29 ionization chamber (PTW, Freiburg, Germany) detector system was used for IMRT QA verifications. In the experimental set-up for the fluence map measurements, the dosimetric parameters were set to be the same as they were in the TPS plans (see figure 4.4). The 2D-array was placed at the treatment table perpendicular to the radiation field; the center of the detector corresponded with the crosshair. A 5-cm build-up and a 5-cm backscatter material were added. By downloading the treatment fields to the Linac, each treatment field was delivered to the 2D-Array by using the same MUs and multi-leaf file as in the original plan. All of the measured treatment fields were saved under the same file for subsequent analysis. The 2D-Array detector was connected to the 2D-array interface and the PC, as shown in the structure system configuration (see figure 2.2). MatrixScan software was used to acquire the measured fluence maps. The software used to control the 2D-Array was called the MatrixScan and was used to acquire the data. The software determined the dose or the dose-rate data from the irradiation of the 2D-Array by the Linac. It used 3D graphics to display the data and transfer the acquired data to the *VeriSoft* software for analysis.

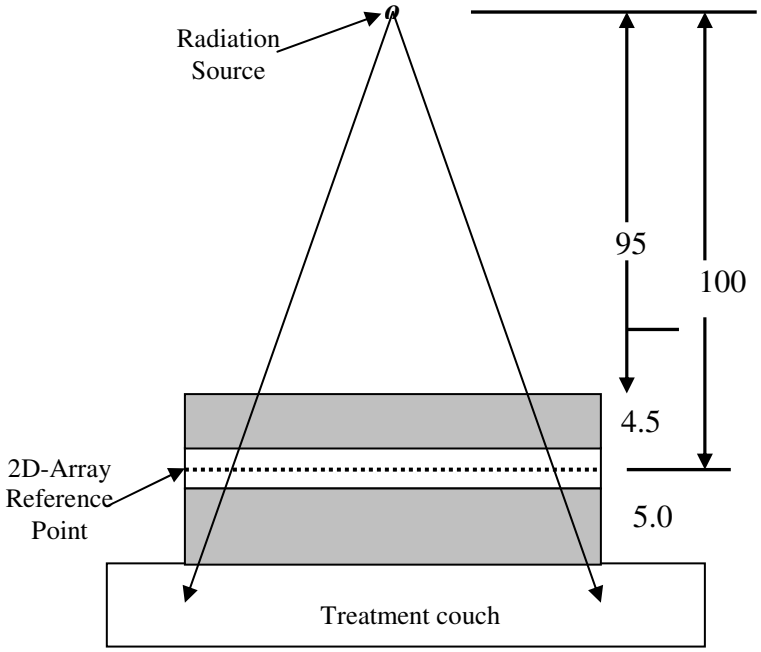

Figure 4.4.The placement geometry of the 2D-Array Seven29 ionization chamber.

4.2.4 IMRT dose matrix registration and analysis

VeriSoft has been used for dose matrix registration and analysis (VeriSoft operator's manual). The software provides a crosshair tool that allows the center of the calculated and measured dose matrix to be set. There are also different tools that can be used for dose matrix rotation, setting the crosshair zero position, scaling, the selection of a region of interest, and the calibration and normalization of each image. These tools are used to linearly scale and align the measured dose matrix to the TPS-calculated dose matrix. The software allows for an automated display and a comparison of the measured and calculated dose distributions. It consists of 3 modules: the profile presentation and/or comparison, the 2D-isodose presentation and/or comparison and the 3D-isodose presentation and/or comparison. For the dose matrix comparisons, the software requires that the matrices have the same resolution. The software allows for the resampling of the image with the highest resolution and sets its resolution to match that of the lower resolution image. To compare two matrices, the user has to change all of the images' pixel units to the same values. The matrices can be overlaid, the image centers can be

aligned, and the remaining non-image-based region of the re-sampled image can be filled with zero values. The measured images using the Kodak EDR2 film dosimetry system can then be calibrated using the established calibration curves. The calculated and measured dose distributions are usually compared by normalizing them to a common point and assuming that the doses are equal at that point. The software can also analyze the matrices via isodose colorwash (or grayscale) subtraction. All three methods of evaluation can be viewed simultaneously on-screen to aid in the overall image analysis.

4.2.5 Gamma evaluation and acceptance criteria

To compare the dose matrices, the gamma evaluation method (Low *et al.,* 1998) has been used. This method is a theoretically based method that utilizes user-defined factors, the so-called gamma index. The index factor is based on user-acceptable percentage dose differences and distance-to-agreement to obtain a schematic of areas that pass or fail to meet the user-defined criteria. The VeriSoft software was chosen to implement the level based on the assessment criteria of Depuydt *et al*. (2002) for quantitative evaluation method; Gamma evaluation becomes a very useful tool in analyzing co-registered dose distributions containing both high- and low-dose regions along with steep dose gradient areas. This aspect makes this approach one of the tools of choice for the analysis of IMRT fields. The gamma index factors that are utilized in evaluating the gamma evaluation function in the software were ± 3%/3 mm of the dose difference and the distance-to-agreement values, respectively.

4.2.6 Testing the pass-rate criteria

An IMRT plan will be satisfactory even if as little as 90% of the tested points comply with the gamma criterion (Low *et al.,* 1998). When comparing the dose distributions using the gamma evolution criteria, the reasoning for using a 3%/3 mm cut-off and the criterion that a certain percentage must pass a level of 90% is based on what is technically achievable and not what would have a clinical impact. In this test, the aim is to see if a plan that fails the fluence QA with the current criteria and 90% would it be clinically unacceptable.

A head-and-neck IMRT plan generated using CMS XiO TPS was used. The plan was chosen from the clinically approved and treated IMRT plans. The plan has multiple target volumes and multiple organs at risk that are distributed throughout the treatment volume. This plan was considered to be an error-free IMRT plan and was used for the IMRT QA dose plans and patient doses. Another IMRT plan was created by introducing errors into the chosen plan. The errors were introduced into the plan to create dose differences in the IMRT fluence maps. Artificial changes of more than 10% of the fluence area in the field were made by a value of +5% in areas of a high dose gradient and dose levels in the field to simulate a few miscalibrated leaves; these changes were followed by a recalculation of the IMRT plan. For fluence QA purposes, IMRT plans were recalculated in a homogenous water-density phantom. The error-free plan and the error-induced plan were compared in terms of fluence maps and with the dose-volume histograms (DVHs). Finally, the suitability of both IMRT plans in terms of their dose matrices and patient anatomy dose differences were assessed; the clinicians in our department assisted with the assessments.

4.3 Results and discussion

The results of the measurements that were conducted for this study are presented in the following sections. In addition, results based on the time efficiency will be presented following the experimental data.

4.3.1 Kodak EDR2 film measurements

A calibration curve for EDR2 film is shown in figure 4.5. The response of the film to the dose is not strictly linear. To accommodate this variation in the response, all of the IMRT films were converted with optical density dose functions prior to the generation of the isodose plots. The film becomes saturated following direct exposure to approximately 700 cGy. The calibration curve was confirmed by repeating the experiment three times. The average total optical density uncertainty for all of the levels was 3%. The increased error is mainly due to the processor effects. The calibration curve data will be used as input for converting the optical densities to doses for fluence map comparisons.

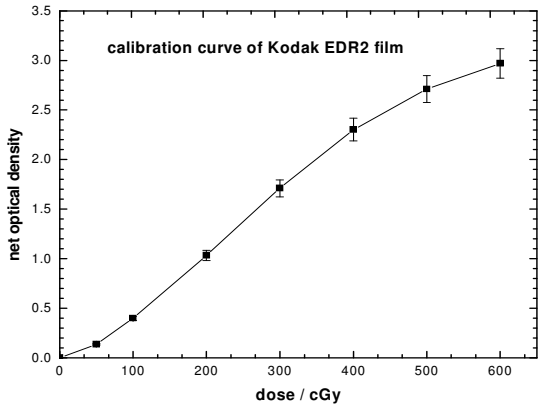

Figure 4.5.The calibration curve of the EDR2 film. The curve shows the approximately linear relative dose response of the EDR2 film. The film becomes saturated with a direct exposure to approximately 700 cGy.

Figures4.6, 4.7 and 4.8 show comparisons between the film and TPS dose distributions and the gamma evaluation for the first IMRT plan containing three fields: the anterior field, the left-posterior field and the right-posterior field. These results enabled the evaluation of the degree of agreement between the measured and calculated dose distributions in the regions of the dose gradient. Level-based assessment criteria were used for dose distribution comparisons. The criteria would only allow a 1^{st} pass; 1^{st}pass and 2^{nd} pass only; or 1^{st}, 2^{nd} and 3^{rd} pass. Details of 1^{st}, 2^{nd} and 3^{rd} pass definitions are provided by Depuydt *et al.* (2002). By using level-based assessment, the acceptance criteria were user definable with user inputs for distance-to-agreement (in mm) and percentage dose difference. The dose range to which the distance-to-agreement and percentage difference matching criteria are applied vary (i.e., the user can elect to use a higher percentage tolerance below a nominated threshold of the total dose). The currently used version of the VeriSoft gamma evaluation does not report any numerical solutions of the gamma function; instead, a pass/fail criterion was implemented.

Figures 4.6 (a), (c) and (e) show the isodose overlay for the three IMRT fields. The results present the concurrence of the two datasets. This concurrence was quantitatively confirmed by the gamma map plots and vertical and horizontal line scans through the

isocenter (see figures 4.9 (a) to (f)). Figures 4.6 (b), (d) and (f) illustrate the dose-difference gamma function pass/fail criteria. The results are illustrated in the green area, which fulfilled the criterion for the entire irradiated field. Regions in red represent areas where the gamma evaluation criteria were not fulfilled. The results for the first and second IMRT fields showed discrepancies in which there were areas that did not meet the criteria due to the film dosimetry. Figures 4.7 and 4.8 also show comparisons between the measured and calculated datasets for the second and third IMRT plans.

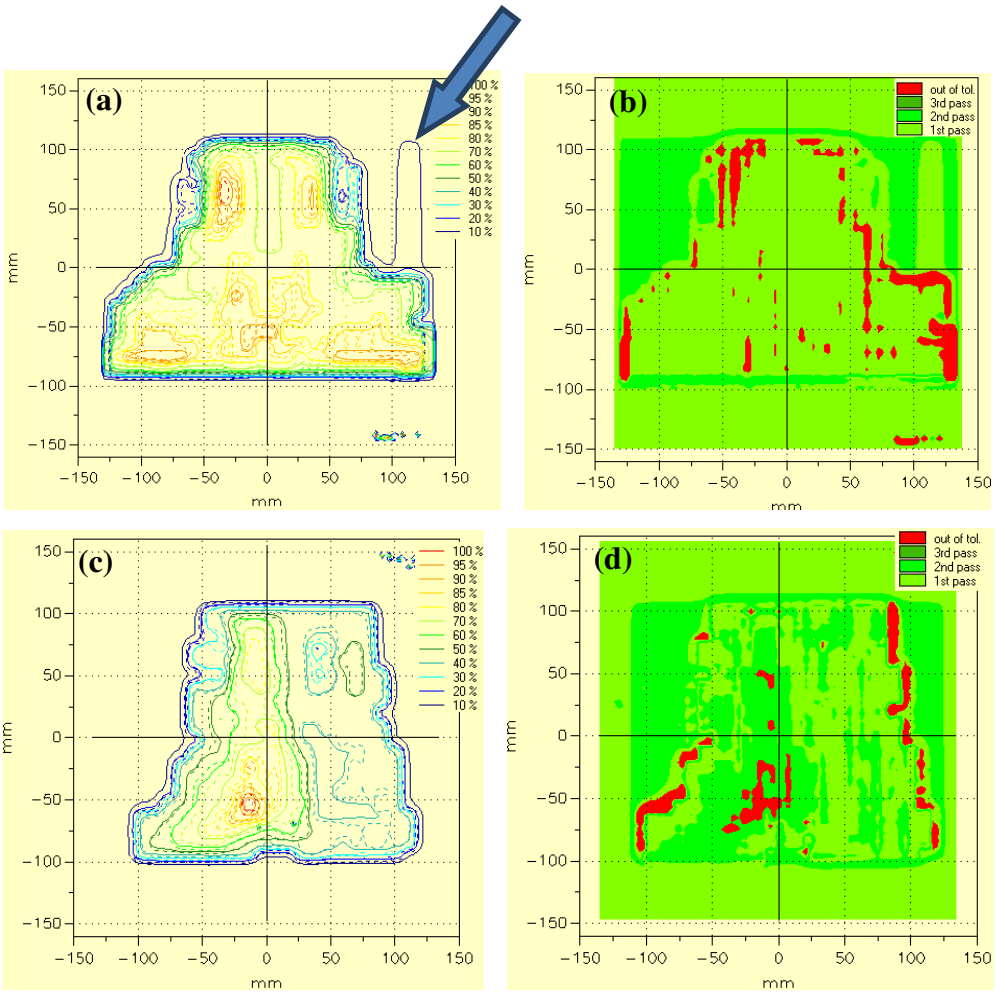

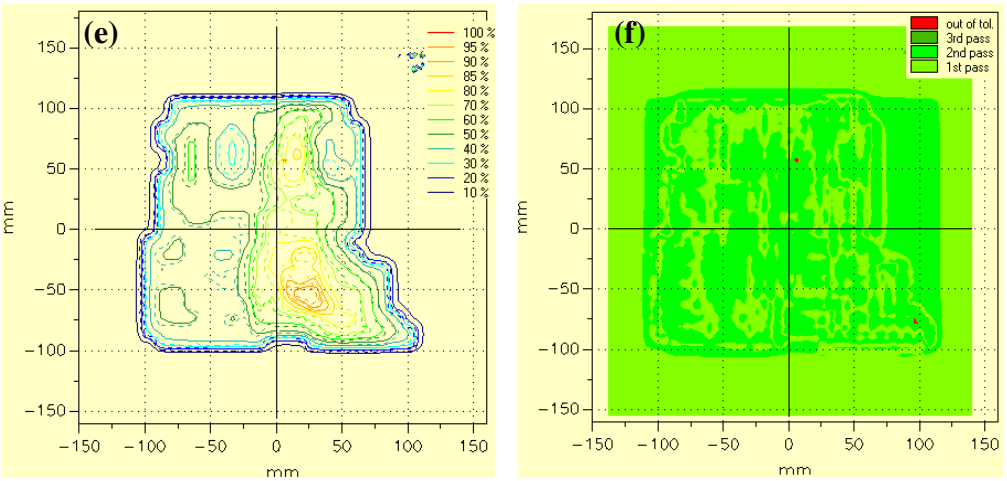

Figure 4.6.(a), (c) and (e) show IMRT isodose overlay comparisons (solid line: TPS; dotted lines: film); (b), (d) and (f) show gamma function pass/fail criteria. The green color represents areas for which the gamma index criterion is met, and the red color represents the areas for which the gamma index criterion is not fulfilled. These results are for the first IMRT plan. The areas indicated by the arrows on the top of the figure represent systematic errors.

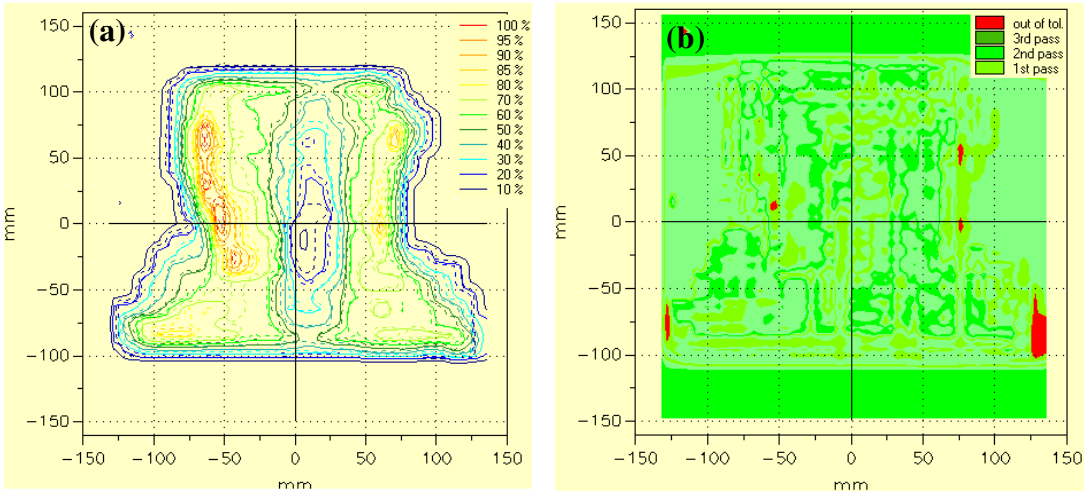

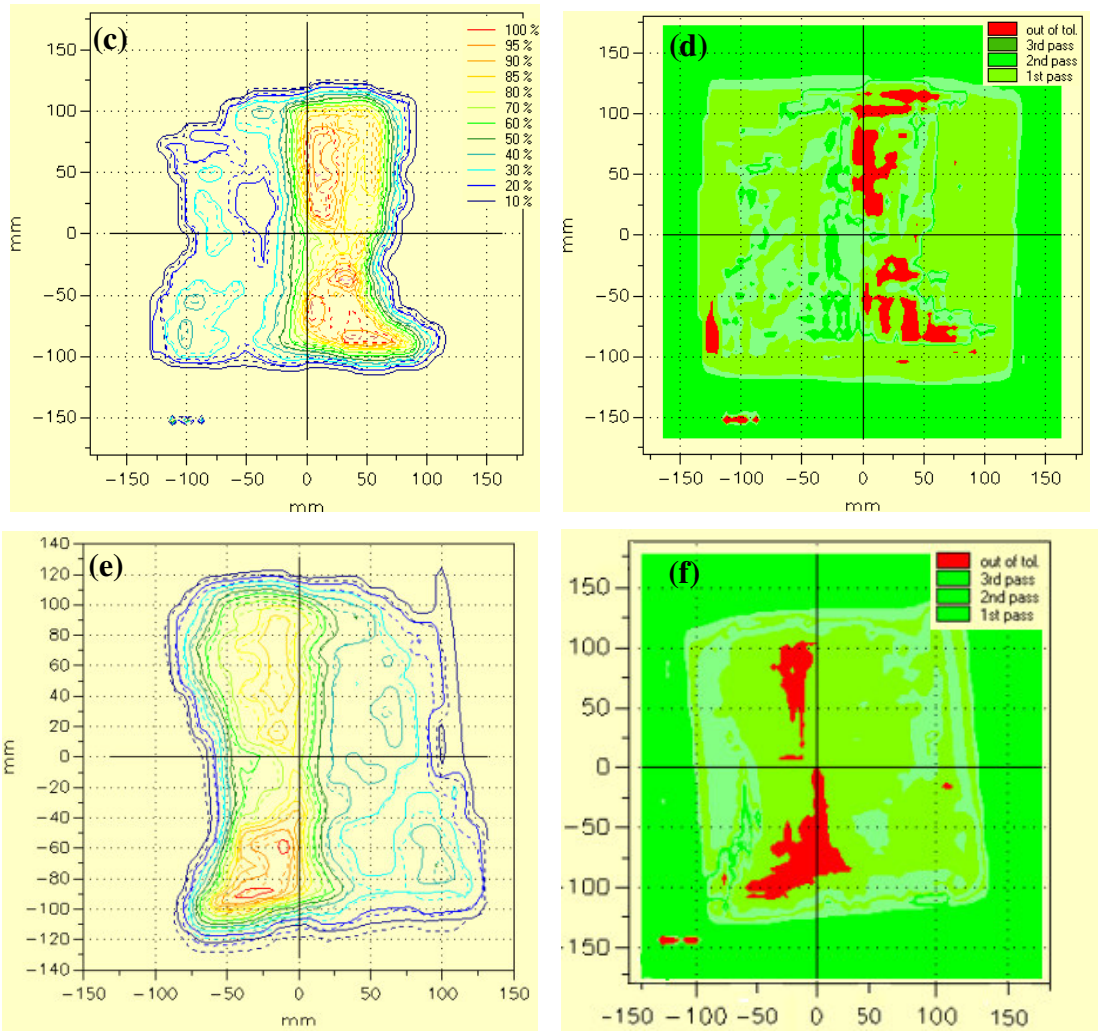

Figure 4.7.(a), (c) and (e) show the IMRT isodose overlay comparisons (solid line: TPS; dotted lines: film); (b), (d) and (f) show gamma function pass/fail criteria. The green color represents areas for which the gamma index criterion is met, and the red color represents the areas for which the gamma index criterion is not fulfilled**.** These results are for the second IMRT plan.

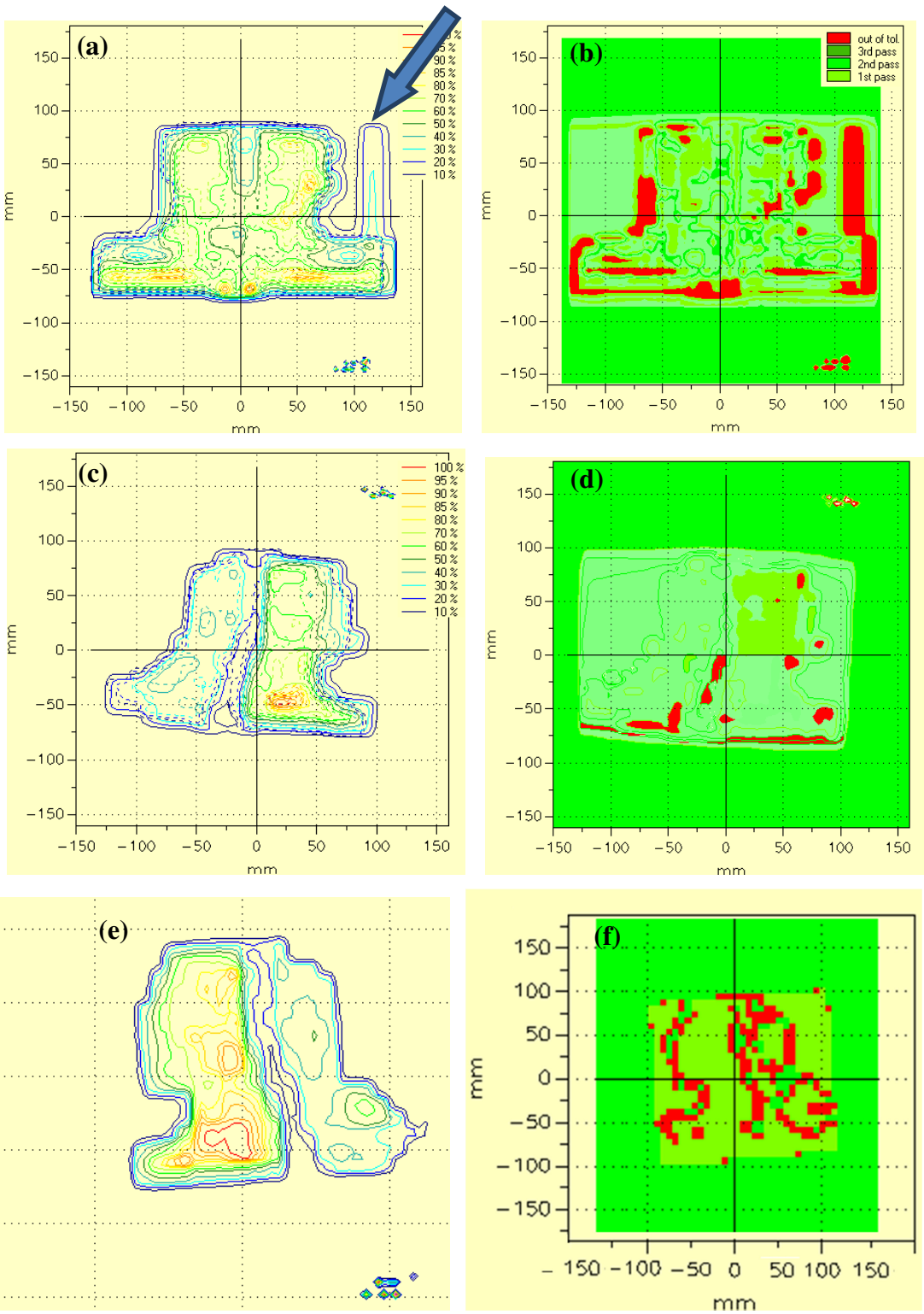

Figure 4.8.(a), (c) and (e) show IMRT isodose overlay comparisons (solid line: TPS; dotted lines: film); (b), (d) and (f) show gamma function pass/fail criteria. The green color represents areas for which the gamma index criterion is met, and the red color

represents areas for which the gamma index criterion is not fulfilled**.** These results are for the third IMRT plan. Areas indicated by the arrows on the top of the figure represent systematic errors.

Figures 4.6 (a), 4.8 (a) and (b) show noticeable discrepancies between the measured and calculated dose distributions. These discrepancies were indicated by a small peak in the fluence maps. This is an error in the calculation of the IMRT fluence maps within the TPS. This is an example of how routine QA picked up a systematic error that could be rectified. This behavior was also observed in figures 4.10 (a), 4.12 (a) and (b) and the dose profiles (4.13 (a)). Examples of these errors were also observed in the calculated segments in IMRT field in the TPS, as shown in figures 4.9. (a) and (b).

The error occurred because CMS XiO TPS required the MLC jaws to close (MLCs from both banks touching each other) in the middle of the current beamlet. For very large fields, only this position can be beyond the over travel limit of one of the MLC leaf banks. Therefore, instead of closing, the MLC leaf, a small gap appears. This can be remedied by either closing the leaves at another position closer to the center or by bringing in the jaws from the side. Once this problem was discovered through the QA processes, a computer program was developed to fix this problem.

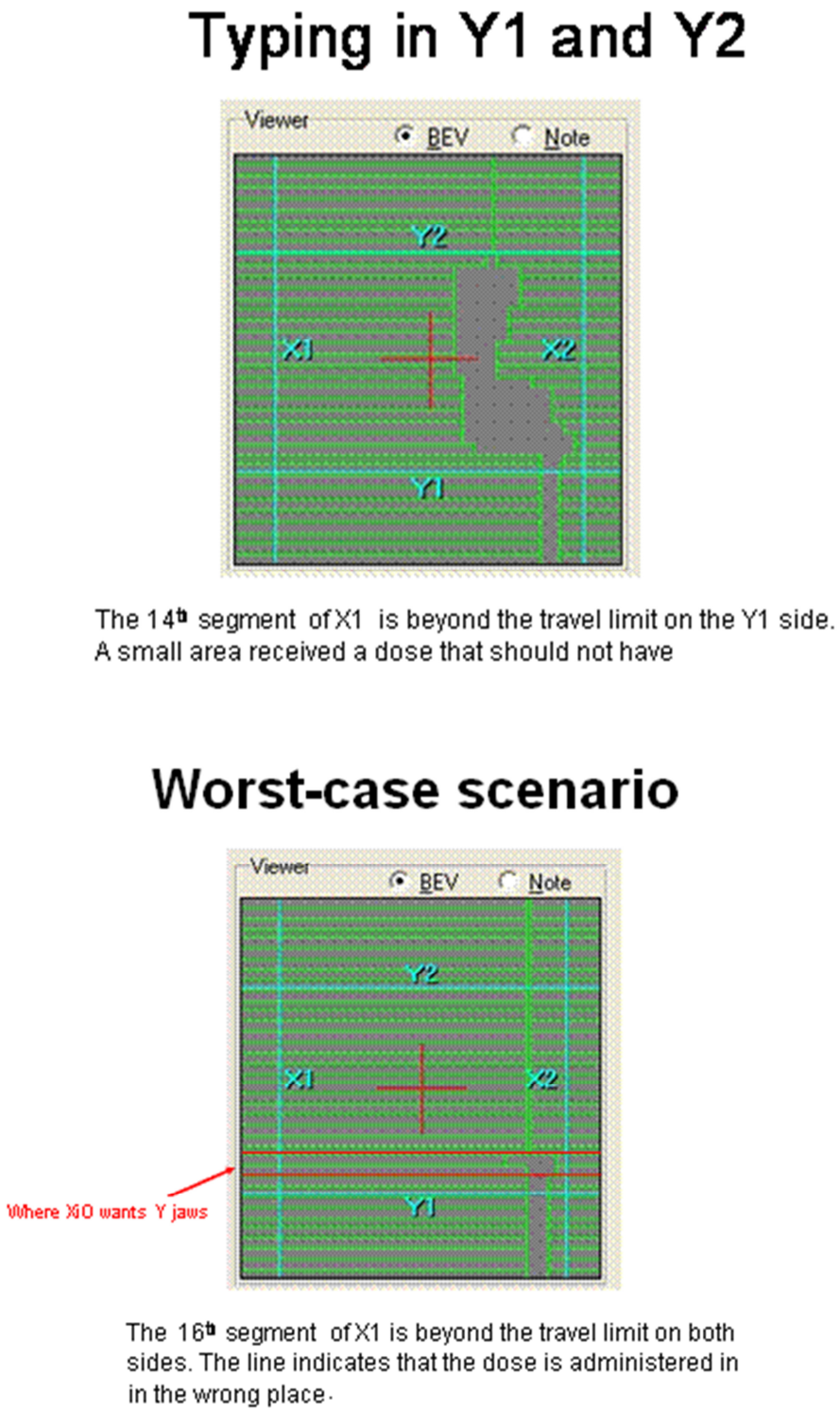

Figure 4.9. An example of two cases for the systematic errors that occur in CMS XiO TPS.

Figures 4.10 (a) to (f) show profiles that were extracted from the measured intensity maps that used film and from the calculated intensity maps that used TPS. The comparison was done by tracing the dose values along a straight scan line, as indicated in the 2D plot, in the X and Y directions for three IMT fields in the first plan. The normalization point was the same for the film and the TPS. The graphs below clearly demonstrate that the measured and the calculated data fit each other well. The graphs also show that the correspondence is within the tolerance range for film dosimetry with noticeable discrepancies that were also observed at the field edges with high gradients. Figures 4.10 (a), (c) and (e) show maximum dose differences of 12.0% between the film and TPS in the X-direction, whereas the average dose differences were 4.0 ± 0.9%, 3.4 ± 0.9% and 2.5 ± 0.8% for field1, field2 and field3, respectively. In figures 4.10 (b), (d) and (f), the maximum dose difference between the film and the TPS in the Y-direction is 10.0%, whereas the average dose differences were 3.4 ± 1.4%, 2.7 ± 1.2% and 2.6 ± 0.8% for field1, field2 and field3, respectively. These deviations were caused by the processor effect in film dosimetry and by the overreaction of the radiographic EDR2 films to low-energy photons (Yeo *et al.,* 2004; Wiezorek *et al.,* 2005), which is expected in higher mass energy absorption coefficients for energies up to 150 KeV. Similar results have been previously published (Van Esch *et al.,* 2002).

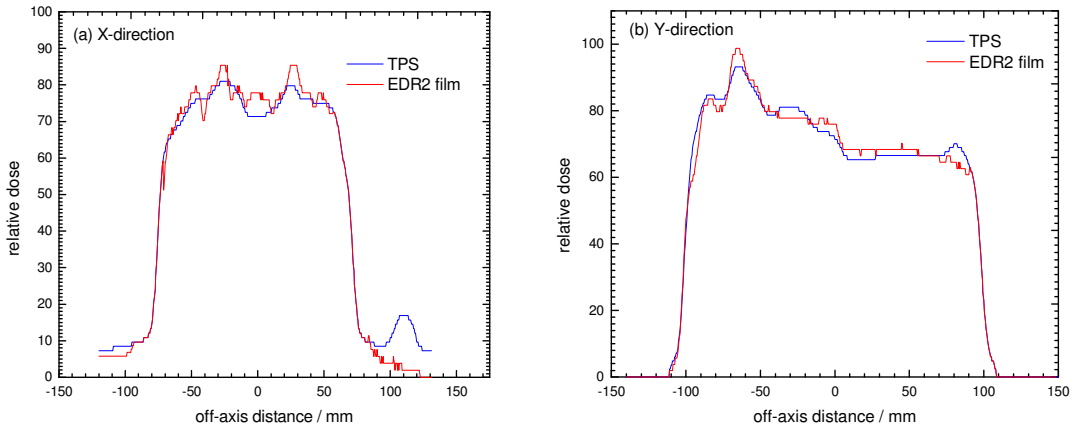

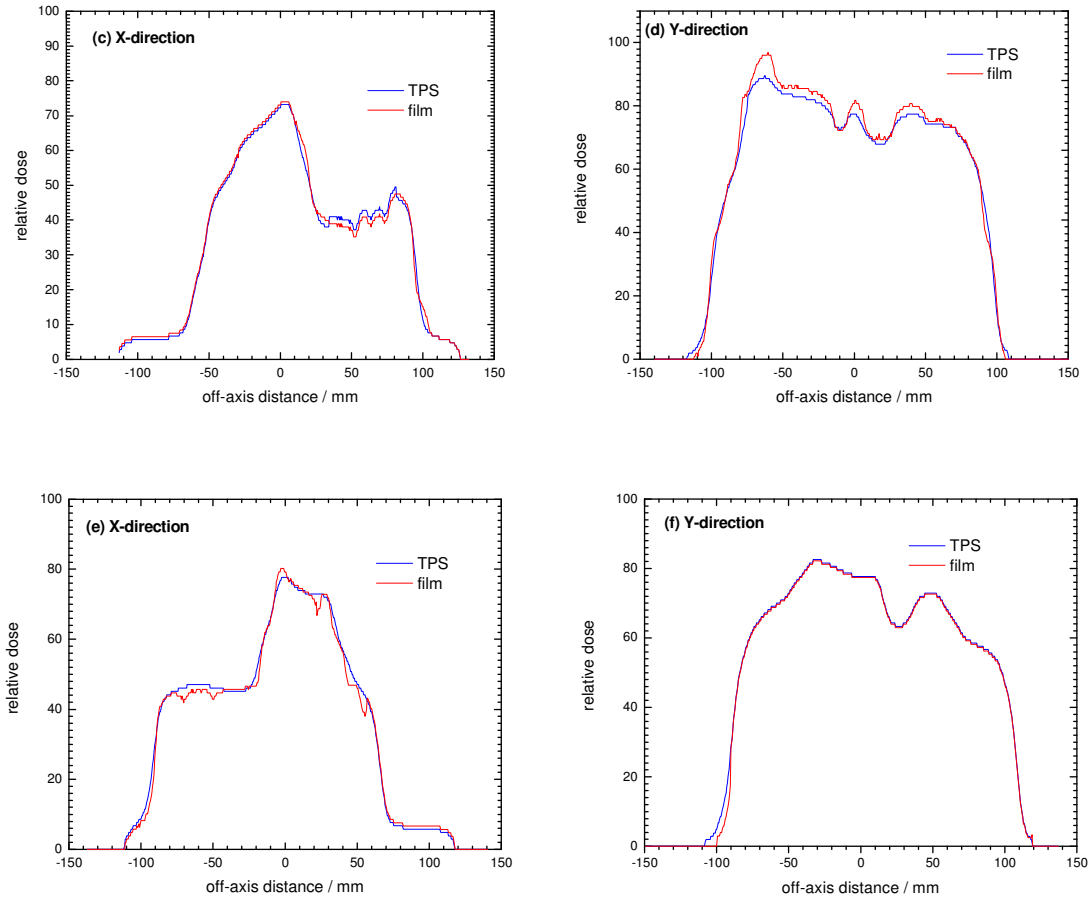

Figure 4.10. Comparisons of the plots of the measured (red line) and calculated (blue line) doses of the three IMRT dose profiles normalized to the maximum dose taken by the Kodak EDR2 film.

4.3.2 2D-Array measurements

Figures 4.11, 4.12 and 4.13 display comparisons between the measured dose distributions from the 2D-Array and the calculated dose distributions from the TPS. These figures depict the isodose overlay, which shows the agreement of the measured and calculated dose distributions. These agreements were quantitatively confirmed by the gamma evaluation criteria, in which the green indicates the area or point that met the criteria, whereas the red indicates the points at which the criteria were not reached. As mentioned previously, the criteria were implemented in the software set for a DTA of 3 mm and a dose difference of 3%. This dose difference can be tolerated up to 10%, especially in

treatment cases of the head and neck in which highly modulated beams are used and are subject to relatively higher discrepancies.

The first IMRT plan is shown in figure 4.11. In this figure, the gamma evaluation plot of the dose distributions shows an agreement for most of the points among the datasets for the three fields with the exception of small deviations shown at the edges of the field, which were confirmed with the plotted profiles along the field (see figure 4.15). The disagreements resulted from the high dose gradient. The results for the second and third IMRT plans showed more points that failed to meet the criteria in comparison to the first plan. These results are illustrated in figures 4.12 and 4.13.

Overall, the evaluation criteria for head-and-neck IMRT plans were set to investigate the possible dependence of the gamma agreement on the measurement technique. The acceptance criteria were not met, and those areas were observed at the edges of the fields and at high dose gradient areas; these deviations were due to the measuring device, which had a higher relative error level.

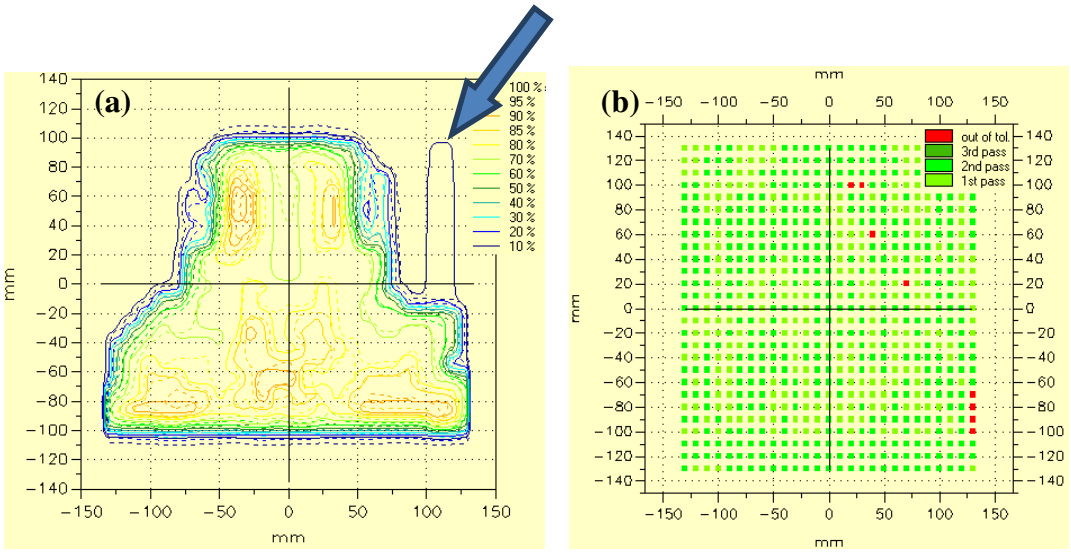

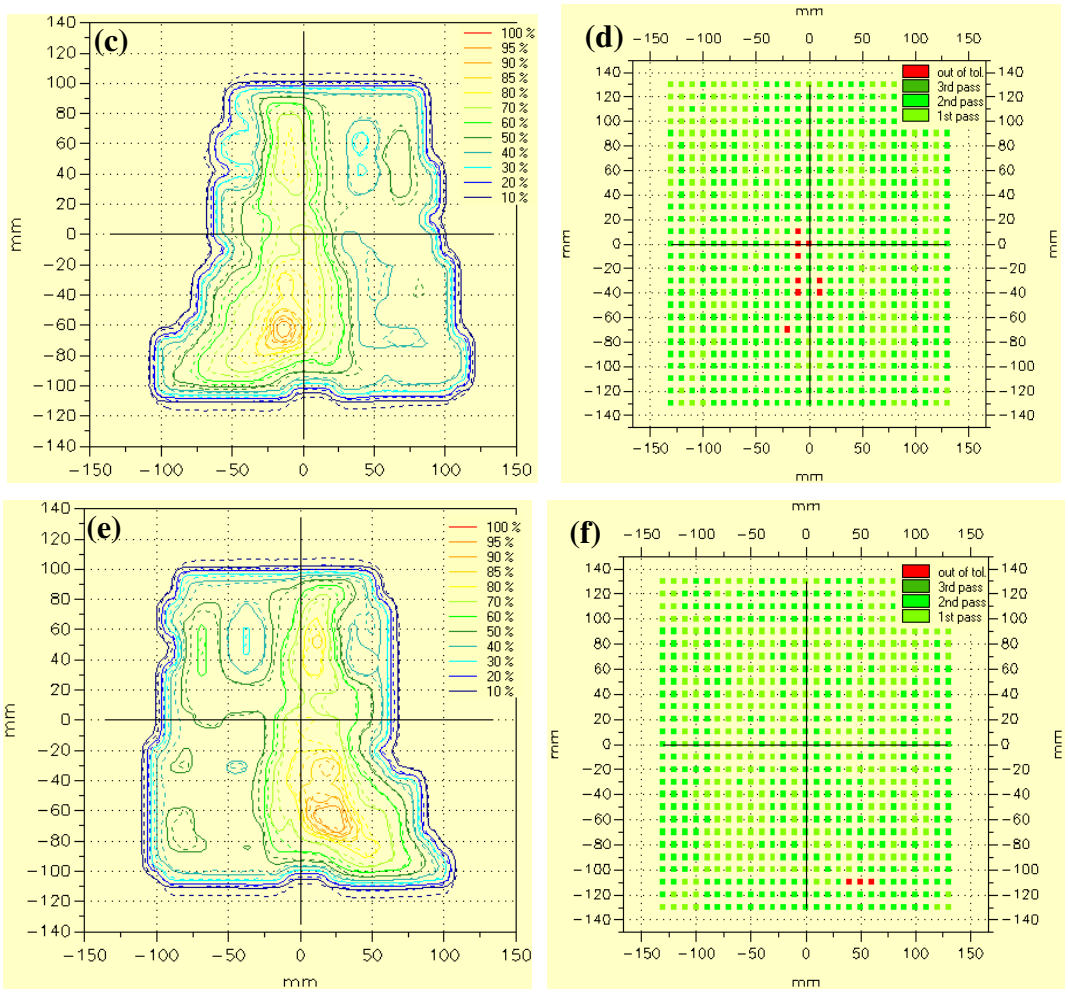

Figure 4.11.(a), (c) and (e) show IMRT isodose overlay comparisons (solid line: TPS; dotted lines: 2D-Array); (b), (d) and (f) show the gamma function pass/fail criteria. The green color represents areas where the gamma index criterion is met, and the red color represents areas where the gamma index criterion is not fulfilled**.** These results are derived from the first IMRT plan. Areas indicated by the arrows on the top of the figure represent systematic errors.

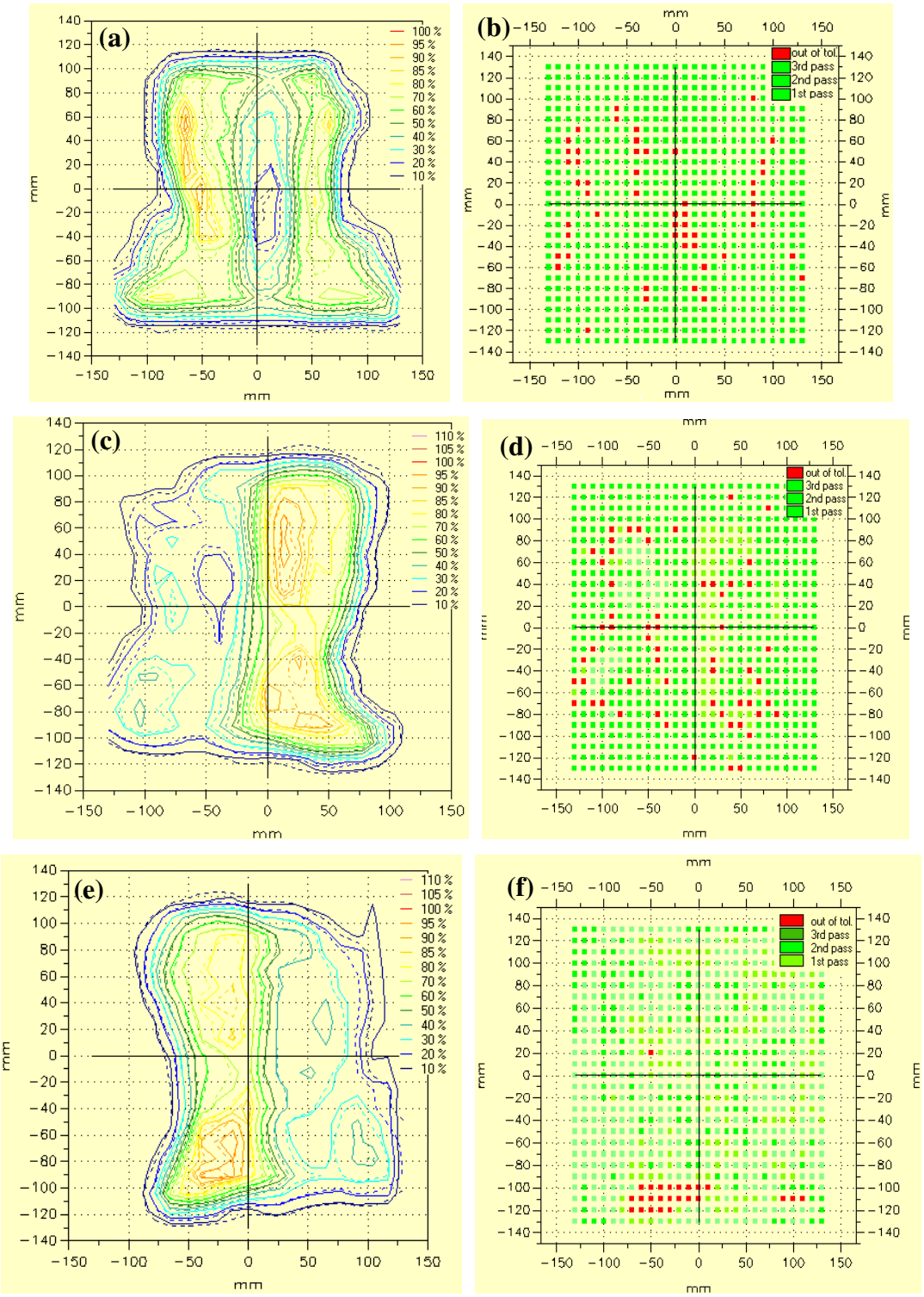

Figure 4.12.(a), (c) and (e) show IMRT isodose overlay comparisons (solid line: TPS; dotted lines: 2D-Array); (b), (d) and (f) show the gamma function pass/fail criteria. The green color represents areas where the gamma index criterion is met, and the red color

indicates areas where the gamma index criterion is not fulfilled. These results are for the second IMRT plan.

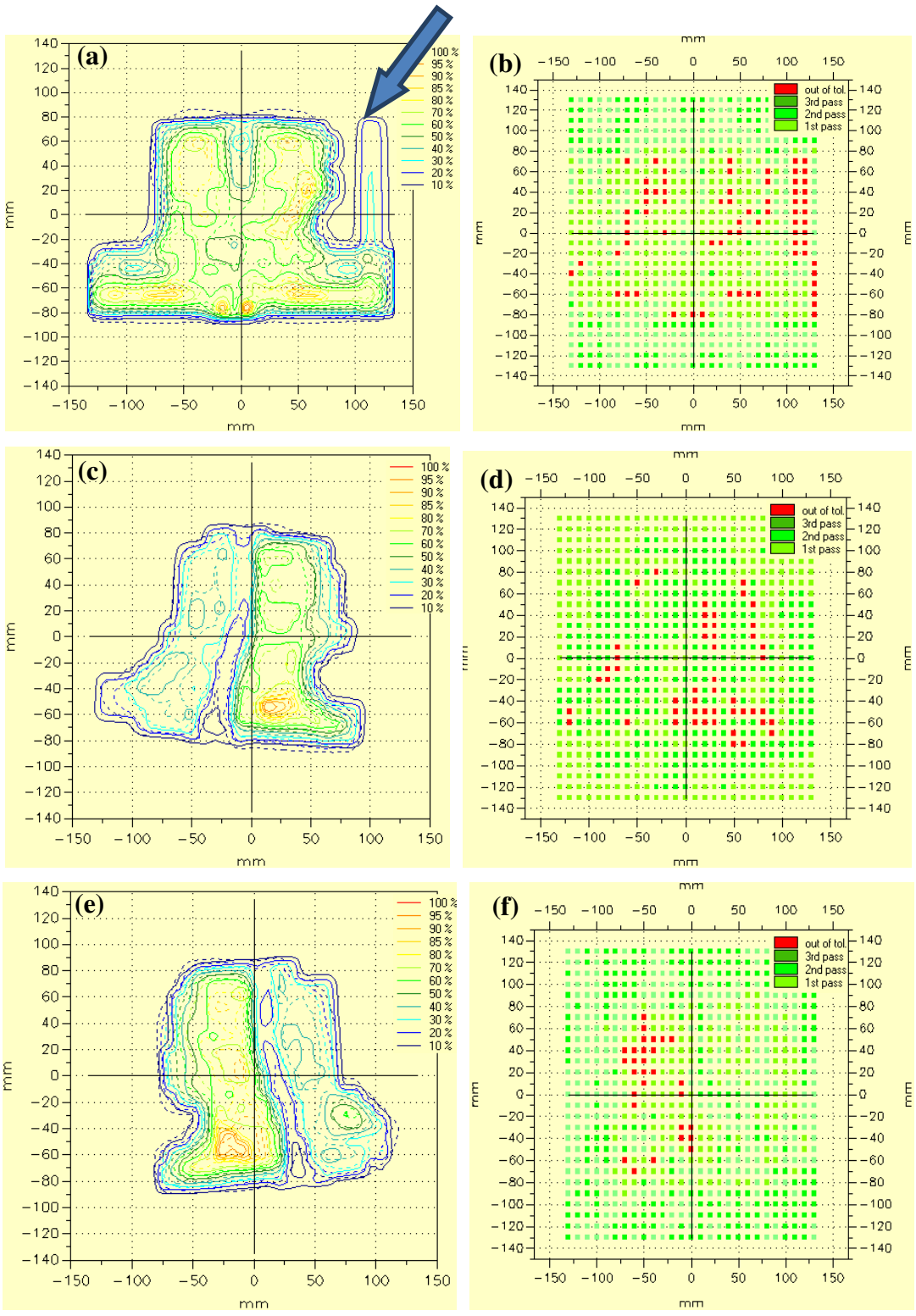

Figure 4.13.(a), (c) and (e) show IMRT isodose overlay comparisons (solid line: TPS; dotted lines: 2D-Array); (b), (d) and (f) show gamma function pass/fail criteria. The green color represents areas where the gamma index criterion is met, and the red color represents areas where the gamma index criterion is not fulfilled. These results were based on the third IMRT plan. Areas indicated by the arrows at the top of the figure represent systematic errors.

In figure 4.14, the calculated beam profiles are shown by a blue line, whereas while the measured profiles from the 2D-Array are shown by red points. Although the results showed some discrepancy at the edges of the fields for some of the beam profiles, which was likely in response to the high dose gradients, a close correspondence between the beam profiles for the calculated and measured data was observed. Figures 4.14 (a), (c) and (e) show the maximum dose difference of 8% between the film and TPS in the X-direction, whereas the average dose differences were 3.2 ± 0.9%, 3.4 ± 0.8% and 2.8 ± 0.8% for field1, field2 and field3, respectively. In figures 4.14 (b), (d) and (f), the maximum dose differences between the film and TPS in the Y-direction was 8%, whereas the average dose differences were 3.1 ± 1.4%, 4.3 ± 1.2% and 3.0 ± 0.9% for field1, field2 and field3, respectively. Agreement between the calculated and measured data is shown for the line profiles along the X-axis and Y-axis despite the fact that the inverse-planning demands were complex and required strongly modulated IMRT fields.

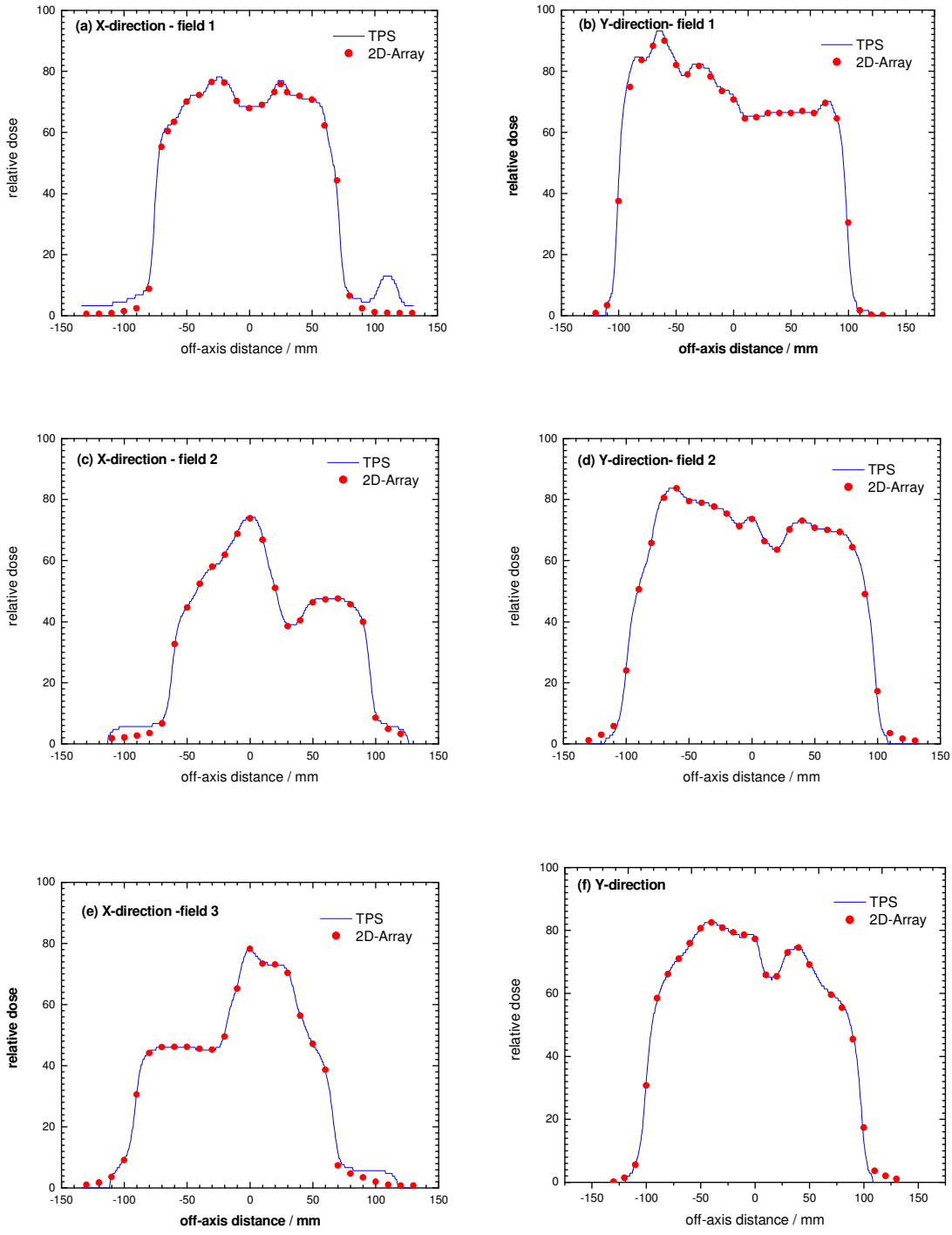

Figure 4.14. A comparison of the measured (red points) and calculated (blue line) results of the three IMRT dose profiles normalized to the maximum dose determined by the 2D-Array Seven29 detector.

4.3.3 Testing the pass-rate criteria

Figures 4.15 and 4.16 show comparisons among the three measured and calculated IMRT plans. Figure 4.15 depicts an error-free IMRT plan, whereas figure 4.16 depicts an IMRT plan with introduced errors. Figure 4.15 shows that most of the points in the IMRT plan met the criteria, and only a few points failed for the three fields: the anterior, the left-posterior and the right-posterior fields. In figure 4.6, the anterior and the left-posterior field passed by a few points; the points that failed to meet the criteria are in red. The right-posterior field exhibits the most of the points in the field that did not meet the evaluation criteria. These points fell within areas of a high dose gradient. The results showed that the IMRT plan failed to meet the criteria of 3%/3mm for the dose difference and distance-to-agreement.

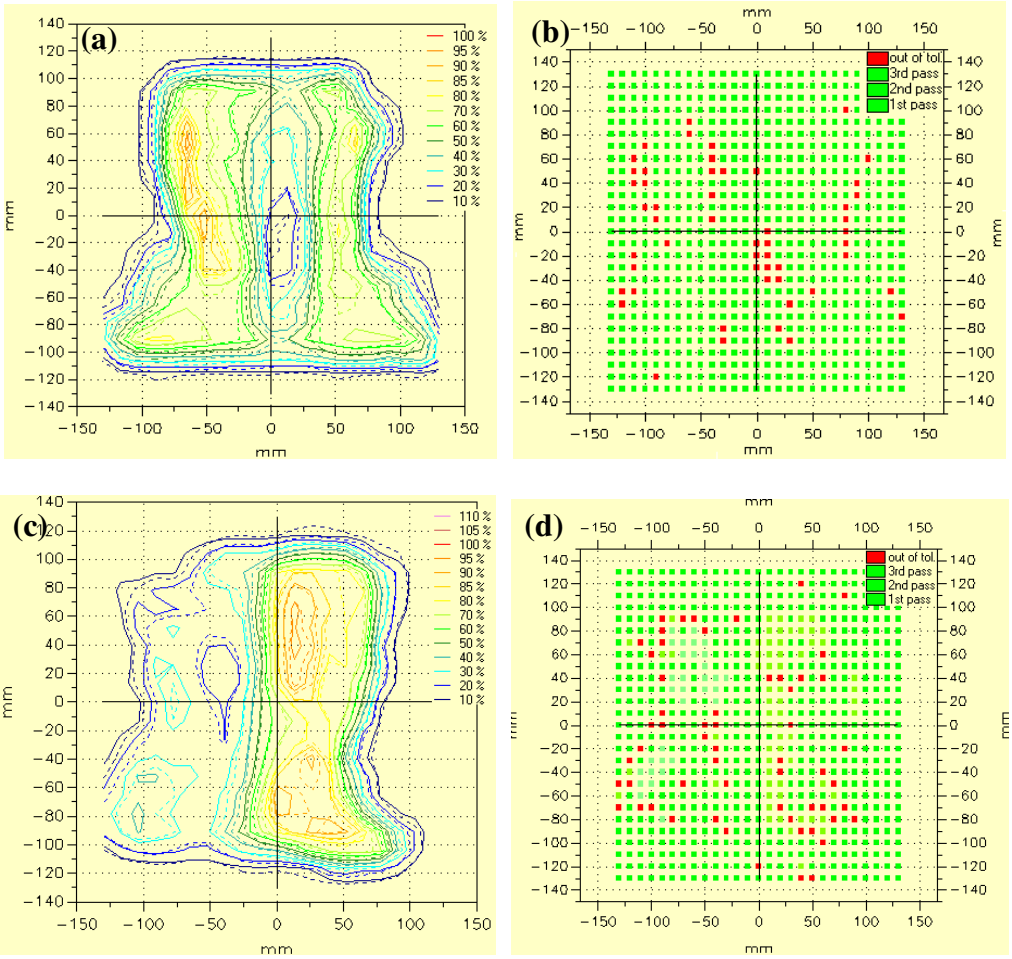

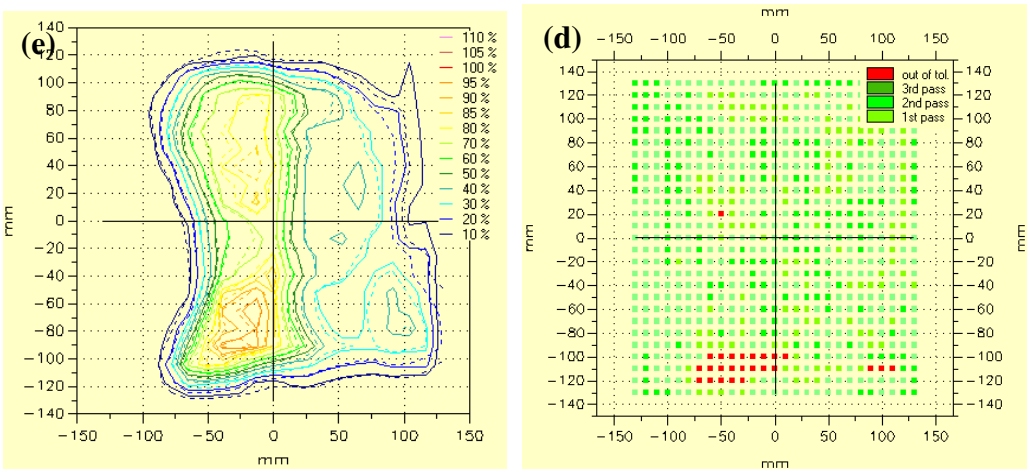

Figure 4.15.The isodose overlay (solid line: TPS; dotted lines: 2D-array) and gamma function pass/fail criteria for three IMRT fields of a head-and-neck treatment plan (a). The green color represents areas where the gamma index criterion is met, and the red color represents areas where the gamma index criterion is not fulfilled.

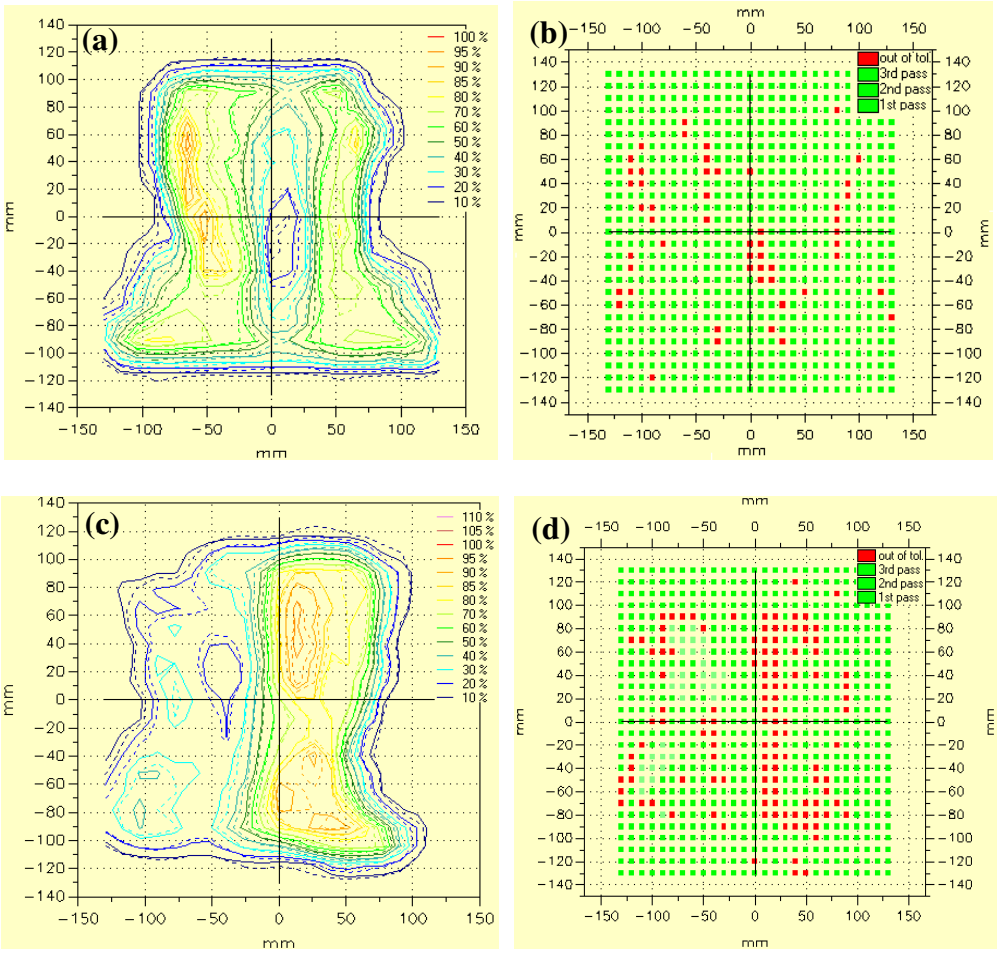

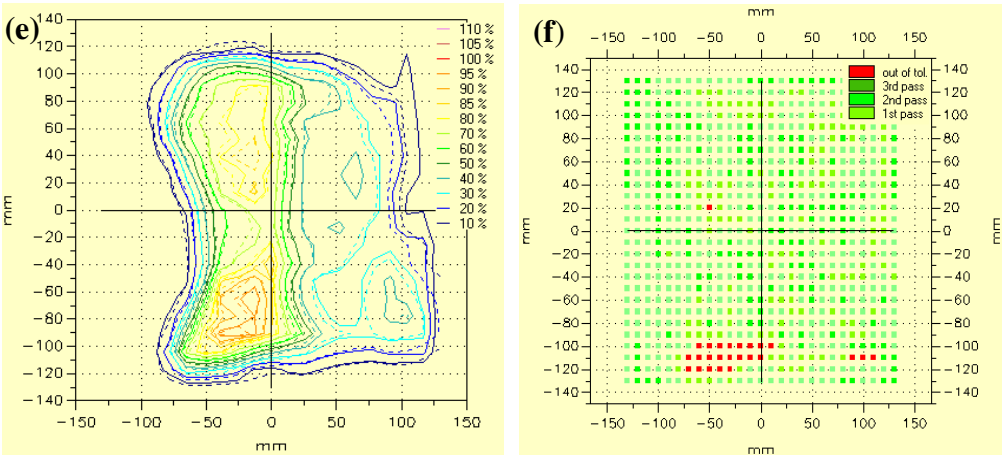

Figure 4.16. Isodose overlays (solid line: TPS; dotted lines: 2D-array) and gamma function pass/fail criteria for three IMRT fields of a head-and-neck-treatment plan (b). The green color represents areas where the gamma index criterion is met, and the red color represents areas where the gamma index criterion is not fulfilled.

Figure 4.17 shows representative axial CT slides that indicate the isodose distributions that were obtained for the two IMRT plans. Both of the IMRT plans met the prescription goal for PTV1 and PTV2. For plan (a), the deviations of D_{90} (Gy) from the prescribed dose were 2.38 and 0.98 Gy for PTV1 and PTV2, respectively. For plan (b), the deviations of D_{90} (Gy) from the prescribed dose were 3.38 and 0.90 Gy for PTV1 and PTV2, respectively. The mean and the maximum dose differences between PTV1 and PTV2 were less than 2%. Tables 4.1 and 4.2 list the $D_{100,}$ $D_{100,}$ $V_{100,}$ $V_{90,}$ mean and maximum dose values for target volumes for both plans. Table 4.3 summarizes the maximum dose received by the organs-at-risk, in which the OAR received doses lower the tolerance doses for each. The DVHs of the target volumes and of the organs-at-risk for both plans are shown in figures 4.18 and 4.19, respectively. The results demonstrated that both IMRT plans were acceptable.

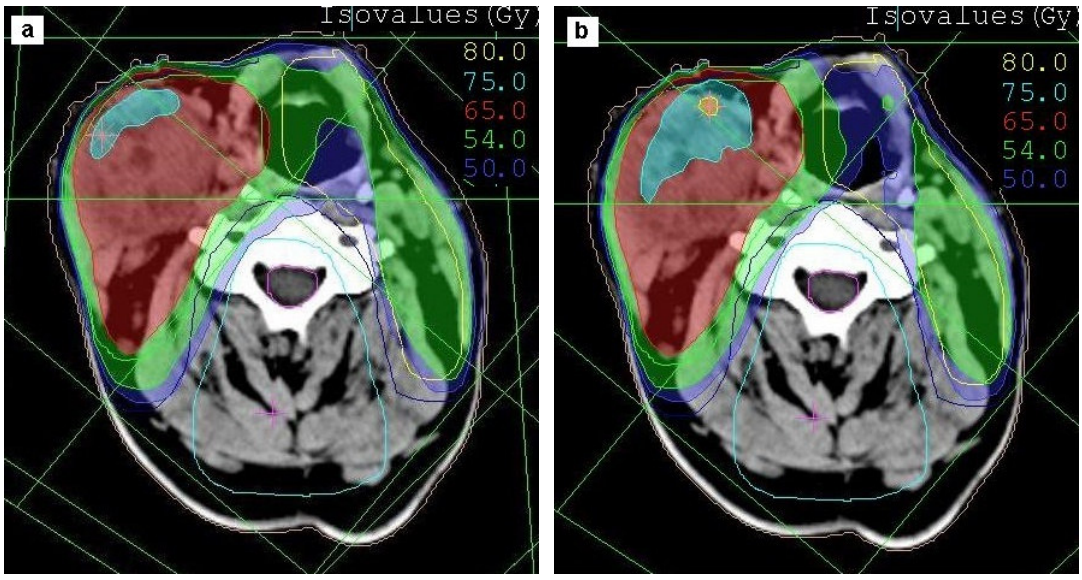

Figure 4.17.The isodose distributions in an axial view in a patient with head and neck cancer. (a): the error-free IMRT plan; (b): the IMRT plan with errors. The colors wash represent sets at 80, 75, 65, 54 and 50 Gy.

Table 4.1. A dosimetric summary of the target volumes for plan (a).

Plan (a)	**D_{100} (Gy)**	**D_{90} (Gy)**	**V_{100} (%)**	**V_{95} (%)**	**D_{mean} (Gy)**	**D_{max} (Gy)**
PTV1	22.15	51.62	84.76	91.34	61.27	82.72
PTV2	38	64.02	87.2	95.58	69.31	80.72

D_{100}: the dose received by 100% of the volume

D_{90}: the dose received by the 90% of the volume

V_{100}: the volume receiving 100% of the prescribed dose

V_{95}: the volume receiving 90% of the prescribed dose

D_{mean}: the mean target-volume dose

D_{max}: the maximum target-volume dose

Table 4.2. A dosimetric summary of the target volumes for plan (b).

Plan (b)	**D_{100} (Gy)**	**D_{90} (Gy)**	**V_{100} (%)**	**V_{95} (%)**	**D_{mean} (Gy)**	**D_{max} (Gy)**
PTV1	21.35	50.62	81.12	87.94	60.95	81.16
PTV2	36.76	64.1	87.82	94.7	70.56	81.16

Table 4.3. A dosimetric summary of organs at risk for both plans.

OAR	**D_{max} (Gy) Plan (a)**	**D_{max} (Gy) Plan (b)**
Brainstem	47.38	46.61
Spinalcord	41.17	39.62
Larynx	57.76	57.35

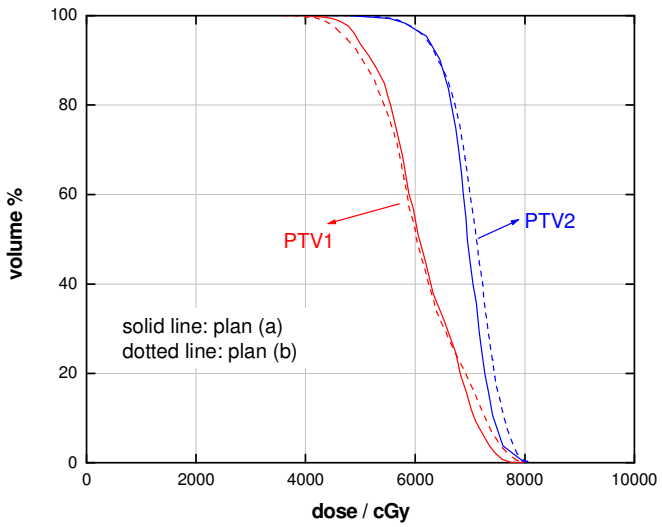

Figure 4.18. A dose-volume histogram of differences between the error-free IMRT plan (solid line) and the IMRT plan with errors (dashed line). The DVH shows PTV1 and PTV2.

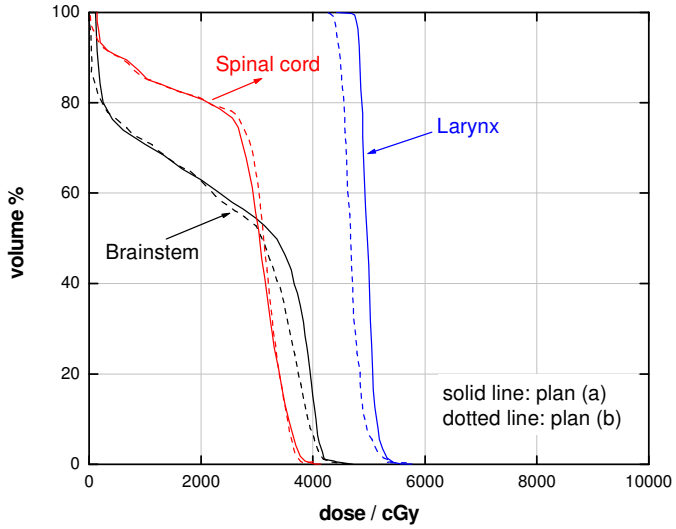

Figure 4.19. A dose volume histogram of differences between the error-free IMRT plan (solid line) and the IMRT plan with errors (dashed line). The DVH shows the organs at risk.

From these results, it can be concluded that the generally accepted norm for fluence map pass/fail criteria does not have a sound foundation in clinical practice. A better approach would be to substitute the measured fluence map into the TPS and recalculate. If the differences are not clinically significant, then treatment can continue; otherwise, the IMRT plan and QA can be repeated.

4.3.4 Kodak EDR2 film dosimetry versus 2D-Array dosimetry systems

Different gamma agreements were obtained for the IMRT fluence map measurements that use the Kodak EDR2 film and the 2D-Array Seven29 dosimetry system as a result of the different characteristics of the two dosimetry systems. The differences in gamma criteria between the Kodak EDR2 film dosimetry system and the TPS and 2D-Array Seven29 dosimetry system with the TPS occurred because of different aspects of the experimental techniques. Although, the currently used version of the VeriSoft gamma evaluation does not report any numerical solutions of the gamma function, instead a pass/fail criterion was implemented. The concomitant agreements for isodose overlay and gamma map evaluations were evaluated visually and judged to be satisfactory.

Table 4.4 shows the time required to complete the experimental procedures for the two different dosimetry systems. As shown from the results, the Kodak EDR2 film dosimetry system required more time than the 2D-Array Seven29 dosimetry system to perform the entire dosimetry procedure. The results demonstrated that the 2D-Array Seven29 detector system is more time efficient and is therefore a more clinically practical measurement device.

Table 4.4 The time required for the different steps of the verification procedure per single IMRT plan.

Step	Kodak EDR2 film (average time)	2D-Array (average time)
Experimental set-up and data collection	1.0 hr	35 mins
Developing/processing	1.0 hr	n/a
Scanning	45 mins	n/a
Analysis of the measurements	1.15 hrs	30 mins

The results show that Kodak EDR2 film is less suitable than the 2D-Array detector system even though EDR2 film has a high spatial resolution and has been commonly used for IMRT patient-specific QA. In addition, the EDR2 film can introduce many dosimetric uncertainties if the film is not used properly. The uncertainties in the experiments can be attributed to different factors as follows. (i) Errors in the film positioning during the experimental procedures. Although some of the results in the extracted beam profiles showed some agreement, there were noticeable errors in many regions of the film where there were areas that did not meet the selected gamma criteria. (ii)The intermittency effect; according to Childress *et al.* (2005), "The intermittency effect refers to the change in a film's OD response when exposed to many small doses compared to a single exposure of the same total dose". Childress *et al*. (2005) clearly indicated that the intermittency effect can introduce uncertainties of greater than 2%. The change in the optical density of the film would cause a significant difference between the EDR2 film dose distribution and the TPS-calculated dose distribution. This is clinically important for IMRT patient-specific QA because the step-and-shoot technique delivers

short bursts of radiation over a substantial period of time. (iii) The effect of the processing time delay for the EDR2 film, which is defined as the time taken between the irradiating and developing stages of the EDR2 film. It has been demonstrated that increasing the time between irradiating and developing EDR2 film can affect the absolute dose response of EDR2 film by between 4 and 6% (Childress *et al*., 2005). Unfortunately, in this experiment, a short period of time was given between the irradiating and developing stages. A previous study showed that a delay of at least one hour between the irradiation and developing of the EDR2 films would guarantee that the film optical density had reached 99% of its stable optical density (Childress *et al*., 2004).

For the comparison of the 2D-Array Sven29 measurements versus the TPS, the areas that did not meet the selected criteria were relatively smaller compared to the EDR2 measurements versus the TPS. The results also proved that the 2D-Array Seven29 dosimetry system has much more promise than the EDR2 film does. However, the 2D-Array Seven29 dosimetry system also has considerable limitations. As mentioned above, the EDR2 film has a high spatial resolution compared to the 2D-Array dosimetry system; here, the measured points for the EDR2 film are almost identical with the TPS-calculated points. This type of resolution cannot be achieved with the 2D-array Seven29 because the ionization chambers within the array are fixed at positions with distances of 5 mm, and the commonly used 2D-Array detector systems (PTW, Freiburg) have a maximum of 729 ionization chambers that are used to evaluate the dose distribution compared to the thousands pixels of the film. This limitation of the sampling resolution of the 2D-Array detector raises questions about the usefulness of 2D-Array dosimetry system compared with film dosimetry. Further study will be useful to develop analysis software for the film to match the calculation method of the 2D-Array detector. This would allow for an accurate representation of the comparison between the 2D-Array detector and EDR2 film for the measurement of IMRT fluence maps.

4.4 Conclusion

The main purpose of this chapter was to evaluate the IMRT dose distributions, to assess the ability of the Kodak EDR2 and 2D-Array Seven29 ionization chamber detector

system to measure the dose distributions and to compare the measured and calculated dose distributions using CMS XiO TPS. The EDR2 film dose distributions showed some agreement with the CMS XiO TPS data using the current criteria of 3%/3mm. The results were confirmed by the beam profiles along the fluence field. The maximum dose difference was approximately 10%. For the 2D-Array Seven29 detector system, the gamma evaluation plot of dose distributions showed an agreement for most of the points between the datasets except for small deviations shown at edges of the field, which were confirmed with the plotted profiles along the field. The maximum dose difference was approximately 8%. In general, the differences in gamma criteria between both dosimetric methods with the TPS resulted from different aspects of the experimental techniques; both dosimetric methods have the ability to identify systematic errors. The obtained results were based on different calculation methods and, as a result, yielded different results for IMRT dose distributions; it was not easy to determine which dosimetry method was a more accurate tool for IMRT dose distributions. Nevertheless, the 2D-Array was demonstrated to be superior to EDR2 film as a result of its ease of set-up. In addition, the results showed that, based on the evaluation of IMRT clinical plans using the pass-rate criteria, the generally accepted norm for the use of a fluence map with pass/fail criteria does not have a sound foundation in clinical practice. A better approach would be to substitute the measured fluence map into the TPS and recalculate. If differences are not clinically significant, then continue with treatment; otherwise, redo the IMRT plan and QA.

Based on the results, the 2D-Array Seven 29 detector system has generally proven to be the detector of choice due to its superior dosimetric characteristics in terms of time efficiency. The 2D-Array Seven29 detector system results were shown to have overall smaller areas that failed to meet the given criteria compared to Kodak EDR2 film. Additionally, the 2D-Array Seven29 detector system significantly reduced the amount of time to perform measurement procedures and analyses. Although the EDR2 film has a high resolution, but a reduced cost efficiency; it proved to be a very unreliable tool for performing IMRT patient-specific QA, especially in a busy department. The EDR2 film required twice the time required by the 2D-Array to perform the measurements and triple

the time for the entire process (i.e., developing, scanning and analysis of the results). Therefore, the time required to perform patient-specific QA for IMRT is very inconvenient in a busy clinical setting. The accuracy of EDR2 film is also reduced because of the insensitive nature of the EDR2 film, which requires almost ideal processing conditions and calibration. However, the accuracy could be improved by utilizing more accurate film dosimetry procedures, which is a potential topic for follow-up studies. The study concludes that the 2D-Array Seven29 dosimetry system is a practical dosimetric tool that is both reliable and time-saving for patient-specific QA for IMRT.

5. The application of an amorphous silicon electronic portal imaging device for IMRT pre-treatment verification

5.1 Introduction

The intensity modulated radiation therapy (IMRT) technique requires new and accurate methods and tools for the verification of dose delivery. Numerous dosimetric methods are used for quality assurance (QA) of the IMRT. The commonly used method for dose delivery verification is film dosimetry. Although several radiation oncology clinics have used a film dosimetry system for patient-specific QA for IMRT (Dogan *et al*., 2002;Winkler *et al.,* 2005; Budgell *et al.,* 2005; Bucciolini *et al.,* 2007; De Martin *et al.,* 2007), film dosimetry is not the only dosimetry technique that is used. Other dosimetric devices for 2D dose measurements include 2D diode arrays, ionization chamber arrays (Buonamici *et al*., 2007; Jursinic and Nelms 2003) and electronic portal imaging devices (EPIDs) (Warkentin *et al.,* 2003; Van Esch *et al.,* 2004; Talamonti *et al.,* 2006; Howell *et al.,* 2008; Wendling *et al.,* 2006; van Zijtveld *et al.,* 2007). EPIDs have been adapted for dosimetric purposes and are increasingly used. Several studies have confirmed the appropriateness of the amorphous silicon EPIDs for IMRT portal dosimetry (Talamonti *et al.,* 2006; Greer and Popescu 2003; McCurdy *et al.,* 2001; Kavuma *et al*., 2008). Recently, van Elmpt *et al.* (2008a) published a review of EPID dosimetry. A number of studies of EPID dosimetric characteristics have been conducted. The a-Si EPID response is linear with the dose and is dose-rate dependent, which is advantageous in providing accurate portal dosimetry. However, the conversion of the EPID signal into a dose is a complicated procedure; the field-size-dependent output factors and EPID response kernels need to convert the acquired EPID images into 2D dose distributions with or without using a beam attenuator (Warkentin *et al.,* 2003; Winkler *et al.,* 2007; McCurdy *et al.,* 2001).

There are different methods used in EPID dosimetry. It can be used for pre-treatment verification, in which the dose distribution in the plane of the detector is measured with or without an attenuator in the beam (van Esch *et al.,* 2004; Howell *et al.,* 2008; van Zijtveld *et al.,* 2006). However, portal dose measurements are used to reconstruct the

dose in the phantom (Wendling *et al.,* 2006; Van Zijtveld *et al.,* 2007; McDermott *et al.,* 2006; Van Elmpt *et al.,* 2008b). EPID dosimetry can also be performed using a beam attenuator in the treatment path (McDermott *et al.,* 2007; Van Zijtveld *et al*., 2009).

Recently, EPID dosimetry has been considered superior to the film dosimetry method. The main advantages of using an EPID instead of film are that EPID measurements are easy to perform; the experimental set-up can be simple; and the data can be obtained digitally, are easy to handle and can be used directly for processing. In addition, EPID produces more reproducible results and eliminates film processing problems. Additionally, EPIDs are built-in at the Linac's gantry; this makes them ideally suited for measuring individual fields at the treatment gantry angles, which is a more complicated task with film. At the Department of Radiation Oncology, SBAH, the film dosimetry system has been used for IMRT patient-specific QA. Recently, we found that the film is less suitable than the 2D-Array dosimetry system. However, the aim of this chapter to is develop a dosimetric set-up for a-Si EPID for use in IMRT pre-treatment verification. An experimental set-up has been developed and validated for portal dosimetry using Siemens equipment for the pre-treatment verification of individual fields of head-and-neck IMRT plans, and the criteria for analysis have been established. The measured portal images are compared with the calculated IMRT plans at the level of the EPID without any scatter material between the source and the detector.

5.2 Materials and methods

For dosimetric purposes, a comprehensive calibration of the a-Si EPID is required. This includes gain calibration, dose linearity, an evaluation of the a-Si EPID stability, field-size dependence, the ghosting effect, the effect of build-up, the effect of the transmission thickness and the conversion of the EPID grayscale value into EPID dose values. These parameters were investigated in detail in chapter 3.

5.2.1 IMRT dose maps

5.2.1.1 EPID dose maps

The portal images were acquired with the available amorphous silicon electronic portal imaging device (a-Si EPID) (OPTIVUE 1000ART) incorporated in a Siemens ONCOR Linac (Siemens Medical solutions, Concord, USA), which was equipped with 160-leaf standard MLC. The linac produced 6 and 15 MV photons with two different dose-rate modes. The a-Si EPID detector had an imaging area of 40 cm x 40 cm. The detector utilized 1,024 x 1,024 pixels, with a pixel size of 0.8 mm (there are more details about the imager in chapter 3). The IMRT plans were downloaded from the network to be treated at the EPID. No attenuator was used in the beam axis. The IMRT plans were measured using the EPID by acquiring the EPID images for the different IMRT fields. The acquired fluence images were measured with the EPID at a depth of maximum dose for each energy used in the IMRT fields. The source-to-detector (SDD) distance was chosen such that the maximum dose fell within 115 cm, with the gantry angle zero degree perpendicular to the beam axis. The acquired EPID images were then saved to be imported and analyzed for comparisons with the calculated CMS XiO treatment planning dose maps for the same set-up. The EPID experimental set-up and the CMS XiO TPS calculation phantom are shown in figure 5.1.

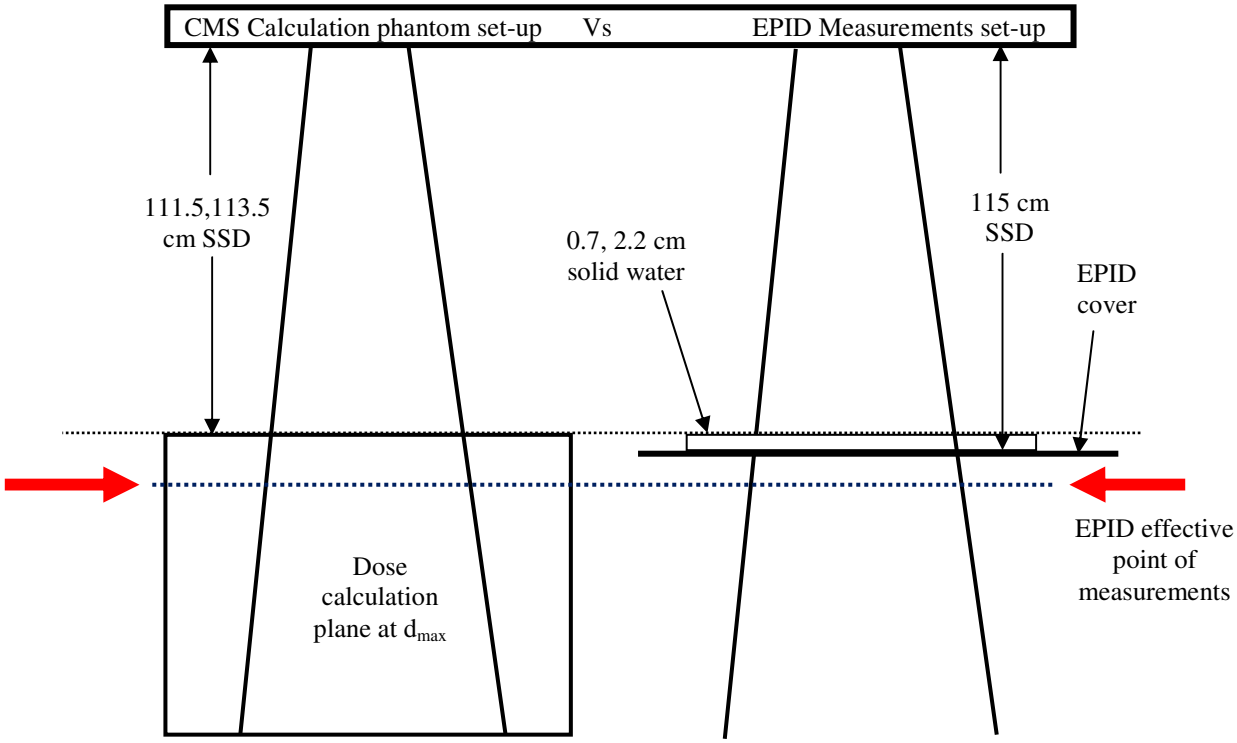

Figure 5.1. A diagram of the EPID experimental set-up for acquiring EPID images versus the CMS XiO TPS calculations set-up on a homogenous phantom for the comparisons.

5.2.1.2 CMS XiO TPS dose maps

In this study, the IMRT dose maps were calculated by using a CMS XiO TPS (CMS, St. Louis, MO). Three IMRT plans were used for the verifications. All three plans were for the head-and-neck and used a step-and-shoot IMRT treatment technique; each plan contained five fields except for the third plan, which had only three fields. The convolution algorithm and a 2.5-mm grid spacing were used for dose calculations in these plans.

For the IMRT quality assurance procedure, the CMS XiO treatment planning system offers different options to ensure that treatment is verified and delivered properly. These options include relative dosimetry and absolute dosimetry. Here, the relative QA option was used to recreate the dose for individual beams perpendicular to a flat, homogenous phantom without the need to create a separate plan after the IMRT plan was completed. The dose was then normalized to 100% along the weight-point fan. The IMRT plans were

calculated using the field-related approach, in which each treatment field was reset to deliver the dose within the beam in a plane perpendicular to the central beam axis and to the phantom for a gantry angle of zero degrees. The plans were performed using isocentric techniques. The source-to-detector distance (SDD) was chosen as approximately115 cm. The weight of each beam was recalculated to deliver the dose at 1.5 and 3.5 cm depths in water for 6 and 15 MV intensity-modulated fields, respectively, while maintaining the same number of monitor units as that found in the original patient plan.

The calculated dose maps were saved with a unique file name, and the IMRT plans were then transferred through the LANTIS network in preparation for treatment. The IMRT plans for each treatment field were imported to RIT 113 software Version 5.2 (Colorado Springs, CO) to be compared with the acquired EPID images to a verification phantom. Figure 5.1 shows the experimental set-up of the calculated and measured dose maps.

5.2.2 Dose map comparison methods

For the comparisons of the measured IMRT dose maps using the a-Si EPID to the calculated dose maps using CMS XiO TPS, the dose distributions were evaluated for three IMRT plans that contained 15 IMRT fields. All of the acquired EPID images were stored as DICOM files, and all of the calculated dose maps were saved as ASCII files. Both datasets were imported for analysis and evaluation, which were performed by using Radiological Imaging Technology (RIT) 113 Dosimetry Software, Version 5.2 (Colorado Springs, CO). The software currently available in the department does not have the functionality to compare EPID images, and a third party was approached to evaluate their software.

The RIT 113 software introduced a new calibration method called plan-based calibration. This method can be used to develop relative dosimetric calibration curves between the TPS-calculated dose maps and the acquired EPID images or between the treatment TPS-calculated dose maps and the 2D-Array images. This method allows a relative dose comparison to be conducted without conducting a separate calibration. The calculated

dose maps that are obtained using the CMS XiO TPS from the IMRT fields will first be normalized to their maximum values; this will be followed by the creation of a dose histogram. The dose histogram will be obtained by dividing the calculated dose map into dose bins. Here, both the calculated dose maps and the acquired EPID images will be registered, and by using the mean dose value on the pixels found on each image, a calibration curve will be created. The calibration curve will be used to convert the obtained EPID images and the treatment planning images into dose maps for comparison.

In the RIT software, the data were classified into two categories for comparison: the target images and the reference images. Here, the EPID images are denoted as target images, and the calculated treatment-planning dose maps are considered reference images. This software also allows the acquired image to be converted into a dose image and provides a host of regular MLC and IMRT QC analysis routines for the images. These routines provide a suite of measurements and dose map comparisons including gamma function, dose profiles and isodose overlay plots, and subtraction and pixel histogram distributions. The agreements between the measured and calculated data were assessed for each field based on a gamma function algorithm (Low *et al.,* 1998) with the DTA and ΔD_{max} criteria of 3 mm and 3%, respectively.

The software also provides different comparison criteria, such as isodose overlay, gamma maps and the subtraction of gamma maps, for the target and the reference image. For the RIT 113 software, the gamma method is implemented such that a gamma value is calculated with the value 1 corresponding to the 3 mm and 3% criteria. Thus, any gamma values< 1 meet the criteria.

5.3 Results and discussion

The results obtained for the comparisons of the measured dose maps using the a-Si EPID to the calculated dose map using the CMS XiO TPS are presented in this section. A comparison between the calculated dose maps generated by the CMS XiO TPS and the measured dose maps generated by the a-Si EPID using the gamma evolution method will be described in the subsections.

5.3.1 IMRT dose maps

The acquired dose maps using the a-Si EPID were saved as DICOM images, and the calculated dose maps using the CMS XiO TPS were saved as ASCII files. These dose maps were saved in separate files to be used for the comparisons.

5.3.2 Dose map comparison methods

5.3.2.1 Isodose color wash

Figures 5.2 to 5.6 show examples of isodose color wash comparisons of the measured dose maps using a-Si EPID (left) with the calculated dose maps using the CMS XiO TPS (right) for the first IMRT plan, which contains five IMRT fields: the right-posterior oblique, anterior, left-posterior oblique, right-anterior oblique and left-anterior oblique fields. The measured and calculated dose maps were normalized to the maximum values in a homogenous region. Figures 5.2 (a) and 5.2 (b) show the results of the 2D dose maps that were measured with the a-Si EPID and calculated with the CMS XiO TPS for the right-posterior oblique field. The dose map comparison shows a close agreement between the IMRT fields. For the five IMRT fields (figures 5.2 to 5.6), the isodose color wash comparisons were evaluated visually and were determined to be satisfactory. The quantitative assessment (isodose overly, gamma index, dose profiles, etc.) of the agreements between the dose maps can be performed using the gamma analysis method with the RIT 113 Software. More details on the quantitative assessments are shown in subsequent sections.

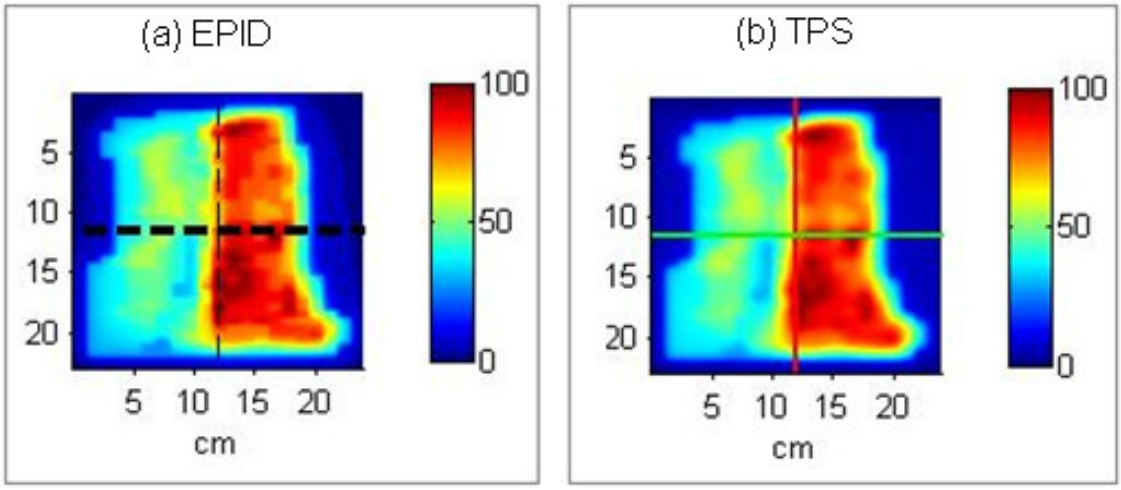

Figure 5.2. A comparison between (a) the dose maps measured with a-Si EPID versus (b) the dose maps calculated with the CMS XiO treatment planning system for the right-posterior oblique field.

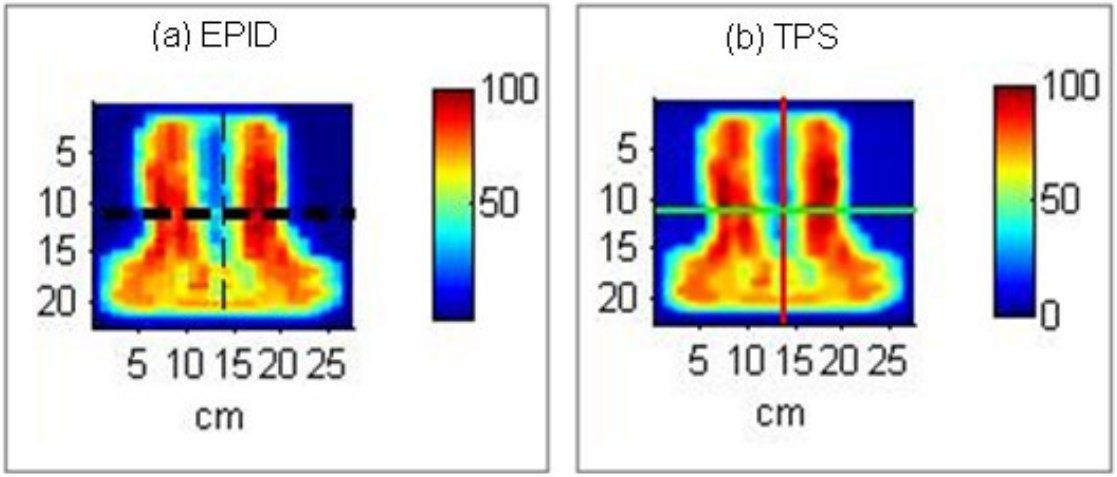

Figure 5.3. A comparison between (a) the measured dose maps with a-Si EPID versus (b) the calculated dose maps using the CMS XiO treatment planning system for the anterior field.

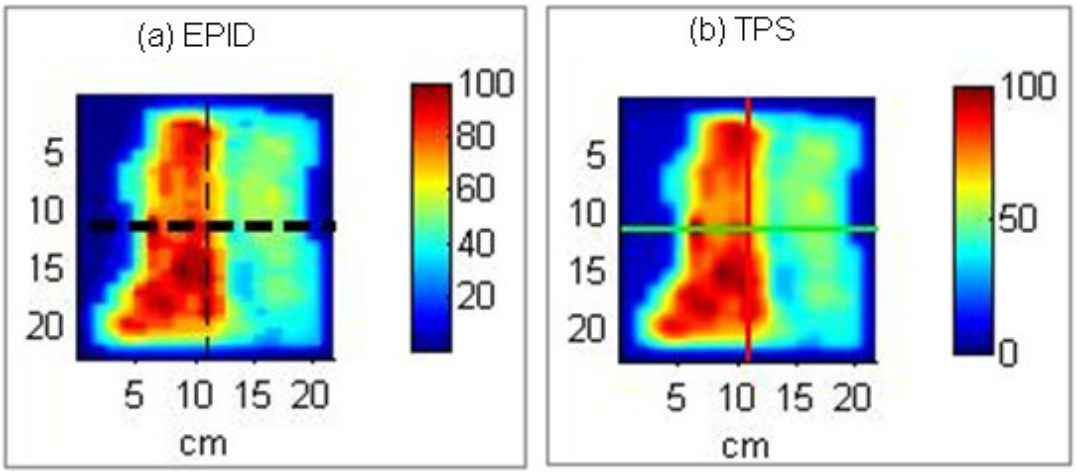

Figure 5.4. A comparison between (a) the dose maps measured with a-Si EPID versus (b) the dose maps calculated with the CMS XiO treatment planning system for the left-posterior oblique field.

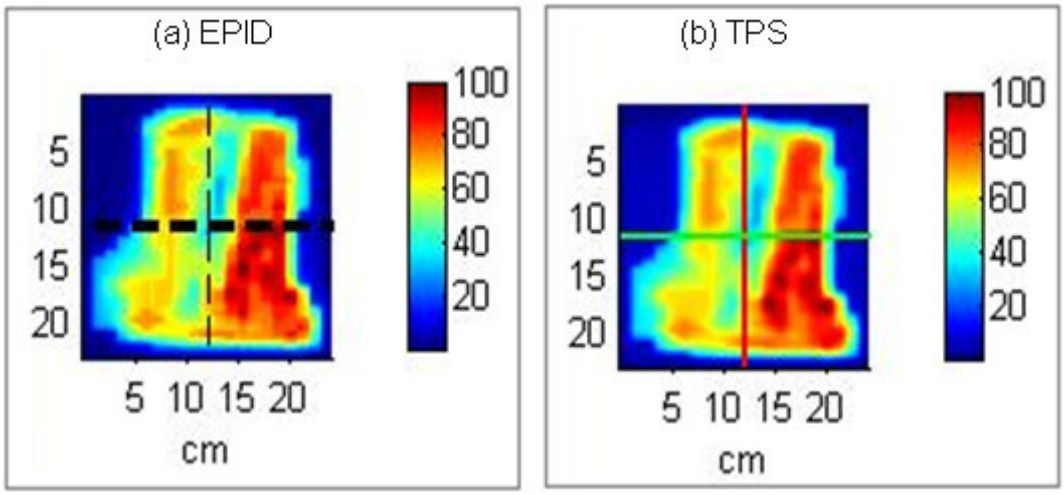

Figure 5.5. A comparison between (a) the dose maps measured with a-Si EPID versus (b) the dose maps calculated with the CMS XiO treatment planning system for the right-anterior oblique field.

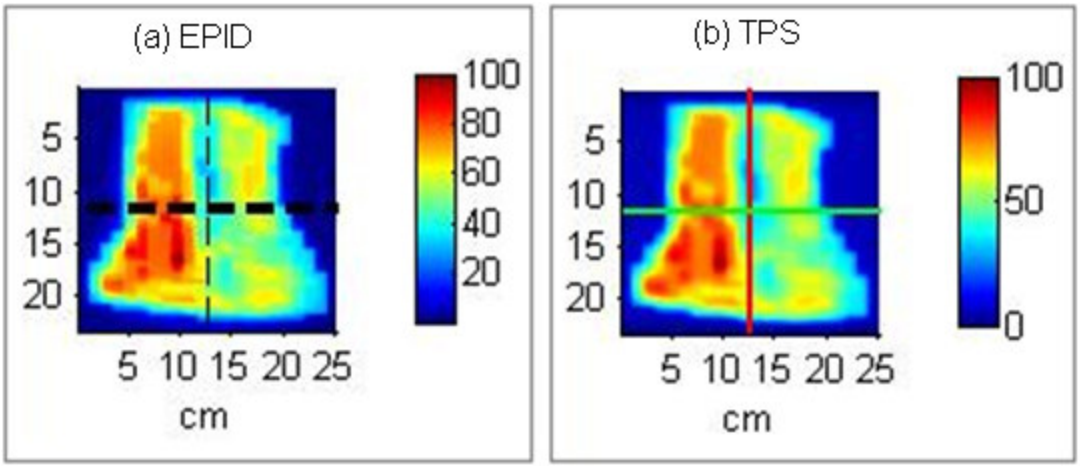

Figure 5.6. A comparison between (a) the measured dose maps with a-Si EPID versus (b) the calculated dose maps using the CMS XiO treatment planning system for the left-anterior oblique field.

5.3.2.2 Gamma evaluations

For a quantitative evaluation of the agreement, the gamma criteria were used. As commonly accepted, the reference values for the agreement are 3% and 3 mm for the dose differences and distance-to-agreement, respectively. Figures 5.7 to 5.11 show examples of gamma evaluations for the five IMRT fields. Although the viewer options in the EPID dosimetry software permit the user to apply different settings in the presentation of the gamma maps, a default setting was chosen that displayed areas with gamma values less than or equal to 1.0 (agreement is within the 3%/3mm criteria) in gray and areas with gamma values greater than 1.0 (agreement outside the 3%/3mm criteria) in red. Figure 5.7 (a) shows the isodose overlay of the measured and calculated dose maps depicted together for the first IMRT field, the right-posterior oblique field; the isodose lines correspond with dose values of 30, 40, 50, 70, and 90 cGy. In figure 5.7 (b), the corresponding gamma map shows that most of the field has gamma values of less than or equal to 1.0 (indicated by the large area shown in gray); the small area in the center of the field has gamma values that are greater than 1.0, corresponding to a high dose-gradient region (shown in red). In addition, there are areas at the edges of the field (shown in red) that show gamma values greater than 1.0; most of these areas fell outside the treatment field. Because the majority of the field has gamma values less than or equal to 1.0, and

areas with gamma values greater than 1.0 are confined to a high dose-gradient region, there is agreement between the measured and TPS-calculated dose maps.

The results were confirmed by evaluating the percentage of pixels that did not meet the specific criteria for each field. The percentage difference refers to the percentage of the measured pixels that did not meet the criteria (shown in table 5.2). For the first IMRT field, the right-posterior oblique field (as shown in figure 5.7), the portal dosimetry software yielded acceptable results. Of the 55,209 pixels that were analyzed, only 4,862 pixels, or 8.81% of the total pixels, had a gamma value greater than 1.0. The second IMRT field, the anterior field, is shown in figure 5.8; this field resulted in the largest discrepancy, with 22.67% of the pixels analyzed having a gamma value of greater than 1.0. Figures 5.9 to 5.11 show the gamma evaluation results for the other three IMRT fields: the left-posterior oblique, the right-anterior oblique and the left-anterior oblique fields.

All of the IMRT fields showed reasonable qualitative results. A summary of the agreement results for the 15 IMRT fields is shown in table 5.2. Agreement (gamma index less ≤ 1.0) of 90% or more was found for the IMRT fields. The minimum discrepancy or percentage difference was 4.25%, the maximum discrepancy was 23.49%, and the average discrepancy was 13.54%, with a 6.72% standard deviation.

In all of the compared results for the IMRT fields, the discrepancies were usually highest in areas around the field edges. These effects were also found in other studies (Howell *et al.,* 2008) and can be traced back to the registration steps in the images during the analysis phase. From the results, it was also demonstrated that 15 IMRT fields were acceptable. The experimental set-up used to validate the calculated dose maps was highly satisfactory. In general, an agreement between the measurements and the calculations and the comparisons demonstrated the robustness of the a-Si EPID for IMRT pre-treatment verification purposes.

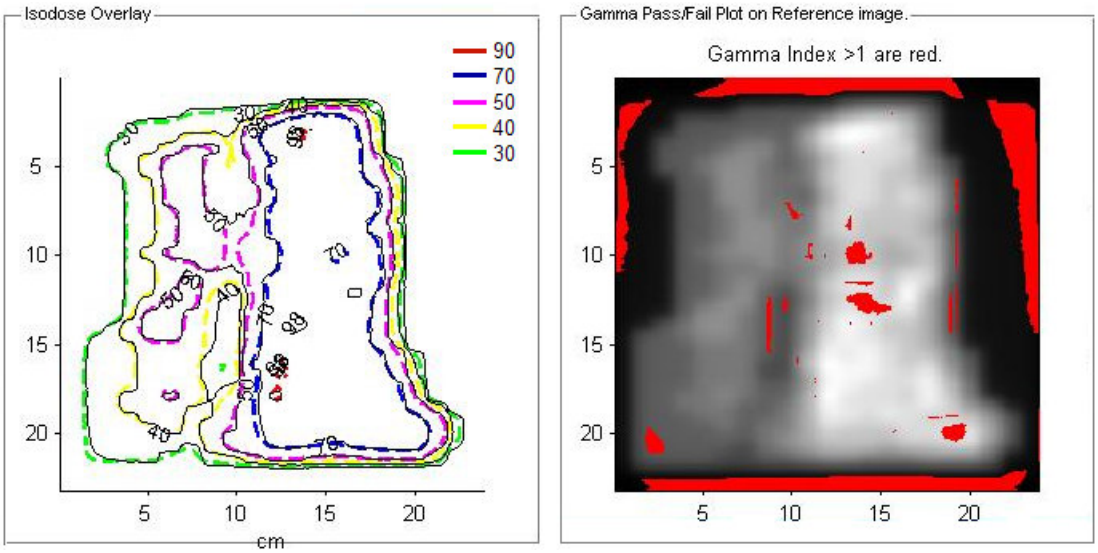

Figure 5.7. A comparison between the right-posterior oblique IMRT field and the left isodose overlay; a-Si EPID isodoses are depicted as dashed lines, and CMS XiO TPS isodoses are depicted as solid lines (doses are specified in cGy). Right, a gamma map plot. The gamma index was ≤ 1 for the DTA and the ΔD_{max} criteria of 3 mm and 3%, respectively.

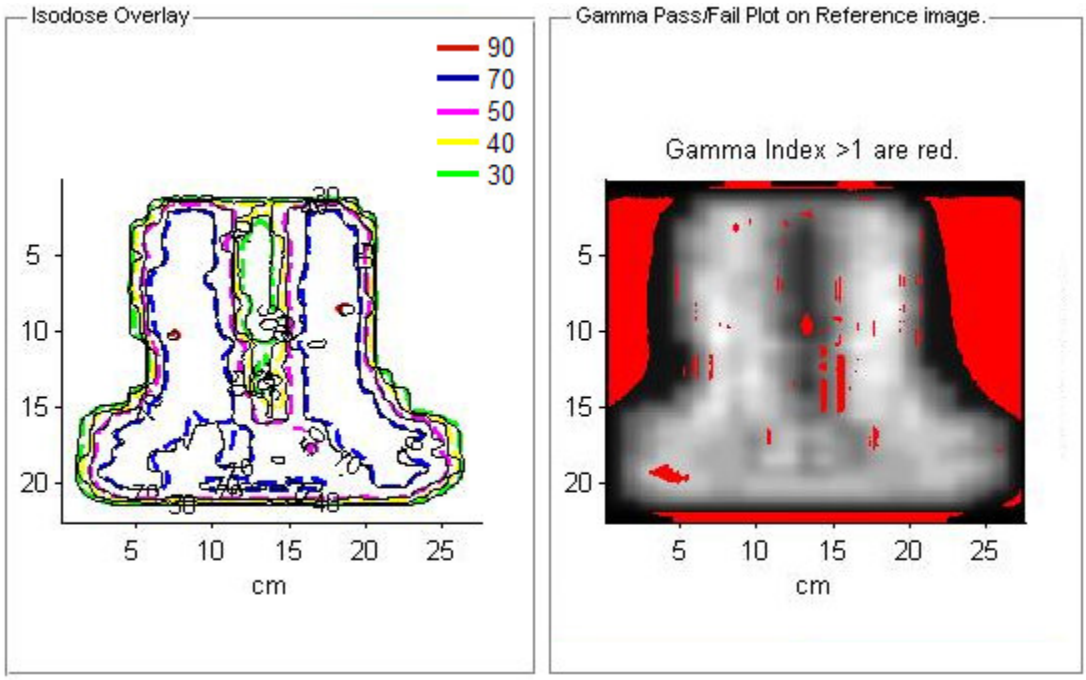

Figure 5.8. A comparison between the anterior IMRT field and the left isodose overlay; a-Si EPID isodoses are depicted as dashed lines, and CMS XiO TPS isodoses are

depicted as solid lines (doses are specified in cGy). Right, a gamma map plot. The gamma index was ≤ 1 for the DTA and the ΔD_{max} criteria of 3 mm and 3%, respectively.

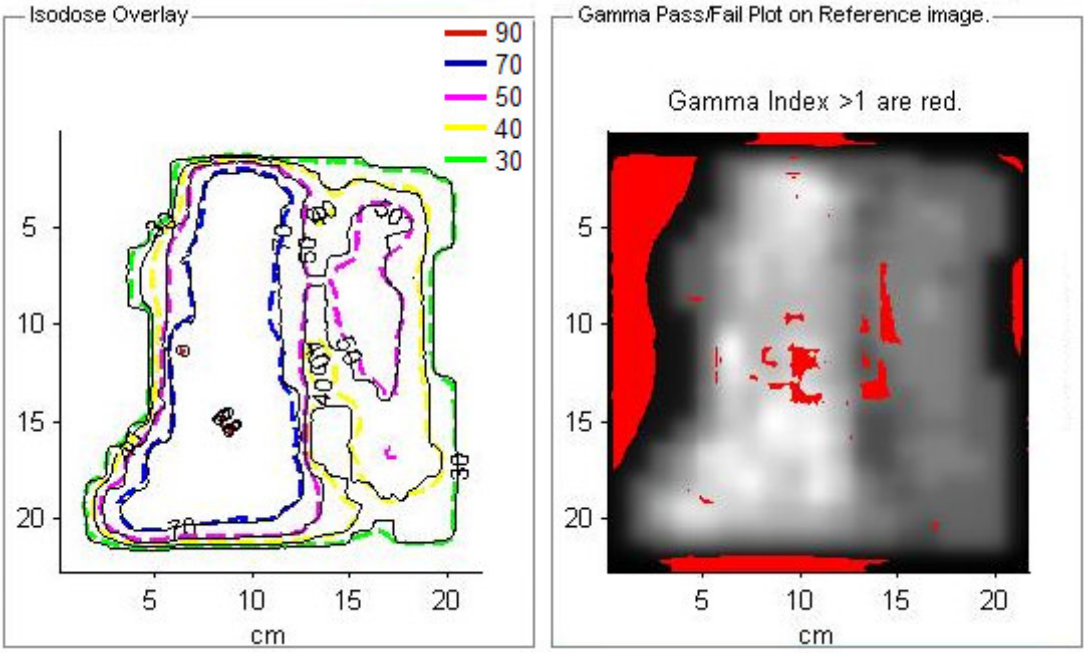

Figure 5.9. A comparison between the left posterior oblique IMRT field and the left isodose overlay; a-Si EPID isodoses are depicted as dashed lines, and CMS XiO TPS isodoses are depicted as solid lines (doses are specified in cGy). Right, a gamma map plot. The gamma index was ≤ 1 for the DTA and the ΔD_{max} criteria of 3 mm and 3%, respectively.

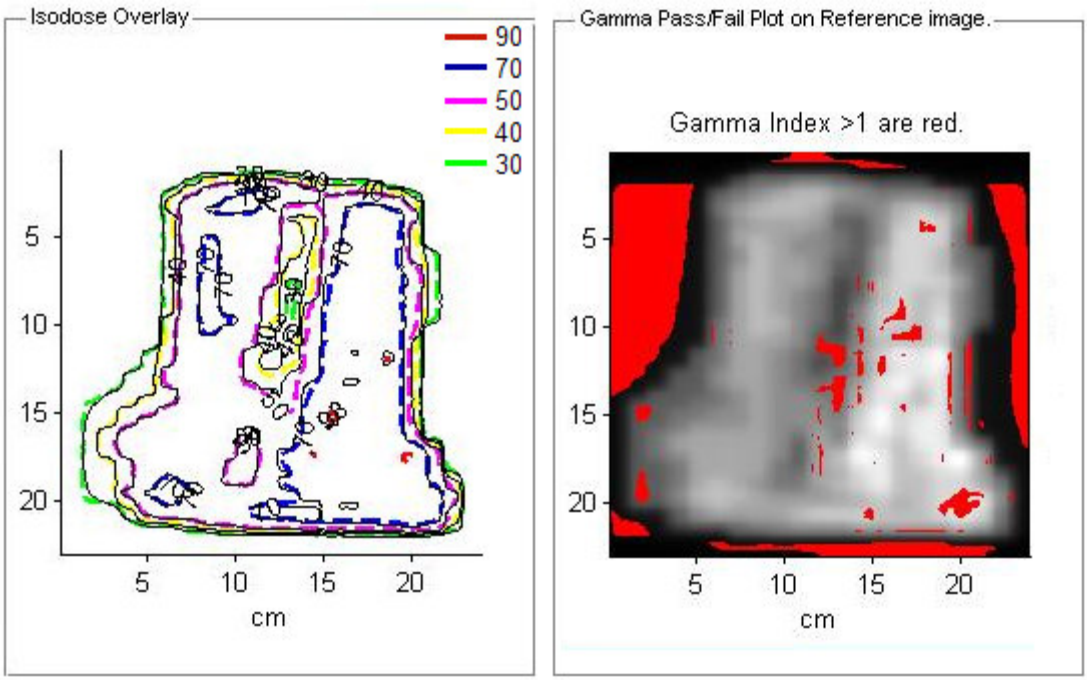

Figure 5.10. A comparison between the right anterior oblique IMRT field and the left isodose overlay; a-Si EPID isodoses are depicted as dashed lines, and CMS XiO TPS isodoses are depicted as solid lines (doses are specified in cGy). Right, a gamma map plot. The gamma index was ≤ 1 for the DTA and the ΔD_{max} criteria of 3 mm and 3%, respectively.

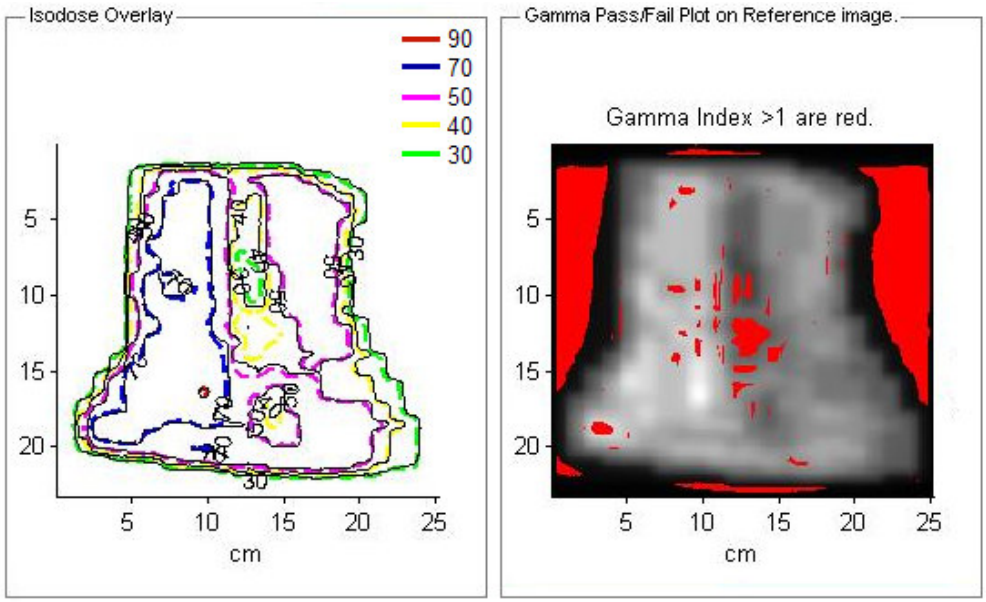

Figure 5.11. A comparison between the left anterior oblique IMRT field and the left isodose overlay; a-Si EPID isodoses are depicted as dashed lines, and CMS XiO TPS isodoses are depicted as solid lines (doses are specified in cGy). Right, a gamma map plot. The gamma index was ≤ 1 for the DTA and the ΔD_{max} criteria of 3 mm and 3%, respectively.

Table 5.1. A summary of the results for 15 IMRT fields using the gamma criteria of 3% and 3mm for the dose difference and distance-to-agreement, respectively.

Field number	Total number of pixels	Total number of matching pixels	Percentage difference
1	55,209	50,346	08.81%
2	81,875	63,316	22.67%
3	49,259	44,491	09.68%
4	55,209	48,247	12.61%
5	58,483	49,524	15.32%
6	47,765	37,135	22.25%
7	57,479	49,852	13.27%
8	54,731	46,262	15.47%
9	50,561	38,781	23.30%
10	52,789	46,486	11.94%
11	52,741	48,273	08.47%
12	46,989	44,992	04.25%
13	56,715	43,391	23.49%
14	49,473	46,845	05.31%
15	49,557	46428	06.31%

5.3.2.3 Subtraction histogram

Figure 5.12 shows an example of the results of the subtraction histogram extracted from the dose differences between the measured and the calculated dose maps on a pixel-by-pixel basis for one IMRT plan. These results were obtained by setting the dose difference

to 3% and the distance-to-agreement to 3 mm. The graph exhibited a distribution centered on zero, which showed that the differences are statistically distributed around ±3 dose differences. The results confirm that an average of 85% of the pixels are within ±3%.

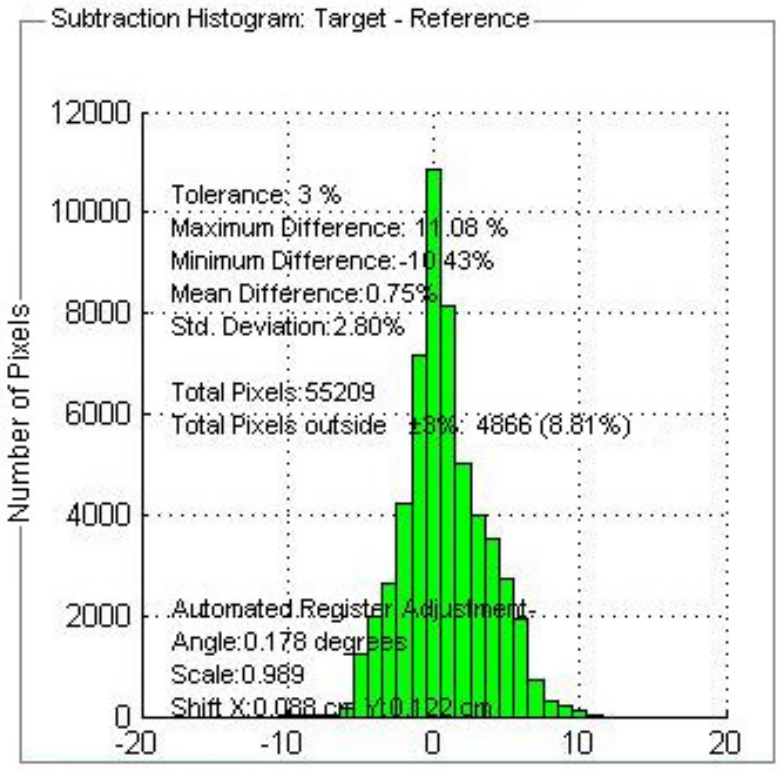

Figure 6.12. The subtraction histogram for the target and reference images.

5.3.2.3 Relative dose profile

Figures 5.13 to 5.17 show examples of beam profiles extracted from the five IMRT fields as indicated by the lines across the isodose color wash that correspond to the five displayed IMRT fields in sections 5.3.2.1. The vertical profiles are shown in red solid lines, and black dashed lines correspond to reference images and target images, respectively, whereas the horizontal profiles are shown in green solid lines and black dashed lines corresponding to the reference images and the target images, respectively. In both profiles, the corresponding dose differences are plotted in blue lines, which are measurements that fell between ±3 dose differences. The obtained dose profiles were in close agreement, as shown previously in the dose maps. These results also confirmed the dose map correspondences.

Using the 3%/3mm gamma criteria, the agreement (gamma index less than or equal to 1) between the measured and the calculated dose profiles was good. Figures 5.13 to 5.17 show that most of the agreements are at the center of the fields for the five IMRT fields. The results also showed that there were clear discrepancies around the edges of the fields. The details of agreement between measured and calculated dose profiles for each field are shown in table 5.3 and figure 5.18.

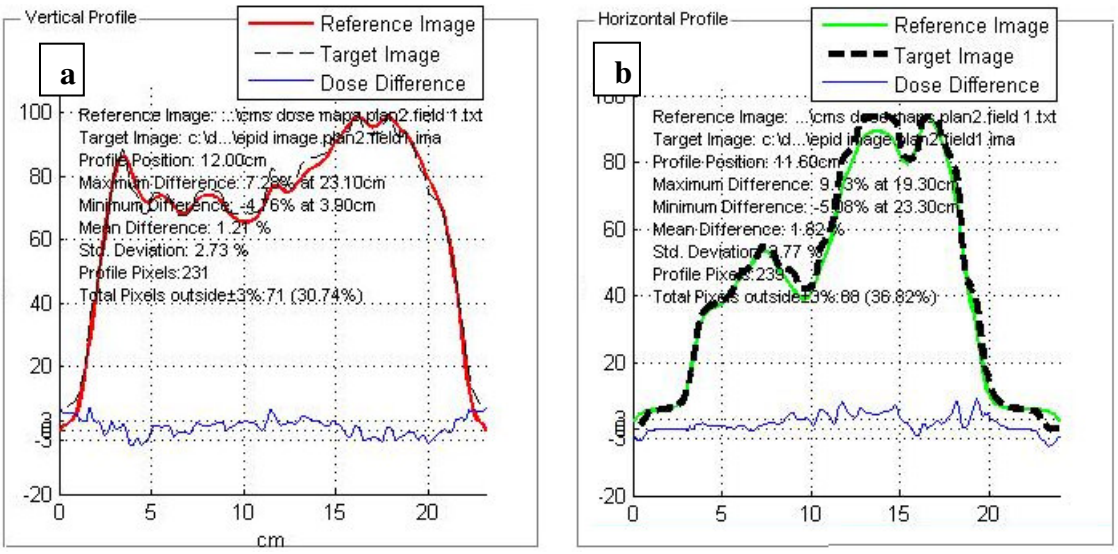

Figure 5.13. (a) vertical and (b) horizontal dose profiles measured and calculated along the lines of the a-Si EPID images and the CMS XiO TPS images and the corresponding dose difference profiles for the right-posterior oblique field. The DTA and the ΔD_{max} criteria were 3 mm and 3%, respectively, were used.

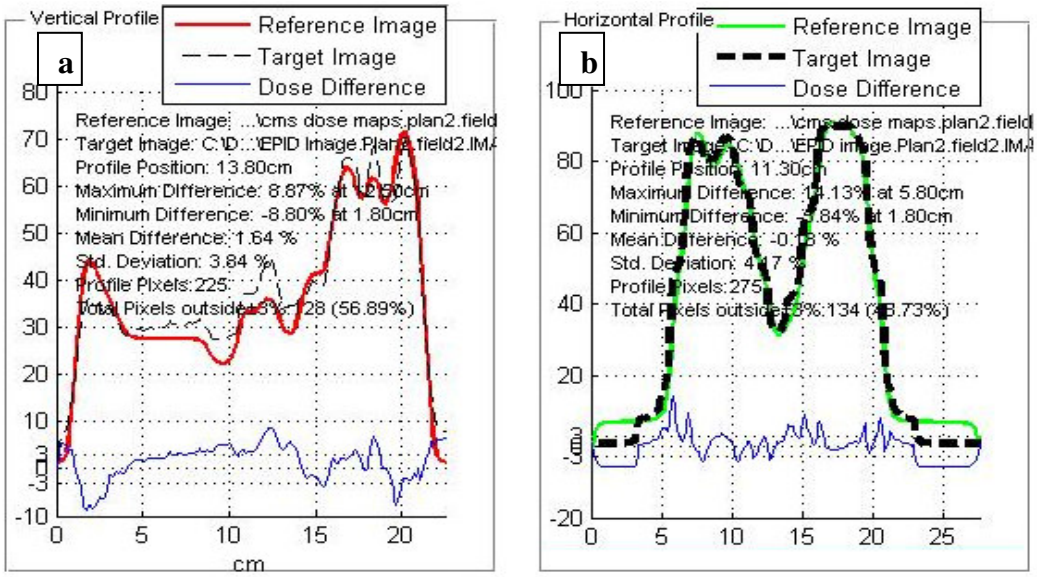

Figure 5.14. (a) vertical and (b) horizontal dose profiles measured and calculated along the lines of the a-Si EPID images and the CMS XiO TPS images and the corresponding dose difference profiles for the anterior field. The DTA and the ΔD_{max} criteria of 3 mm and 3%, respectively, were used.

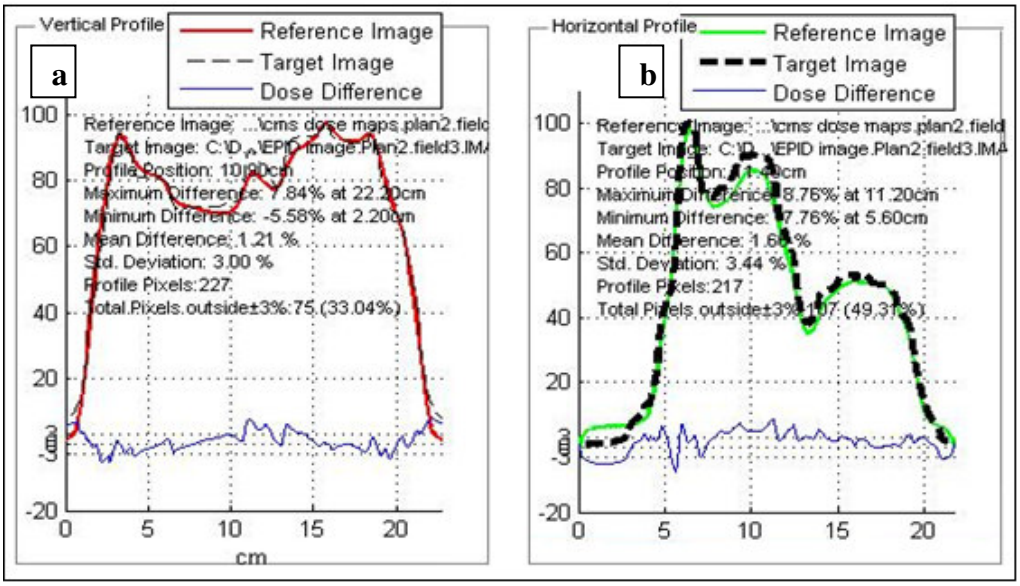

Figure 5.15. (a) vertical and (b) horizontal dose profiles measured and calculated along the lines of the a-Si EPID images and the CMS XiO TPS images and the corresponding dose difference profiles for the left-posterior oblique field. The DTA and the ΔD_{max} criteria of 3 mm and 3%, respectively, were used.

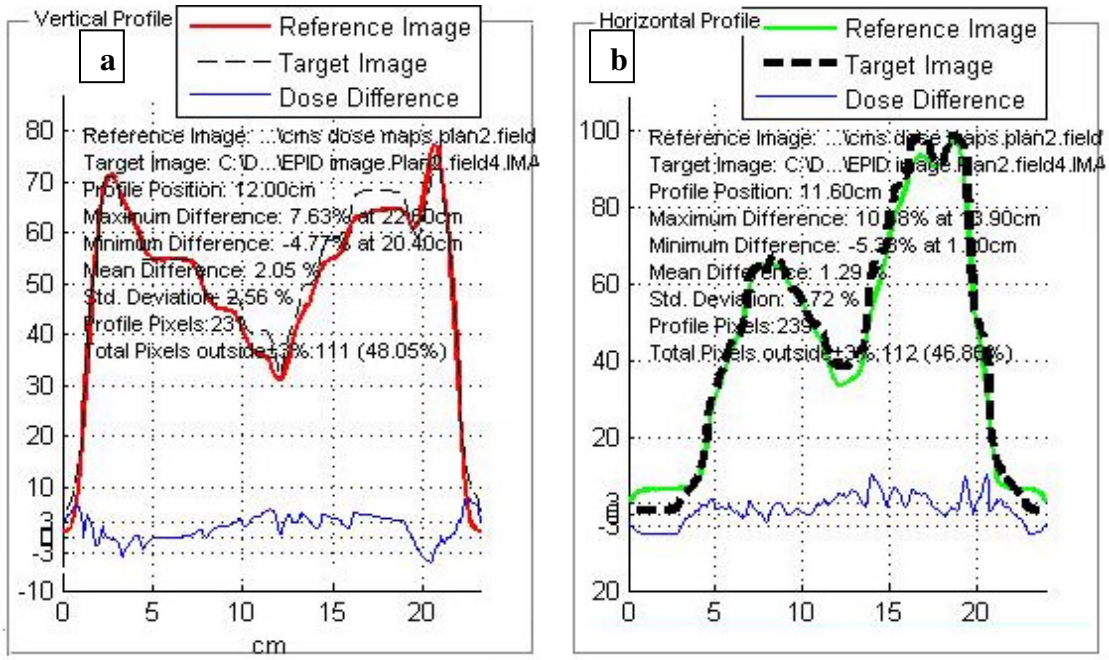

Figure 5.16. (a) vertical and (b) horizontal dose profiles measured and calculated along the lines of the a-Si EPID images and the CMS XiO TPS images and the corresponding dose difference profiles for the right-anterior oblique field. The DTA and the ΔD_{max} criteria of 3 mm and 3%, respectively, were used.

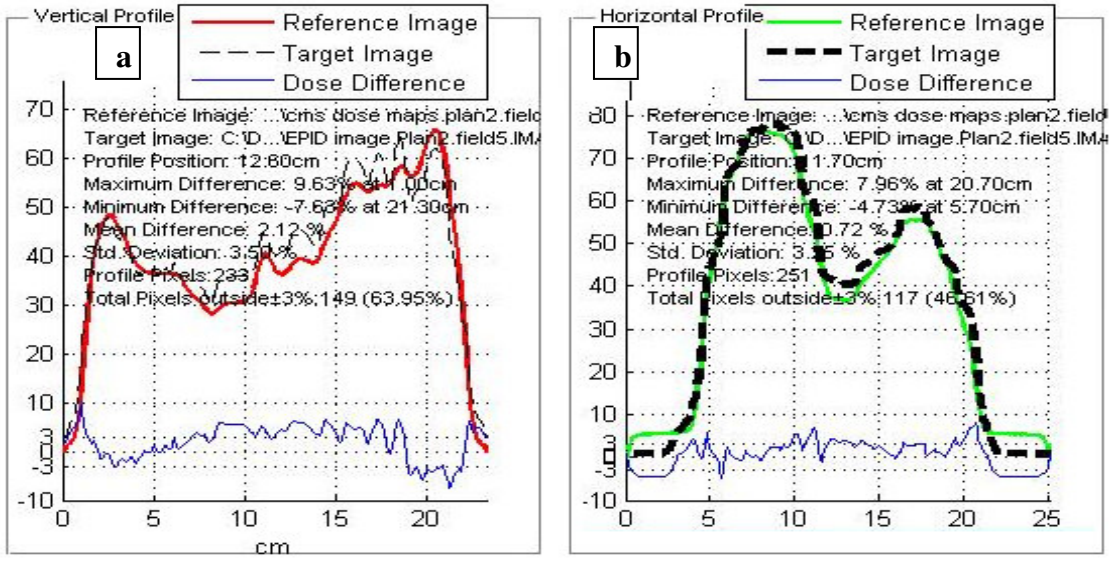

Figure 5.17. (a) vertical and (b) horizontal dose profiles measured and calculated along the lines of the a-Si EPID images and the CMS XiO TPS images and the corresponding

dose difference profiles for the right-posterior oblique field. The DTA and the ΔD_{max} criteria of 3 mm and 3%, respectively, were used.

Table 5.2 shows the IMRT field number with the corresponding mean dose differences that were obtained from the vertical and horizontal dose profiles along the calculated and measured dose maps. The maximum values for mean difference for the vertical profile and the horizontal profile were 2.12% and 2.11%, respectively. The variances of the mean dose differences were 0.31 and 0.44 for the vertical and horizontal profiles, respectively. Figure 5.18 shows a summary plot of the comparisons of the measured with the calculated dose maps for the 15 IMRT fields. In this figure, a plot of the mean dose difference versus the IMRT field beam number/field number is presented. In each of the 15 IMRT fields, the mean dose difference agreement met the selected criteria. The regions where the gamma index exceeded 1 were always located around the edges of the fields or in the low dose-gradient region.

Table 5.2. Comparisons of the mean dose difference between the calculated and measured dose maps for the vertical and horizontal dose maps for 15 IMRT fields.

IMRT field number	**Mean dose difference (%)**	
	Vertical profile	**Horizontal profile**
1	1.21	1.82
2	1.64	1.8
3	1.21	1.66
4	2.05	1.29
5	2.12	0.72
6	1.89	0.44
7	0.96	2.11
8	0.44	0.28
9	2.09	0.83
10	0.7	1.4
11	1.07	1.85

12	1.33	0.56
13	1.14	0.01
14	1.79	0.96
15	2.14	1.73

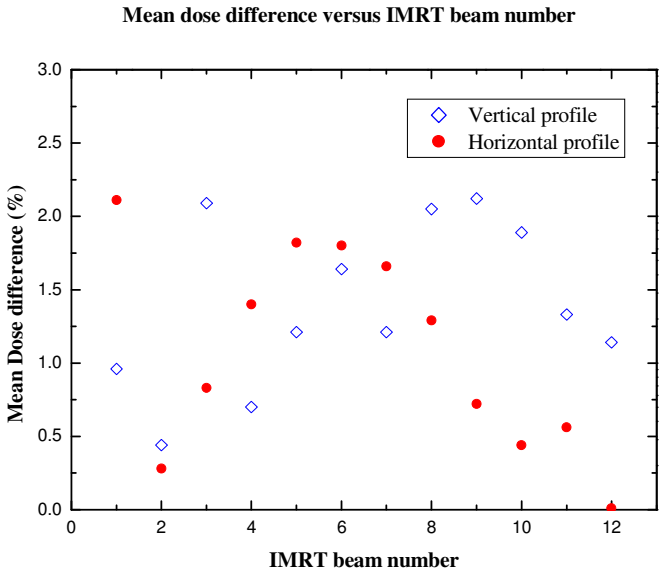

Figure 5.18. The mean dose differences in percentages versus the IMRT field or beam number for the vertical profile (blue dots) and for the horizontal profile (red dots). The DTA and the ΔD_{max} criteria of 3 mm and 3%, respectively, were used.

5.4 Conclusion

IMRT is an increasingly popular technique among radiation therapy treatments. However, due to the complexity of IMRT, sophisticated dosimetric devices are required to verify the treatment delivery. In this work, an amorphous-silicon electronic portal imaging device (a-Si EPID) was used for the IMRT pre-treatment verification. The agreements between the measured and the calculated dose maps with the help gamma function were satisfactory. However, the observed disagreements between the measured and the calculated dose maps (agreement outside the 3%/3mm criteria) occurred at detectors outside of the useful fluence map field. The experimental set-up used for the IMRT pre-treatment verification demonstrated the possibly of using an a-Si EPID for

portal dosimetry. Further work should be done to incorporate the effect of the transmission thickness on the IMRT field to reduce the discrepancy in simulating normal patient set-up. The preliminary results demonstrated the usefulness of the amorphous-silicon electronic portal imaging device (a-Si EPID) as a pre-treatment IMRT QA device for planner dose verification.

6. Absolute dosimetry and monitor unit verifications for intensity-modulated radiation therapy

6.1 Introduction

At the Steve Biko Academic Hospital (SBAH), there are a large number of palliative head-and-neck cases (the most prevalent cancer in males treated in our hospital). We have developed a simple three-field IMRT plan with a concomitant boost that delivers superior dose distribution, is faster and easier to treat and requires fewer fractions than the alternative plan. This saves time and resources. This technique is for the treatment for palliative cases; however a five-field IMRT plan is also used for the radical treatment. However, physical quality assurance must still be performed and can become a bottleneck. Different dosimetric tools have been used for quality control (Low *et al.,* 2001; Ezzell *et al.,* 2003; Bortfeld 2005). A 2D-Array Seven29 ionization chamber has replaced film dosimetry for relative dose distributions (Wiezorek *et al*., 2005; Buonamici *et al.,* 2007). For absolute dosimetry, an ionization chamber has been used to measure the absorbed dose in the IMRT field (Capote *et al*., 2004; Kumar *et al.,* 2007; Leonid *et al.,* 2003; Low *et al.,* 2003; Hugo *et al*., 2004).

Due to the need for efficient tools for IMRT patient-specific QA, experimental methods were and are still commonly used for IMRT plan verification. For this reason, different dosimetric approaches have been used. Although most of the QC has been conducted using experimental methods are; however, time consuming for the physicist, in addition the Linac's need to be used for more time. However, with the increase in inverse planning efficiency, the number of IMRT patients must continually increase; the experimental IMRT verifications methods it may be impractical to check a large number of plans, and it might also affect the workflow. An alternative to the experimental method is the independent MU calculation method. MU verifications from the inverse planning system represent a problem. Therefore, an alternative method is being sought to replace the absolute dose measurements to speed up the process. Different methods have been used for the monitor unit (MU) calculations in IMRT verifications using independent computer programs. Xing *et al.* (2000) developed a computer algorithm for the

verification of MLC leaf sequences and derived a formula for MU calculations for IMRT by using a simple scatter-summation algorithm. Boyer *et al.* (1999) investigated some of the theoretical aspects of MU calculations for an intensity-modulated field. Their approach was independent of the specific form of leaf sequence algorithms. Another method used to verify the MU calculation in IMRT treatment is to sum the fractional MUs that correspond to the segmented fields. A modified Clarkson integration method was used to determine the dose at a given point in the patient (Kung *et al.,* 2000).

The aim of this work is to develop a novel approach for monitor unit calculations and to check the feasibility of replacing the absolute dosimetry method in our department. The MU check program calculates the average area product and uses this to estimate the MU for each field in the IMRT plan. The resultant MUs are used to calculate an equivalent dose based on a conventional MU check program. Because the dose is non-uniform, the calculated dose cannot be compared to the prescribed dose. A volume-weighted average dose of various target volumes is calculated from the DVH and is compared to the calculated dose.

6.2 Theory

In radiotherapy, several factors such as, radiation type, beam energy, calculation algorithm, the field size, irregularity of the treatment field, field-shaping device (blocks, MLC), the depth-to-dose reference point and the beam modifiers are used to determine whether the calculated MUs are realistic (Stern *et al*., 2011). However, in IMRT, conventional monitor unit calculations cannot be performed because of the complexity of the beamlets. One solution is to calculate the dose to only a single point; however, this approach gives very limited information and simply tests the planning system. In this novel approach, attempts are made to use the contribution from each beamlet and bring it in line with the doses in the whole target through the dose volume histogram (DVH).

The basic premise of an MU checking program is that the dose that is deposited in a tumor volume is given by the incident energy minus the energy departing the volume divided by the mass of the volume. This principle can be used to calculate the delivered

energy per field to the target volume. The energy deposited in the whole volume of the target(s) can then be estimated by applying the normal planning principles of attenuation. However, because the dose distribution in the target(s) is non-uniform, this total energy cannot be compared to the prescribed dose. However, the dose volume histogram can be used to determine the average dose per target. Because the volume of each target is known, we can estimate the total energy deposited in the target(s) as determined by the TPS. These two values should be closely related.

Let us consider the energy passing through an area due to a field segment; the fluence can be converted to the total energy delivered by the segment. From the definition by Podgorsak *et al*. (2004), the energy fluence Ψ, is the quotient of dE over dA , where dE is the radiant energy incident on a sphere of cross-sectional area dA . Thus, the energy fluence is

$$\psi = {dE}/{dA}\left(\text{J/m}^2\right) \quad \text{.....(6.1)}$$

Hence, energy is the product of the energy fluence and the area $\left(dE = \psi dA\right)$.

The total energy available for deposition by a segment is proportional to the MU (Khan 2003), thus;

$$E \alpha MU \quad \text{.....(6.2)}$$

Taking into considerations the scatter contributions from the incident photon fluence per MU, which is changes with the change of the collimator settings; equations 6.2 can be written as:

$$E = MU \times A \times S_c \left(m^2\right) \quad \text{.....(6.3)}$$

when the scatter in the patient is not considered. Because the scatter inside the patient is made up of all the contributions from each segment, it is reasonable to assume that the total energy deposited to $d_{\max}$ is the sum of the equation (6.3) for all the segments multiplied by the phantom scatter for the whole patient.

Assuming that there are k segments in the treatment t field, we have

$$E_{tot} = \left(\Sigma_s^K MU_s \times A_s \times S_c\left(A_s\right)\right) S_p\left(A_{tot}\right)\left(MU.m^2\right) \quad \text{.....(6.4)}$$

where

MU_s is the monitor units for segment S ,

A_s is the area of segment S ,

S_c is the in-air output ratio (Zhu *et al.,* 2009), and

S_p is the phantom scatter.

An additional term, E_{trans} , is needed to account for the dose transmitted through the collimators, which will be accounted for later. This energy can be compared to that deposited in the target(s). However, to make this calculation more intuitive, we prefer to determine the number of MUs that must be given to a standard 10 × 10 cm^2 field to deposit the same amount of energy:

$$MU_{avg} = \frac{\left[\left[\left(\Sigma_s^K MU_s \times A_s \times S_c\left(A_s\right)\right)\right] S_p\left(A_{tot}\right) + E_{trans}\right]}{A_{tot} \times S_{p,c}(10)} \quad \text{.....(6.5)}$$

Most beamlets are smaller than 10 × 10 cm^2, $S_c\left(A_s\right) < 1$. As a first approximation, we can argue that the transmitted energy makes up for this; therefore, we can remove the term E_{trans} and replace $S_c\left(A_s\right)$ with $S_c\left(A_{tot}\right)$:

$$MU_{avg} = \frac{\Sigma_s^K MU_s \times A_s \times S_{p,c}\left(A_{tot}\right)}{A_{tot}} \left(MU.m^2 \Big/ m^2\right) \quad \text{.....(6.6)}$$

where A_{tot} is the total area, and $A_{tot} < \Sigma_s^K A_s$ because of the beamlet overlap.

The average MUs for the various fields can be plugged into a conventional MU spreadsheet to determine the average dose received by the target(s).

This calculated dose can be compared with the delivered dose at the target volume ($D_{t\,\mathrm{arg}et}$). Multiple target volumes are often used in IMRT; therefore, the deposited dose at the target volume ($D_{dp-t\,\mathrm{arg}et}$) can be deduced from the dose volume histograms (DVHs) by looking at the 50% dose (D^{50}) or the mean dose with a corresponding volume for the different target volumes.

$$D_{dp-t\,\mathrm{arg}et} = \left(\Sigma D_t^{50} \times V_t\right) \Big/ \left(\Sigma V_t\right) \left({}^{(J\,/\,Kg).Kg}\!\Big/_{Kg} \right) \quad \text{.....(6.7)}$$

Where

$D_{dp-t\,\mathrm{arg}et}$ is the deposited dose at the target volume,

D_t^{50} is the mean dose at the of the target t, and

V_t is the volume of the target t.

(In addition, there must be no target volume overlap).

6.3 Materials and methods

6.3.1 IMRT plans used

Three consecutive head and neck cancer cases were used. The plans were generated by using the CMS XiO treatment planning system (TPS) and consisted of three isocentric fields. There were up to three targets to allow for concomitant boosts. The radiation source was a Siemens ONCOR Linac (Siemens Medical solutions, Concord, USA), which utilizes 6 and 15 MV photon beams for IMRT treatment delivery using a step-and-shoot IMRT mode. The Linac was equipped with an OPIFOUCS MLC with 82 leaves and an amorphous silicon electronic portal imaging device (a-Si EPID).

6.3.2 Absolute dose measurements

The absolute dose measurements were performed using a Farmer 0.6-cc ionization chamber type TM 30013 connected to a PTW UNIDOS electrometer (PTW, Freiburg,

Germany) (see figures 6.2 and 6.3). The chamber was inserted into a Gammex RMI solid-water phantom as shown in figure 6.1. The phantom had dimensions of 30×24×24 cm^3. The experimental set-up was analogous to the calculated IMRT plans except for the gantry angle, which was changed to a zero-degree angle to simplify the phantom positioning. A computed tomography (CT) scan of the RMI Gammex solid water IMRT phantom with a Farmer 0.6-cc ionization chamber was taken at 2-mm in the CT scanner and was used to recalculate the plans. For the ionization chamber measurements, the readings were corrected for the temperature and pressure. Measurements were repeated three times separately for each field (in step-and-shoot IMRT). The measured doses were compared with the calculated values at the ionization chamber location. The percentage of the dose difference for each case was calculated as follows:

$$Percentagedifference = \frac{(D_{Calculated} - D_{Measured})}{D_{Calculated}} \times 100\% \text{.....(6.8)}$$

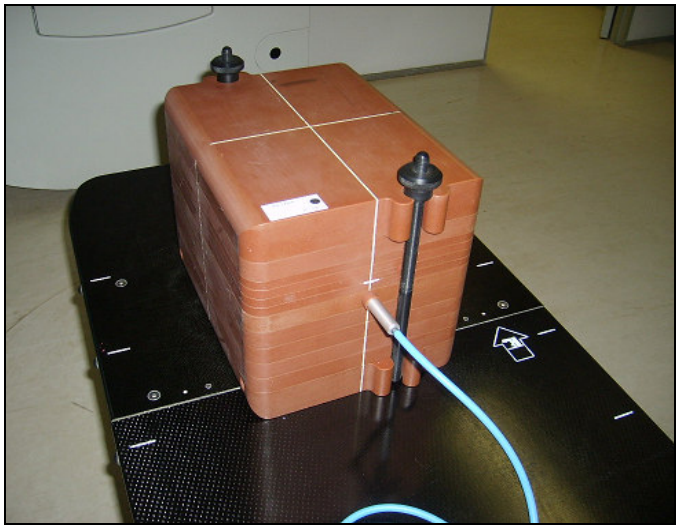

Figure 6.1. The IMRT solid-water phantom (Gammex RMI) that was used for the absolute dose measurements with the Farmer ionization chamber.

Figure 6.2. The PTW UNIDOS electrometer that was used for the absolute dose measurements.

Figure 6.3. The Farmer ionization chamber that was used for the absolute dose measurements.

6.3.3 The monitor unit check program (MUCP)

A computer program was written in Microsoft Visual Basic (VB) programming language (version 3.0). The code read the IMRT plan file as an input file to calculate the MU contributions from each field in the plan. Several parameters, such as the cumulative area MU product, the field area, the normalized MU, the average and the maximum and standard deviation for each field, were calculated. The code also calculated the intensity-level distributions for each field. The results obtained from this program were used as the

input data for the standard MU check spreadsheet to calculate the average dose to the target volume(s).

Instead of comparing the calculated dose to the prescribed dose, the spreadsheet was modified to accept the D_t^{50} doses that were obtained from DVH and the volumes of the target(s). The volume-weighted average dose was thus calculated and compared to the dose that was found from the average MUs.

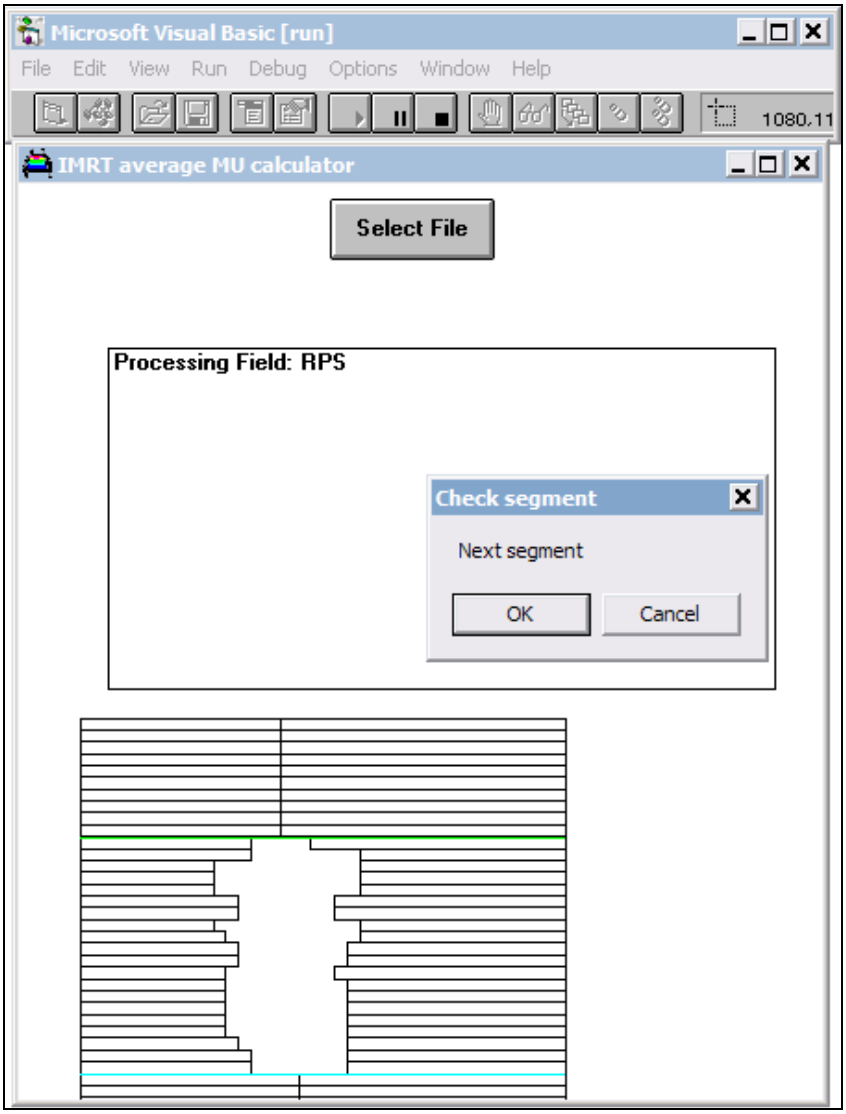

Figure 6.4. A screenshot of the MU calculator for the IMRT window. This window allows the user to view the field segments.

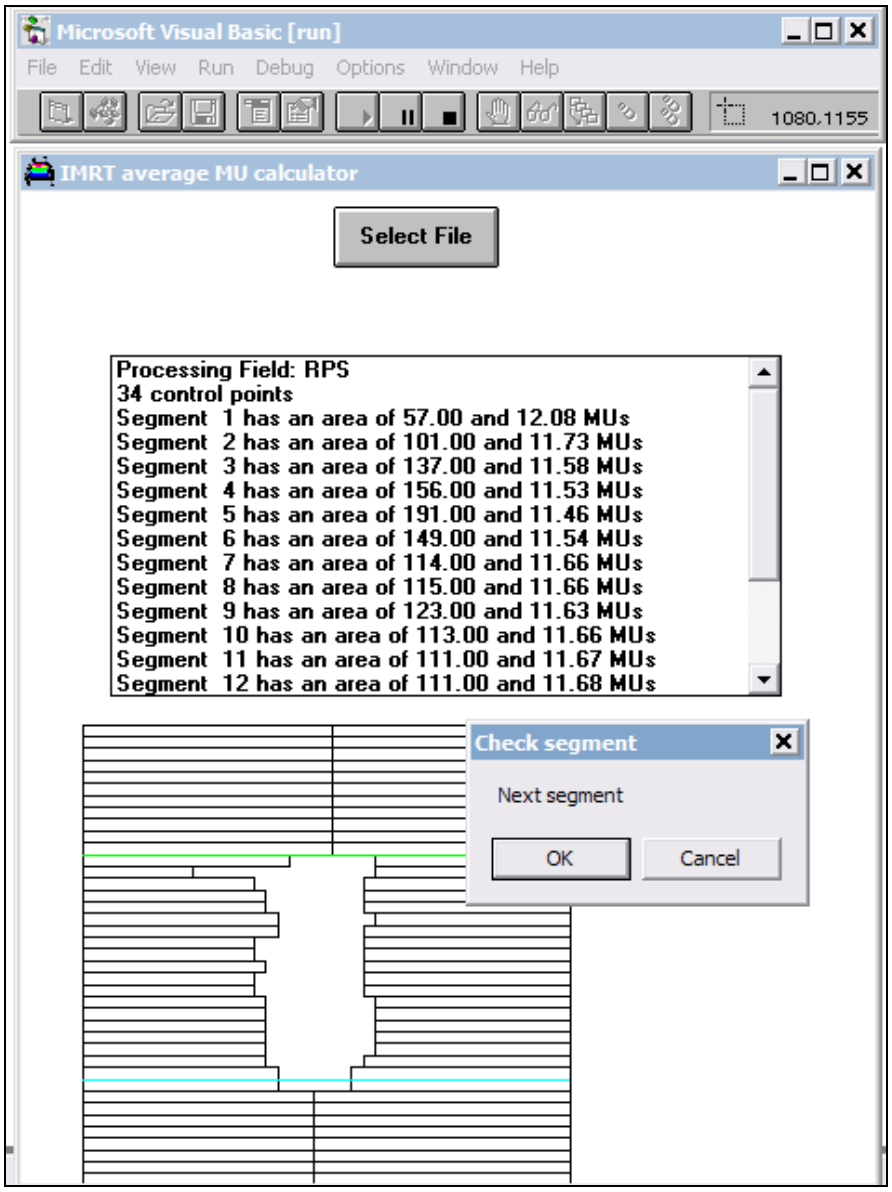

Figure 6.5. A screenshot of the MU Calculator for the IMRT window. This window allows the user to read and calculate the field area and the MU for each segment.

6.4 Results

6.4.1 IMRT plans used

Three IMRT plans consisting of nine IMRT fields with an average of 19 beamlets per field were used.

6.4.2 Absolute dose measurements

Table 1 shows the results obtained for the point dose measurements for the nine IMRT treatment fields. The results show a comparison between the measured and the planned doses for the three IMRT plans. The dose per fraction varied between 1.8 and 2 Gy. The percentage differences between the calculated and measured doses fell between a minimum value of 1.0% and a maximum value of 3.9 %.

Table 1 shows a comparison between the calculated and measured doses for nine IMRT treatment fields; the difference is expressed as a percentage of the field dose {i.e., [100*[(D_{cal}-D_{mes})/D_{cal}]} in column 4.

Treatment field	Calculated dose (cGy) CMS XiO TPS	Measured dose (cGy) ionization chamber	Percentage difference (%)
1	89	88	1.0
2	64	65	1.5
3	91	88	3.3
4	103	102	1.0
5	31	30	3.2
6	103	100	2.9
7	76	73	3.9
8	51	50	2.0
9	72	71	1.4

6.4.3 The monitor unit check program (MUCP)

6.4.3.1 Calculations of the MU_{avg}

MU calculations were conducted for the three IMRT plans. The results of the calculations of the MU data are shown in tables 2, 3 and 4. The cumulative area MU product, the field area, the normalized MU, the average MU, the maximum MU and the standard deviation are given. Figures 6.6 to 6.8 show the intensity-level distributions for the three IMRT plans. Figure 6.9 is an example of the segments making up a single field, whereas in figure 6.10, the fluence map together with its equivalent square field intensity is displayed.

Table 2. The results of the calculations of the MU parameters for the first IMRT plan.

Calculated data Plan (1)	**Field1**	**Field 2**	**Field 3**
Cumulative area MU product	19,212.13	24,985.84	19476.47
Field area	320	460.65	322
Normalized MU	60.04	54.24	60.49
Average MU	60.61	61.19	61.05
Maximum MU	116.81	98.85	134.12
Standard deviation	18.75	21.7	18.57

Table 3. The results of the calculations of the MU parameters for the second IMRT plan.

Calculated data Plan (2)	**Field1**	**Field 2**	**Field 3**
Cumulative area MU product	14153.53	13064.36	14231.20
Field area	221	281	223
Normalized MU	64.04	46.48	63.82
Average MU	64.33	47.29	64.10
Maximum MU	135.89	87.94	151.48
Standard deviation	39.25	18.94	37.34

Table 4. The results of the calculations of the MU parameters for the third IMRT plan.

Calculated data Plan (3)	**Field1**	**Field 2**	**Field 3**
Cumulative area MU product	14903.08	13783.60	12878
Field area	237	240	225
Normalized MU	62.88	57.43	57.24
Average MU	2.88	57.43	57.24
Maximum MU	149.30	115.19	138.90
Standard deviation	32.55	20.73	29.32

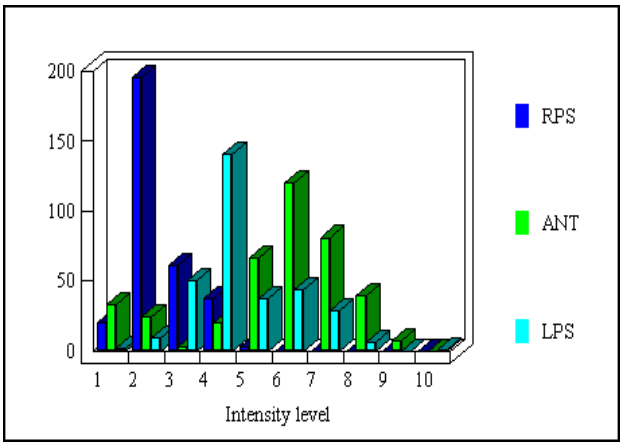

Figure 6.6. The intensity distributions for the first IMRT plan.

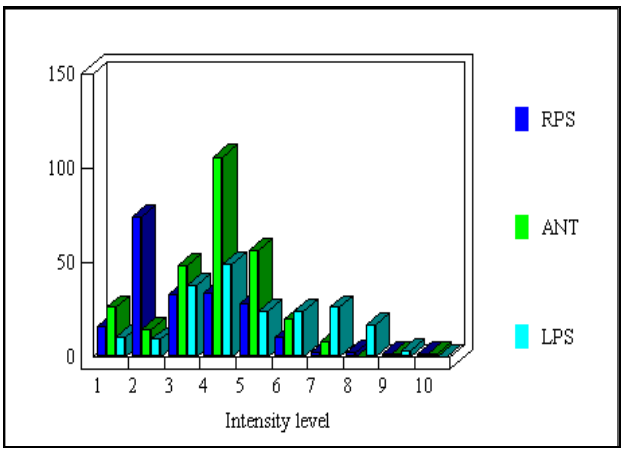

Figure 6.7. The intensity distributions for the second IMRT plan.

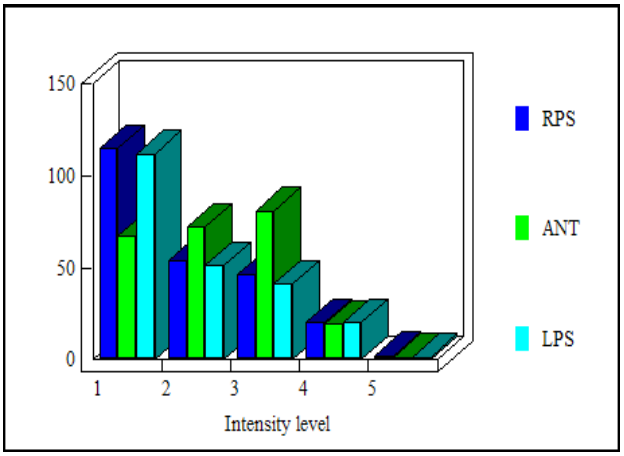

Figure 6.8. The intensity distributions for the third IMRT plan.

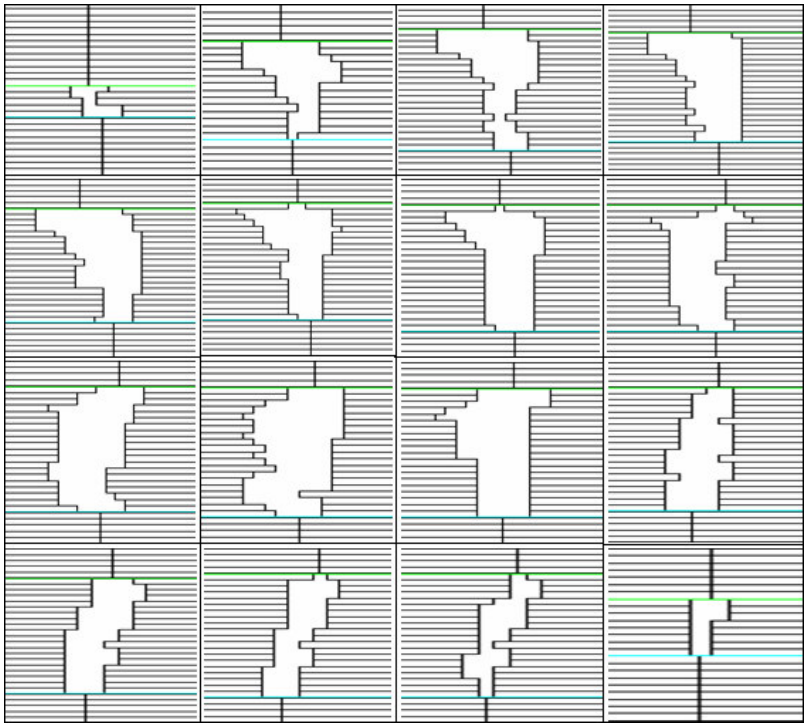

Figure 6.9. An example of the IMRT field segments that are calculated by the MU program. The IMRT fields contain 16 segments.

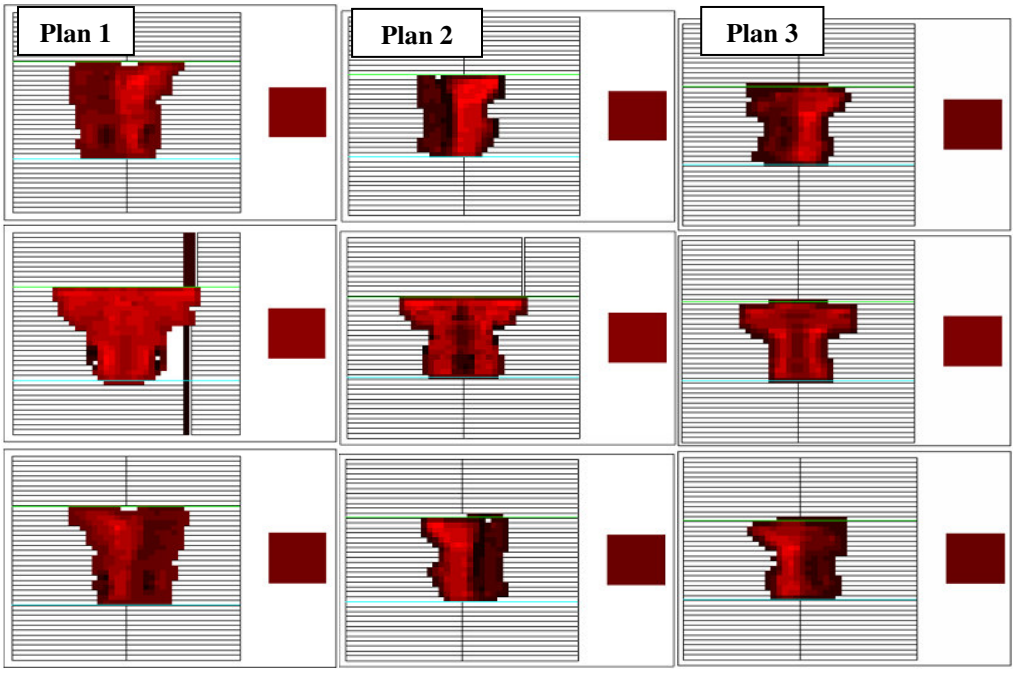

Figure 6.10. The intensity maps for the three IMRT plans. The square on the right represents the calculated average intensity for each field, A, B and C.

6.4.3.2Calculations of D_{target}

All of the IMRT treatment plans used multiple target volumes. The target volumes and the associated mean doses were extracted from the dose volume histograms (DVHs). For each treatment plan, the total volume and the mean dose were used as the input data in the MU verification program. Table 5 shows the results of the extracted data for the three IMRT plans and the target volumes with the delivered mean dose for each. The results also showed that the IMRT plans can contain two or more target volumes.

Table 5. The extracted data from the IMRT plans for the three treatment fields.

IMRT Plan	Target Number	Volume (cc)	Mean Dose (cGy)
Plan 1	Target 1	1239	5310
	Target 2	81.2	5954
Plan 2	Target 1	784.81	5310
	Target 2	30.51	1805
	Target 3	53.96	6446
Plan 3	Target 1	605.60	5687
	Target 2	154.28	6315

6.4.3.3 Dose verifications for the IMRT plans

The doses calculated from the fluences and DVHs were compared. Table 6 shows the results of the verification of the three IMRT treatment plans. Each plan was verified separately for the total dose delivered. The difference was less than 1% for all of the treatment plans. This was obtained by plugging the calculated MU data and the mean dose with the associated volume into the modified MU check spreadsheet.

Table 6. The verification of the doses delivered for three IMRT fields using the MU calculation program.

Plan	Prescribed dose (cGy)	Delivered dose (cGy)	Dose difference (%)
1	214.0	213.7	0.14
2	208.0	207.5	0.24
3	181.6	180.5	0.56

6.5 Discussion and conclusion

IMRT quality control (QC) was performed using absolute dosimetry verifications and a new MU calculation verification method in this study. The absolute dosimetry showed good results for most of the IMRT plans (IMRT treatment fields). The results showed that most of the IMRT fields agreed well with the calculated weighted dose as compared with the measured point doses for each field and fell within an average deviation of approximately 2.4±1.2% and a maximum dose difference of 3.9%. The discrepancies resulted from the heterogeneity of the IMRT fields, and there was a volume averaging effect for the Farmer-type ionization chamber (Low *et al.,* 2003). The MU verification was conducted in two steps. The first step was to calculate MU parameters such as the average MU for the treatment fields, with the standard deviations, and the field's areas using the computer code. For the second step, the obtained results were used as the input data for the verifications of the delivered dose. These parameters were plugged into an MU check spreadsheet to verify the delivered dose. The evaluation of the program showed that the dose calculated by the program agreed well with the does calculated by the planning system. The results of the MU calculation verifications showed better conformance than the absolute dose measurements. This method can therefore safely replace absolute dosimetry in our IMRT quality assurance program.

7. Conclusions and future work

The main purpose of this study was to develop and validate a streamlined patient-specific QA program for IMRT at the Department of Radiation Oncology, Steve Biko Academic Hospital (SBAH). This was realized by several parts of the study that are detailed in chapters 2 to 6.

In chapter 2, the dosimetric characteristics of the 2D-Array Seven29 ionization chamber detector were studied and validated for implementation in IMRT QA. The results showed that the Array signal was very stable, the maximum standard deviation was 0.3%, and during the start-up period, the Array required a pre-irradiation dose of approximately 500 cGy to reach the stable signal. The results demonstrated that the output factor of the Array is linear to the dose response within the range of 2-500 MUs and is dependent on the radiation beam energy in the range of 6 to 15 MV. The output factors matched very well, to within 2%, to the Pin-Point and Farmer ionization chambers under the same experimental conditions. Moreover, the Array had a sensitive detection system design that could detect errors in a range of 2 mm for the MLC leaf system. Finally, for the open and wedge-modulated fields, the Array beam profiles matched the Pin-Point beam profiles that were measured in a water tank. Agreement was within 4% for the large field sizes and was within 3% for small fields. However, there were small discrepancies for the dose profiles for the small field sizes at the edges of the fields. The source of these discrepancies was the sampling capabilities of the Array resulting from the geometric configuration system of the detector. The same results were reported by Spezi *et al.* (2005). Further modifications of the Array design by the manufacturer may eliminate the problem. It is concluded that the 2D-Array Seven29 ionization chamber presents the required characteristics for performing the QA dosimetry for step-and-shoot IMRT deliveries.

The second part of the study (chapter 3) focused on the dosimetric properties of the newly installed a-Si EPID at Steve Biko Academic Hospital and its feasibility to be used for portal dosimetry purposes. The accuracy of portal dosimetry is dependent on the dose-

response characteristics. Without a comprehensive assessment of the dosimetric properties of the a-Si EPID, the a-Si EPID cannot produce reliable dose measurements.

The a-Si EPID signal was highly reproducible; the short-term reproducibility had a maximum standard deviation of 0.3%. The long-term reproducibility was found to be within ±1.7% over a period of 3 months for a 6 MV photon beam. The a-Si EPID response was linear to the applied MUs within the range of 5-100 MUs; the response across the panel became stable for MU greater than 200 MUs, and similar behaviors were reported for the a-Si EPID by Greer *et al.* (2007). Limitations of the a-Si EPID system, such as errors resulting from the saturation of the detector in high MUs, were identified. Therefore, the detector calibration should be conducted within this range. The field-size dependence requires further investigation to understand the optimal calibration for accurate dosimetry. The ghosting effect was not significant, and it was found that 15 sec is a suitable time interval between image acquisitions. The a-Si EPIDs were found to be suitable for measuring relative transmission doses. The intensity of the beam could be decreased when the patient was positioned at the isocenter of the beam, which has an impact on the amount of the dose that reaches the EPID. The calibration procedure outlined in this study has several limitations because it does not include off-axis corrections of the response of the EPID. Furthermore, the calibration model was not accurate enough to be used for absolute dosimetry. However, the a-Si EPID shows promise in use for portal dosimetry after the establishment of a proper calibration model.

In part three (chapter 4), a quantitative evaluation of the IMRT dose distributions using the Kodak EDR2 film and 2D-Array ionization chamber system was performed. The 2D-Array Seven29 detector system results showed that the QA procedure can identify systematic errors that can be rectified. The resultant dose distributions demonstrated that the Array has overall fewer areas that failed to meet the currently used criteria of 3%/3mm dose differences and distance-to-agreement.

The Array showed superior dosimetric behavior to the EDR2 film; the detector is easy to handle and is less time consuming. Therefore, the Array can significantly reduce the time

required to perform measurements, procedures and analyses. Although the resolution of the EDR2 film is unrivaled, the EDR2 film is time consuming and is therefore an impractical dosimetry system for performing IMRT patient-specific QA, especially in a busy department. However, the film is necessary for commissioning an IMRT program, and the 2D-Array Seven29 dosimetry system is ideal for QA after an IMRT system is fully commissioned. EDR2 film introduces many uncertainties in different stages of the experimental procedure (i.e., exposing, developing, scanning and analysis). This could reduce the accuracy of the results. However, more accurate results can be achieved by utilizing proper dosimetric procedures for the EDR2 film. The study concluded that the 2D-Array Seven29 dosimetry system is a practical and reliable dosimetric tool that is also a time-saving detector for patient-specific QA for IMRT. It is recommended that the IMRT patient-specific QA be performed using the 2D-Array Seven29 dosimetry system.

The use of gamma index criteria appears to be arbitrary; therefore, the critical impact of a failure to meet the criteria was investigated by purposely changing the intensity-modulated fluences. When the intensity-modulated fluences were changed to the point where the gamma index failed the plan, the clinician still found the plan to be acceptable. Rather than summarily failing a plan and redoing it when it fails to meet the gamma criteria, we should then rather substitute the measured fluences into the TPS. Only if there is a clinically significant difference should we redo the entire plan.

Part four (chapter 5) investigated the feasibility of using a-Si EPID for IMRT pre-treatment verification. The results showed that the agreement between the measured and the calculated dose maps with the help of the gamma function was acceptable. However, the observed disagreements between the measured and the calculated dose maps (agreement outside the 3%/3mm criteria) occur at the detectors that are outside of the useful fluence map field. The preliminary results demonstrate the usefulness of an amorphous-silicon electronic portal imaging device (a-Si EPID) as a pre-treatment IMRT QA device for planner dose verification. An a-Si EPID can be used to replace the 2D-Array Seven29 dosimetry system when portal dosimetry software is available.

In the last part of this study (chapter 6), an independent monitor unit verification method was developed. The method is intended to be used as an independent verification method for the IMRT patient-specific QA. The accuracy and performance of the independent monitor unit verification method were also investigated. The independent monitor unit check program (MUCP) was found to be simple, fast, easy and accurate enough to be used in routine verifications for head-and-neck IMRT.

The study proposed that the 2D-Array Seven29 dosimetry system and the developed monitor unit check program (MUCP) could be used for our routine IMRT patient-specific QA program. The 2D-Array Seven29 dosimetry system can be used for the IMRT fluence map measurements with reasonable accuracy while maintaining the large number of IMRT plans in our department. When a plan fails to meet the 3%/3 mm criteria for more than 10% of the points inside the field, then the measured fluence must be used to calculate the actual delivered dose, and only if there is a clinically significant deviation from the prescribed plan must it be redone. The monitor unit check program can be used with the help of the absolute dosimetry for the point-dose verification for the step-and-shoot-IMRT deliveries.

Further studies could include the implementation of the a-Si EPID imager as a portal dosimetry tool for IMRT pre-treatment verification. This requires a proper calibration model for the a-Si EPID and portal dosimetry software. This is currently being investigated as a possible follow-up research project.

Summary

Intensity modulated radiation therapy (IMRT) aims to deliver highly conformal radiation doses to the target volume while sparing organs-at-risk (OARs). This can be achieved with the complex motion and irregular shapes of the multi-leaf collimator (MLC) by using inverse treatment planning systems (TPS). Pre-treatment patient-specific quality assurance (QA) has become an essential part of IMRT programs to ensure that the actual dose distributions that are delivered to the target volume (TV) match the doses that are intended for that volume. At Steve Biko Academic Hospital (SBAH), we use IMRT plans for radical as well as for palliative patients to save time and resources because a concomitant boost and simplified set-up can save time per fraction and for the total duration of the treatment. A cumbersome, time-consuming QA step can negate these advantages. The main purpose of this work was to develop and validate a streamlined patient-specific QA program for IMRT at Steve Biko Academic Hospital (SBAH). The IMRT planning was performed on a CMS XiO treatment planning system (TPS) (CMS, XiO, St. Louis, MO, USA) using an inverse planning algorithm to generate the IM photon beams. The treatment was delivered with a Siemens ONCOR Linac (Siemens Medical solutions, Concord, USA) with 6 and 15 MV photon beams for the IMRT treatment delivery and a step-and-shoot IMRT mode. The Linac is equipped with an OPIFOUCS MLC with 82 leaves and an amorphous silicon electronic portal imaging device (a-Si EPID).

Understanding the dosimetric characteristics of the detector is a requirement for any clinical dosimetric application. Therefore, in the first phase of the study, (chapters 2 and 3), the dosimetric characteristics of the 2D-Array Seven29 (PTW, Freiburg, Germany) and the a-Si EPID were investigated. The dosimetric properties of the 2D-array that were investigated included the reproducibility, the linearity and energy dependence, the output factor, the sensitivity and the clinical applications. The dosimetric properties of the a-Si EPID that were investigated included the detector reproducibility, the detector response as a function of the applied MUs, the field-size dependence, the ghosting effect, the build-up effect of the detector, the detector response as a function of the transmission thickness and an investigation of the use of the detector as a dosimeter.

In the second phase of the study (chapters 4 and 5), relative dosimetry for the IMRT fluence maps was performed. In chapter 4; the delivered dose was measured using two different methods: the Kodak EDR2 film dosimetry and the and the 2D-Array Seven29 dosimetry system. In the study, several IMRT plans for the head-and-neck treatment sites were used. The measured relative isodose distributions and the dose profiles of the EDR2 film and the 2D-Array Seven29 were compared to the relative isodose distributions and dose profiles of the CMS XiO TPS IMRT plans. A quantitative evaluation of the IMRT dose distributions was performed with the gamma index method and 3%/3mm criteria. The two techniques were compared on the basis of time efficiency and accuracy. The use of the gamma index criteria appeared to be arbitrary; therefore, the critical impact of a failure to meet the criteria was investigated by purposely changing the intensity-modulated fluences. Chapter 5 investigated the feasibility of using a-Si EPID for IMRT pre-treatment verification. During the last phase, an independent monitor unit verification method was developed and validated by comparing the results with the absolute dosimetry using a dedicated IMRT QA phantom (Gammex RMI, Middleton, WI) with a Farmer 0.6-cc ionization chamber. The MUCP uses the patient plan with a specific format as the input data. The program simply calculates the average dose area product. This yielded MUs for the equivalent fields, which were then plugged into a standard MU verification program. The calculated dose was compared to the volume-weighted average of the various target volumes from the dose volume histogram (DVH).

The dosimetric characterizations of the 2D-Array Seven29 ionization chamber showed its suitability for use as a dosimetric tool in IMRT verifications. The overall results show that the 2D-Array is more accurate and time efficient than the Kodak EDR2 film for IMRT pre-treatment verification. When the intensity-modulated fluences were changed to the point at which the gamma index failed to meet the criteria for the plan, the clinician still found the plan to be acceptable. The EPID signal was reproducible; the long-term reproducibility was found to be within ±1.7% over a period of 3 months for a 6 MV photon beam. The a-Si EPID demonstrated a good response to the applied monitor units, and the field-size dependence was acceptable. The ghosting effect for the period of time for the image acquisition was negligible for the short time interval of 15 seconds. A

comparison of the relative transmission measurements between the EPID and the ion chamber indicated maximum deviations of 10% and 4.5% at 6 and 15 MV, respectively. However, when the EPID-measured dose maps were compared with the calculated doses from the TPS using the gamma index at a 3% dose difference (DD) and a 3-mm distance-to-agreement (DTA), an agreement (gamma index less ≤ 1.0) of 90% or more was found for the IMRT fields. The preliminary results demonstrate the usefulness of an amorphous-silicon electronic portal imaging device (a-Si EPID) as a pre-treatment IMRT QA device for planner dose verification. For the IMRT absolute dosimetry, the deviations between the ionization chamber measurements and the calculated weighted doses showed an average deviation of approximately 2.4±1.2% and a maximum deviation of 3.9% among the IMRT fields. The dose deviations between the MUCP and the TPS were 0.14, 0.24 and 0.56% for the three IMRT plans. The average deviations were 0.31±0.21%. However; the total dose deviation was approximately 4%.

The 2D-Array Seven29 ionization chamber proved that it has desirable dosimetric characteristics and can effectively be used for IMRT patient-specific QA; however, the a-Si EPID requires further investigation before it can be used as a tool for portal dosimetry purposes. Close agreement between the 2D-Array measured dose and the TPS calculated dose distributions was obtained. There were noteworthy deviations between the TPS and 2D-Array doses on the field edges. However, it should be emphasized that the 2D-Array is a time-efficient tool. It is concluded that a combination of a 2D-Array dosimetry system and a monitor unit check program (MUCP) is an accurate and convenient method for IMRT patient-specific QA. Rather than rejecting a plan and redesigning it when it fails to meet the gamma criteria, we should substitute the measured fluences into the TPS. Only if there is a clinically significant difference should we redesign the entire plan.

Keywords: IMRT, quality assurance, TPS, EDR2 film, 2D-Array, a Si-EPID, monitor units (MUs), absolute dosimetry

“There is no region of regret when the dose you see is the dose you get."(Peter Metcalfe 1994)”

References

AAPM, 1997. Code of practice for brachytherapy physics: Report of the AAPM radiation therapy committee task group no. 56. *Med. Phys*. **24**, 1557–98.

AAPM., Task Group 53., 1998. Quality assurance for clinical radiotherapy treatment planning.*Med. Phys.***25**, 1773-1829.

Aldridge, J.S., Harari, P.M., Reckwerdt, P.J., Olivera, G.H., Tom´e, W., Fink, M.B., 1999. Development of conformal avoidance tomotherapy in the treatment of head and neck cancer.*Int. J. Radiat. Oncol.Biol. Phys*. **45**(Suppl. 1) 245.

Aldridge, J.S., Shepard, D.M., Mackie, T.R., Reckwerdt, P., 1998. Conformal avoidance radiation therapy.*Radiother.Oncol*.**48**, (Suppl. 1).S76.

Althof, V.G,, de Boer, J.C., Huizenga, H., Stroom, J.C., Visser, A.G., Awnenburg, B.N., 1996. Physical characteristics of a commercial electronic portal imaging device.*Med. Phys.***23**, 1845-55.

Amerio, S., Boriano, A., Bourhaleb, F., Cirio, R., Donetti, M., Fidanzio, A., Garelli, E., Giordanengo, S., Madon, E., Marchetto, F., Nastasi, U., Peroni, C., Piermattei, A., Sanz Freire, C.J., Sardo, S., Trevisiol E.E., (2004).Dosimetric characterization of a large area pixel-segmented ionization chamber.*Med. Phys.***31**, 414–20.

Antonuk, L.E., 2002. Electronic portal imaging devices: a review and historical perspective of contemporary technologies and research. *Phys. Med. Biol.***47**, 31–65.

Antonuk, L.E., El-Mohri, Y., Huang, W., 1998.initial performance evaluation of an indirect –detection, active matrix flat-panel imager (AMFPI) prototype for megavoltage imaging. *Int. J. Rad. Oncol. Biol. Phys.***42**, 437-54.

Arbea, L., Ramos, L.I., Martinez-Monge, R., Moreno, M., Aristu, J., 2010. Intensity-modulaed radiation therapy (IMRT) vs. 3D conformal radiotherapy (3DCRT) in locally advanced rectal cancer (LARC): dosimetric comparison and clinical implications. *Rad. Oncol.***5**, 17-23.

Armstrong, J.G., Burman, C., Leibel, S., Fontenla, D., Kutch, G., Zelefsky, M., Fuks, Z., 1993. Three dimensional conformal radiation therapy may improve the therapeutic ratio of high dose radiation therapy for lung cancer. *Int. J. Rad. Oncol. Biol. Phys.* **26**, 685-689.

Arnfield, M.R., Wu, Q., Tong, S., Mohan, R., 2001. Dosimetric validation for multileaf collimator-based intensity-modulated radiotherapy: a review.*Med. Dosim.* **26**, 179-188.

Basran, P.S., Woo, M.K., 2008. An analysis of tolerance levels in IMRT quality assurance procedures. *Med. Phys*. **35**, 2300- 2307.

Bedford, J. L., Young, K.L., Wai, P., Christopher, P.S., Warrington, A.P., 2009.Evaluation of the Delta4 phantom for IMRT and VMAT verification.*Phys. Med. Biol*. **54**, (9): N167–76.

Bortfeld, T., 2006. IMRT: A review and preview. *Phys. Med. Biol.* **51**, 363–379.

Bouchard, H., Lacroix, F., Beaudoin, G., Jean-François, C., Kawrakow, I., 2009. On the characterization and uncertainty analysis of radiochromic film Dosimetry. *Med. Phys*. **36**, 1931- 1946.

Bourland, J.D., McCollough, K.P., 1994. Static field conformal stereotactic radio-surgery: Physical techniques. *Int. J. Rad. Oncol. Biol. Phys.***28**, 471-479.

Boyer, A.L., Xing, L., Ma, C., Curran, B., Hill, R., Kinia, A., Bleier, A., 1999. Theoretical considerations of monitor unit calculations for intensity modulated beam treatment planning. *Med. Phys.***26**, 187-89.

Brahme, A., 1988. Optimization of stationary and moving beam radiation therapy techniques.*Radiother.Oncol*.**12**, 129–140.

Bucciolini, M., Buonamici.F.B., Casati, M., 2004. Verification of IMRT fields by film dosimetry. *Med. Phys.***31**,161–168.

Budgell, G.J., Perrin, B.A., Mott, J.H.L., Fairfoul, J., Mackay, R.I., 2005.Quantitative analysis of patient-specific dosimetric IMRT verification.*Phys.Med. Biol.***50**,103–119.

Buonamici, F.B., Compagnucci, A., Marrazzo, L., Russo, S., Bucciolini, M., 2007.An intercomparison between film dosimetry and diode matrix for IMRT quality assurance.*Med. Phys.***34**, 372-1379.

Cadman, P., Sidhu, N.P.S., 2000. Feasibility of penumbra compensating filters for conformal prostate radiotherapy. *Phys. Med. Biol.***45**, 295-304.

Capote, R., Sanchez-Dobaldo, F., Leal, A., Lagares, J.I., Arrans, R., 2004.An EGSnrc Monte Carlo study for the microionization chamber for reference dosimetry of narrow irregular beamlets.*Med. Phys.***31**, 2416-2422.

Cardinale, R.M., Kavanagh, B.D., 2000. Conformal radiotherapy: what is it and why does it matter? *Surg. Oncol. Clin. N. Am.* **9**, 415-34.

Carol, M., Peacock, P., 1995.A system for planning and rotational delivery of intensity-modulated fields.*Int. J. Imag. Sys. Tech.* **6**,56-61.

Chang, J., Mageras, G.S., Chui, C.S., Ling, C.C., Lutz, W., 2000. Relative profile and dose verification of intensity-modulated radiationtherapy.*Int. J. Rad. Oncol. Biol. Phys.***47**, 231-40.

Chen, J., Chuang, C.F., Morin, O., Aubin, M., Pouliot, J., 2006. Calibration of an amorphous –silicon flat panel portal imager for exit-beam dosimetry. *Med. Phys.***33**, 3095-105.

Cheng, B., Komanduri, M., Weining, Z., Robert, B., Charles, A., 2002.Commissioning and quality assurance for MLC-based IMRT.*Med. Dosim.* **26**, 125–133.

Chen-Shou, C., Spiridon, V., 2001. Inverse Planning Algorithms For External Beam Radiation Therapy. *Med. Dosim.* **26**, 189–197.

Childress, N.L., Rosen, I.I., 2004. Effect of processing time delay on the dose response of Kodak EDR2 film.*Med. Phys.* **31**, 2284-2288.

Childress, N.L., Salehpour, M., Dong, L., Bloch, C., White, A.R., Rosen, I.I., 2005.Dosimetric accuracy of Kodak EDR2 film for IMRT verifications.*Med. Phys.***32**, 539-548.

Chu, R.D.H., Van Dyk, J., Lewis, D.F., O'Hara, K.P.J., Buckland, B.R., Dinelle, F., 1990 GAFCHROMIC® dosimetry media: A new high dose rate thin film routine dosimeter and dose mapping tool. *Radiat. Phys. Chem.* **35**, 767-773.

Cormack, A.M., 1987. A problem in rotation therapy with X–rays.*Int .J. Radiat.Oncol. Biol. Phys.* **13**, 623–630.

De Boer, J.C., Heijmen, B.J., Pasma, K.L., Visser, A.G., 2000. Characterization of a high-elbow.Fluoroscopic electronic portal imaging device for portal dosimetry.*Phys. Med. Biol.***45**, 197-216.

De Martin, E., Fiorino, C,, Broggi, S., Longobardi, B., Pierelli, A., Perna, L., Cattaneo, G.M., Calandrino, R., 2007. Agreement criteria between expected and measured field fluences in IMRT of the head and neck cancer: the importance and use of the gamma histograms statistical analysis. *Radiother.Oncol.***85**,399–406.

Depuydt, T., Van Esch, A., Huyskens, D., 2002. A quantitative evaluation of IMRT dose distributions: refinement and clinical assessment of the gamma evaluation. *Radiother.Oncol.***62**, 09–19.

Devic, S., Seuntjens, J., Hegyi, G., Podgorsak, E.B., Soares, C.G., Kiron, A.S., Ali, I., Williamson, J.F., Elizondo, A., 2004. Doismetric propretrites of improved GafChromic films films for seven different digitizers. *Med. Phys.***31**, 2392-2401.

Devic, S., Seuntjens, J., Sham, E., Podgorsak, E.B., Kirov, A.S., Schmidtlein, R.C., Soares, C.G., 2005. Precise radiochromic film dosimetry using a flat-bed document scanner.*Med. Phys.***32**, 2245-2253.

Didinger, B.H., Schlegel, W., Dedus, J., 2002. Intensity-modulated radiotherapy - technology and clinical applications.*Onkologie*.**25**, 233-238.

Dogan, N., Leybovich, L.B., Sethi, A., 2002. Comparative evaluation of Kodak EDR2 and XV2 films for verification of intensity modulated radiation therapy. *Phys. Med. Biol.***47**, pp.4121–4130.

El-Mohri, Y., Antonuk, L.E., Yorkston, J., 1999.Relative dosimetry using active matrix flat-panel imager (AMFPI) technology.*Med. Phys.***26**, 1530-41.

Essers, M., Hoogervorst, B.R., van Herk, M., Lanson, H., Mijneer, B.J., 1995. Dosimetric characteristics of a liquid-filled electronic portal imaging device.*Int. J. Rad. Oncol. Biol. Phys.***33**, 1265-72.

Ezzell, G.A., Burmeister, J.W., Dogan, N., LoSasso, T.J,, Mechalakos, J.G., Mihailidis, D., Molineu, A., Palta, J.R., Ramsey, C.R., Salter, B.J., Shi, J., Xia, P., Yue, N.J., Xiao, Y., 2009. IMRT commissioning: Multiple institution planning and dosimetry comparisons, a report from AAPM Task Group 119. *Med. Phys*. **36**, 5359–5373.

Ezzell, G.A., et al., 2003. IMRT Sub-committee, AAPM Radiation Therapy Committee. Guidance document on delivery, treatment planning, and clinical implementation

of IMRT: report of the IMRT Subcommittee of the AAPM Radiation Therapy Committee. *Med. Phys.***30**, 2089–2115.

Feygelman, V.,Forster, K., OppDaniel, Nilsson G., 2009.Evaluation of a biplanar diode array dosimeter for quality assurance of step-and-shoot IMRT.*J. Appl. Clin. Med. Phys*. **10**, 64–78.

Fraass, B.A., 1995. The development of conformal radiotherapy.*Med. Phys.***22**, 1911-21.

Francescon, P., Cora, S., Chiovati, A., 2003. Dose verification of an IMRT treatment planning system with BEAM EGS4-based Monte Carlo code.*Med. Phys*. **30**, 144-147.

Franken, E.M., de Boer, J.C., Barnhoorn, J.C., Heijman, B.J., 2004. Characteristics relevant to portal dosimetry for a cooled CCD camera-based EPID. *Med. Phys.***31**, 2549-51.

Franken, E.M., de Boer, J.C., Heijman, B.J., 2006. A novel approach to accurate portal dosimetry using CCD-camera based EPIDs. *Med. Phys.***33**, 888-903.

Gale, A.A., Jain, A.K., Vallow, L.A., Serago, C.F., Buskirk, S.J., Heckman, M.G., 2009. Cardiac dose evaluation for 3Dimensional conformal partial breast irradiation compared with whole breast irradiation. *J. Appl. Clin. Med. Phys*. **10**, 3–13.

Geinita, H., Zimmermann, F.B., Thamm, R., Schumertl, A., Busch, R., Molls, M., 2005.3D conformal radiation therapy for prostate cancer in elderly patients.*Radiother.Oncol.***76**, 27-34.

Glendinning, A.G., Bonnett, D.E., 2000. Dosimetric properties of the Theraview flourscopic electronic portal imaging device.*Br. J. Radiol.***73**, 517-30.

Graham, M.V., Mathews, J.W., Harms, W.B. S.R, Emami, B., Glazer, H.S., Purdy, J.A., 1994. Three dimensional Radiation treatment planning study for patients with carcinoma of the lung. *Int. J. Radiat. Oncol. Biol. Phys.***29**, 1105-17.

Greer, P.B., Popescu, C., 2003. Dosimetric properties of an amorphous silicon electronic portal imaging device for verification of dynamic intensity modulated radiation therapy. *Med. Phys.***30**, 1618–1627.

Greer, P.B., 2007. Off-axis dose response characteristics of an a-Si electronic portal imaging device. *Med. Phys.***34**, 3815-24.

Greer, P.B., Barnes, M.P., 2007. Investigation of an amorphous silicon EPID for measurement and quality assurance of enhanced dynamic wedge. *Phys. Med. Biol. 52*, 1075–1087.

Greer, P.B., Vial, P., Oliver, L., Baldock, C., 2007. Experimental investigation of the response of an amorphous silicon EPID to intensity modulated radiotherapy beams. *Med. Phys.***34**, 4389–98

Grein, E.E., Lee, R., Luchka, K., 2002. An investigation of a new amorphous silicon electronic portal imaging device for transit dosimetry.*Med. Phys.***29**, 2262–2628.

Gutiérrez, A.N., Calvo, O., 2010. Diode Arrays and QA of Advanced Techniques.*J. Phys.*: *Conf. Ser*. **250** 01249.

Heijmen, B.J., Pasma, K.L., Kroonwijk, M., Altohof, V.G.M., 1995. Portal dose measurement in radiotherapy using an electronic portal imaging device (EPID) *Phys. Med. Biol.***40** 1943-1955.

Herzen, J., Todorovic, M., Cremers, F., Platz, V., Albers, D., Bartels, A., Schmidt, R., 2007.Dosimetric evaluation of a 2D pixel ionization chamber for implementation in clinical routine.*Phys. Med. Biol.***52**, 1197-1208.

Howell, R.M., Smith, I.P.N., Jarrio, C.S., 2008. Establishing action levels for EPID-based QA for IMRT.*J. Appl. Clin. Med. Phys.***9**,16–25.

Hugo, B., Seuntjens, J., 2004. Ionization chamber-based reference dosimetry of intensity modulated radiation beams. *Med. Phys.***3**, 2454-2465.

IAEA., 2004. *Review of Radiation Oncology Physics: A Handbook for Teachers and Students*. International Atomic Energy Agency, Educational Report Series, Vienna.

IMRT., Collaborative Working Group., 2001. Intensity-modulated radiation therapy: current status and issues of interest. *Int. J. Radiat. Oncol. Biol. Phys*. **51**, 880–914.

Jacob, V., Kneschaurek, P., 2008.A Method for Improved Verification of Entire IMRT Plans by Film Dosimetry.*Strahlenther.Onkol.***185**, 34-40.

Janathan, G.L., Guanghua, Y., Chihray, L., 2009. Comparison of two commercial detector arrays for IMRT quality assurance.*J. Appl. Clin. Med. Phys.***10**, 62-74.

Ju, G., Ahn, Y.C., Huh, S.J., Yeo, I.J., 2002. Film dosimetry for intensity modulated radiation therapy. *Med. Phys.***29**, 351–355.

Jursinic, P.A., Nelms, B.E., 2003. A 2-D diode array analysis software for verification of intensity modulated radiation therapy delivery. *Med. Phys.* **5**, 870-879.

Jursinic, P.A., Sharma, R., Reuter, J., 2010. MapCHECK used for rotational IMRT measurements: Step-and-shoot, Tomotherapy, RapidArc. *Med. Phys*. **37**, (6): 2837–2846.

Karzmark, C.J., 1984. Advances in Linear Accelerator Design for Radiotherapy.*Med. Phys.* **11**, 105 128.

Karzmark, C.J., Pering, N.C., 1973. Electron linear accelerators for radiation therapy: history, principles and contemporary developments. *Phys. Med. Biol*. **18**, 321–54.

Kavuma, A., Glegg, M., Currie, G., Elliott, A., 2008.Assessment of dosimetrical performance in 11 Varian a-Si500 electronic portal imaging devices.*Phys. Med. Biol.***53**, 6893-6909.

Kavuma, A., Glegg, M., Metwaly, M., Currie, G., Elliott, A., 2010. A novel method for patient exit and entrance dose prediction based on water equivalent path length measured with an amorphous silicon electronic portal imaging device. *Phys. Med. Biol.***55**, 435–452.

Khan, F.M., 2003.*The Physics of Radiation Therapy 3rd ed*. Lippincott Williams and Wilkins, Philadelphia.

Kumar, A., Mukherjee, G., Yadav, G., Pandey, V., Bhattacharya, K., 2007. Optimized dose measurement: An effective tool for QA in intensity –modulated radiotherapy. *Med. Phys.***32**, 156-160.

Kung, J.H., Chen, G.T.Y., Kuchnir, Z.K., 2000. A monitor unit verification calculation in intensity modulated radiotherapy as a dosimetry quality assurance. *Med. Phys.* **27**, 2226-2230.

L´etourneau, D., Gulam, M., Yan, D., Oldham, M., Wong, J.W., 2004.Evaluation of a 2D diode array for IMRT quality assurance.*Radiother.Oncol.***70**, (2): 199–206.

Leonid, B., Leybovich, S.A., Dogan, N., 2003.Comparison of ionization chambers of various volumes for IMRT absolute dose verifications.*Med. Phys.***30**, 119-123.

Li, J.G., Yan, G., Liu, C., 2009. Comparison of two commercial detector arrays for IMRT quality assurance.*J. Appl. Clin. Med. Phys.***10**, 62-74.

Ling, C.C., Humm, J., Larson, S., Amols, H., Fuks, Z., Leibel, S., Koutcher, J.A., 1995. Towards multidimensional radiotherapy (MD-CRT): biological imaging and biological conformality. *Int. J. Rad. Oncol. Biol. Phys*. **47**, 551–560.

LoSasso, T., Chui, C.S., Ling, C.C., 2001. Comprehensive quality assurance for the delivery of intensity modulated radiotherapy with a multileaf collimator used in the dynamic mode. *Med. Phys*. **28**, 2209–2219.

Louwe, R.J., Tielenburg, R., van Ingen, K.M., Mijneer, B.J., van Herk, M.B., 2004. The stability of liquid-filled matrix ionization chamber electronic portal imaging devices for dosimetry purposes.*Med. Phys.***31**, 819-27.

Low, D.A,, William, B.H., Mutic, S., Purdy, A.J., 1998. A technique for quantitative evaluation of dose distributions.*Med. Phys.***25**, 656-661.

Low, D.A., Dempesy, F.J., 2003. Evaluation of the gamma dose distribution comparison method.*Med. Phys.***30**, 2455-2464.

Low, D.A., Gulam, M., Yan, D., Oldham, M., Wong, J.W., 2003.Evaluation of 2D diode array for IMRT quality assurance.*Radiother.Onco*. **70**, 199-206.

Low, D.A., Moran, J.M., Dempsey, J.F., Dong, L., Oldham, M., 2011.Dosimetry tools and techniques for IMRT.*Med. Phys*. **38**, 1313-1338.

Low, D.A., Parikh, P., Dempsey, J.F,, Wahab, S., Huq, S., 2003. Ionization chamber volume averaging effects in dynamic intensity modulated radiation therapy beams. *Med. Phys.* **30**,1706-17011.

MacKenzie, M.A., Lachaine, M., Murray, B., Fallone, B.G., Robinson, D., and Field, G.C., 2002. Dosimetric verification of inverse planned step and shoot multileaf collimator fields from a commercial treatment planning system. *J. Appl. Clin. Med. Phys*. **3**, 97–109.

Mackie, T.R., Kapatoes, J., Ruchala, K., Lu, W., Wu, C., Olivera, G., 2003. Image guidance for precise conformal radiotherapy.*Int. J. Rad. Onco. Biol. Phys*. **56,**89–105.

Manuel, A.M., Coffey, C.W., Ding, G.X., 2011. Evaluation of the dynamic conformal arc therapy in comparison to intensity-modulated radiation therapy in prostate, brain, head-and-neck and spine tumors.*J. Appl. Clin. Med. Phys.***12**, 5–16.

Mark, R., Qiuwen, W., Shidong, T., d Radhe, M., 2001. Dosimetric Validation For Multileaf Collimator-Based Intensity-Modulated Radiotherapy: A Review. *Med. Dosim*. **26**, 179–188.

Martens, C., De Wagter, C., De Neve, W., 2000.The value of the PinPoint ion chamber for characterization of small field segments used in intensity-modulated radiotherapy. Phys. Med. Biol. **45**, 2519–30.

Martens, C., De Wagter, C., De Neve, W., 2001.The value of the LA48 linear ion chamber array for characterization of intensity-modulated beams.*Phys. Med. Biol.***46**, 1131–48.

Masi, L., Casamassima, F., Doro, R., Francescon, P., 2011. Quality assurance of volumetric modulated arc therapy: Evaluation and comparison of different dosimetric systems. *Med. Phys*. **38**, 612-621.

McCurdy, B.M.C., Luchka, K., Pistorius, S., 2001. Dosimetric investigation and portal dose image prediction using an amorphous silicon electronic portal imaging device. *Med. Phys.***28**, 911–924.

McDermott, L.N., Nijsten, S.M., Sonke, J.J., Partridge, M., van Herk, M., Mijnheer, B.J., 2006. Comparison of ghosting effects for three commercial a-Si electronic portalimaging devices.*Med. Phys.***33**, 2448-2451.

McDermott, L.N., Wendling, M., Sonke, J-J., Van Herk, M., Mijnheer, B.J., 2007. Replacing pretreatment verification with in vivo EPID dosimetry for prostate IMRT.*Int. J. Radiat. Oncol. Biol. Phys.***67**,1568–1577.

McDermott, L.N., Wendling, M., Van Asselen, B., Stroom, J., Sonk,e J-J., Van Herk, M., Mijnheer, B.J., 2006. Clinical experience with EPID dosimetry for prostate IMRT pre-treatment dose verification.*Med. Phys.***33**,3921–3930.

McDermott, N.L., Louwe, R.J., Sonke, j.j., van Herk, M., Mijnheer, B.J., 2004.Dose-response and ghosting effects of an amorphous silicon electronic portal imaging device.*Med. Phys.***31**, 285–295.

McDermott, N.L., Nijsten, S., Sonke, j.j., Partridge, M., van Herk, M., Mijnheer, B.J., 2006. Comparison of ghosting effects for three commercial a-Si EPIDs.*Med. Phys.***33**, 2448–2451.

McDonald, S.M., Ahmed, S., Kachris, S., Vogds, B.J., DeRouen, M., Gitttleman, A.E., 2007. Intensity modulated radiation therapy versus three- dimensional conformal radiation therapy for treatment of high grade glaucoma: a dosimetric comparison. *J. Appl. Clin. Med. Phys*. 8, 47-56.

Meertens, H., van Herk, M., Bijhold, J., Bartelink, H., 1990. First clinical experience with a newly developed electronic portal imaging device.*Int. J. Rad. Oncol. Biol. Phys.***18**, 1173-81.

Mell, L.K., Roeske, J.C., Mundt, A.J., 2003. A survey of intensity-modulated radiation therapy use in United States.*Cancer*.**98**, 204- 211.

Menon, G.V., Sloboda, R.S., 2004. Compensator thickness verification using an a-Si EPID. *Med. Phys*.**31**, 2300-12.

Metcalfe, P., Kron, T., Hoban, P., 1997.*The Physics of Radiotherapy X-Rays from Linear Accelerators*.Medical Physics Publishing, Madison, Wisconsin.

Mohan, R., 1998. 3D conformal radiation therapy—Part 4: optimized intensity-modulated three-dimensional conformal radiation therapy. *Int. J. Radiat. Oncol. Biol. Phys*. **42**, (Suppl.) 113.

Mohan, R., 1999. Intensity-modulated radiotherapy—Part 2: radiobiological aspects. *Int. J. Radiat. Oncol.Biol. Phys.***45**, (Suppl. 1) 128–9.

Mohan, R., 2006. Field shaping for three-dimensional conformal radiation therapy and multileaf collimation.*Semin.Oncol*.**5**, 86-99.

Moran, J.M., 2010.Use of Electronic Portal Image Detectors for Quality Assurance of Advanced Treatment.*J. Phys*.: *Conf. Ser*. **250** 012021.

Nelms, B.E., Simon, J.A., 2007. A Survey on Planar IMRT QA Analysis.*J. Appl. Clin. Med. Phys.***8**, 76-90.

Nicolini, G., Fogliata, A., Vanetti, E., Clivio, A., Vetterli, D., 2006b. GLAaS: An absolute dose claibrtaion algorthim for an amorphous silicon portal imager. Applications to IMRT verifications.*Med. Phys.***33**, 2839-2851.

Nicolini, G., Vanetti, E., Clivio, A., Fogliata, A., Boka, G., Cozzi, L., 2006a. Testing the portal imager GLAas algorithm for machine quality assurance.*Radia.Oncol.***3**, 1-20.

Nijsten, S., Mijnheer, B.J., Dekker, A., Lambin, P., Minken, A., 2007b. Routine individualized patient dosimetry using electronic portal imaging devices.*Radiother.Oncol.***83**, 65-75.

Nijsten, S., Minken, A., Lambin, P., Bruinvis, A.I., 2004.Verfication of treatment parameter transfer by means of electronic portal dosimetry.*Med. Phys.* **31**, 341-7.

Nijsten, S.M.J.J., Van Elmpt, W.J.C., Jacobs, M., Mijnheer, B.J., Dekker, A.L.A.J., Lambin, P., Minken, A.W.H., 2007a. A global calibration model for a-Si EPIDs used for transit dosimetry. *Med. Phys.***34**, 2872-2884.

Olch, A.J., 2002. Dosimetric performance of an enhanced dose range radiographic film for intensity-modulated radiation therapy quality assurance. *Med. Phys.***29**, 2159-2168.

ONCOR Impression, Physics Operator manual, Siemens Medical Solutions USA, Inc.

Palta, J.R., Liu, C., Li, J.G., 2008b. Quality assurance of intensity-modulated radiation therapy.*Int. J. Radiat. Oncol.Biol. Phys.***71**, S108-112.

Palter, J.R., Mackie, T.R., 2003. *Intensity–modulated radiation therapy: the state of the art.*Medical Physics Publishing, Madison.

Partridge, M., Hesse, B-M., Muller, L., 2002.A performance comparison of direct-and indirect-detection flat panel imager.*Nucl.Instrum. Methods .Phys. Res.*A .**48**, 351-63.

Pasma, K.L., Kroonwijk, M., de Boer, J.C.J., Visser, A.G., Heijmen, B.J., 1998.Accurate portal dose measurement with a fluoroscopic electronic portal imaging device (EPID) for open and wedged beams and dynamic multileaf collimation.*Phys. Med. Biol.***43**, 2047–2060.

Pawlick, T., Yoo, S., Court, L.E., McMillan, R.K., Russell, J.D., 2008. Process control analysis of IMRT QA: implications for clinical trial. *Phys. Med. Biol*. **53**, 5193-5205.

Pecharromán-Gallego, R., Mans, A., Sonke, J., Stroom, J.C., Olaciregui-Ruiz, Í., Van Herk, M., Mijnheer, B.J., 2011. Simplifying EPID dosimetry for IMRT treatment verification.*Med. phys*. **38**, 983-992.

Pollack, A., Zagars, G.K., Rosen, I.I., 1999. Prostate Cancer Treatment with Radiotherapy: Maturing Methods That Minimize Morbidity. *Semin.Oncol.***26**, 150-61.

Poppe, B., Blechschmidt, A., Djougulela, A., Kollhof, R., Rubach, A., willborn, K., Harder, D., 2006. Two- dimensional ionization chamber arrays for IMRT plan verification. *Med. Phys.***33**, 1005- 1015.

Poppe, B., Djougulela, A., Blechschmidt, A., willborn, K., Ruhmann, A., Harder, D., 2007. Spatial resolution of 2D ionization chamber arrays for IMRT doe verification: single-detector size and sampling step width. *Med. Phys. Biol*. 52, 2921-2935.

Purdy, J.A., 1999. 3D treatment planning and intensity-modulated radiation therapy.*Semin.Radiat.Oncol.***9**, 78-98.

Rangel, A., Palte, G., Dunscombe, P., 2010. The sensitivity of patient-specific IMRT QC to systematic MLC leaf bank offset errors. *Med. Phys*. **37**, 3862- 3867.

Robertson, J.M., Ten Haken, R.K., Hazuka, M.B., Turrisi, A.T., Martel, M.K., Pu, A.T., 1997. Dose escalation for non-small cell lung cancer using conformal radiation therapy.*Int. J. Rad. Oncol. Biol. Phys.* **37**,1079-85.

Sabet, M., Menk, F.W., Greer, P.B., 2010. Evaluation of an a-Si EPID in direct detection configuration as a water-equivalent dosimeter for transit dosimetry. *Med. Phys*. **37**, 1459–1467.

Sadagopan, R., Bencomo, J.A., Martin, R.L,, Nilsson, G., Matzen, T., Balter, P.A., 2008. Characterization and clinical evaluation of a novel IMRT quality assurance system.*J. Appl. Clin. Med. Phys.***10**, 104- 119.

Sakhalkar, H.S., Sterling, D., Adamovics, J., Ibbott, G., Oldham, M., 2009.Investigating the Feasibility of 3D Dosimetry in the RPC IMRT H&N Phantom.*J. Phys.*: *Conf. Ser*. **164** 012058.

Sannazzari, G.L., Ragona, R., Ruo Redda, M.G., Giglioli, F.R., Isolato, G., Guarneri, A., 2002. CT-MRI image fusion for delineation of volumes in three-dimensional conformal radiation therapy in the treatment of localized prostate cancer.*Br. J. Radiol.* **75**, 603 – 607.

Schulz, R.J. 1999. Further improvements in dose distributions are unlikely to affect cure rates. *Med. Phys.***26**, 1007–9.

Spezi, E., Angelini, A.L., Roman, F., Ferri, A., 2005.Characterization of a 2D ion chamber array for the verification of radiotherapy treatments.*Phys. Med. Biol.***50**, 3361–3373.

Spirou, S., Chui, C., 1994. Generation of arbitrary intensity profiles by dynamic jaws or multileaf collimators. *Med. Phys*. **21**, 1031-1041.

Stasi, M., Giordanengo, S., Cirio, R., Boriano, A., Bourhaleb, F., Cornelius, I., Donetti, M., Garelli, E., Gomola, I., Marchetto, F., Porzio, M., Sanz Freire, C.J., Sardo, A., Peroni, C., 2005. D-IMRT verification with a 2D pixel ionization chamber: dosimetric and clinical results in head and neck cancer. *Phys. Med. Biol.***50**, 4681-4694.

Stathakis, S., 2010. Ionization chamber array for patient specific VMAT, Tomotherapy and IMRT QA.*J. Phys.*: *Conf. Ser*. **250** 012029.

Talamonti, C., Casati, M., Bucciolini, M., 2006.Pretreatment verification of IMRT absolute dose distributions using a commercial a-Si EPID.*Med. Phys.***33**, 4367–4378.

Tateoka, K., Ouchi, A., Waka, M., 2006.Dosimetric properties of the liquid ionization chamber electronic portal imaging device (EPID).Igaku.Bustsuri.**26**, 28-38.

Touboul, E., Foulquier. J.N., 1996.Three-dimensional radiation therapy.Report of the "2nd International Symposium 3-D Radiation Treatment Planning and Conformal Therapy".*Bull. Cancer.Radiother.***83**,187-95.11-13 April. Saint-Louis, Missouri, USA.

Touboul, E., Lefkopoulos, D., 1994. Three-dimensional radiation therapy.Report of 3D radiation treatment planning and conformal therapy. An international symposium 21-23 April 1993 Saint-Louis, Missouri, USA, *Bull. Cancer.Radiother.***81**,7-21.

Two Dimensional Array Seven29 user's manual, PTW, Freiburg, Germany.

Van Dyk, J., 2005. *The Modern Technology in Radiation Oncology: A compendium for Medical Physicist and Radiation Oncologists.1st edition. II*. Medical Physics Publishing, Madison, Wisconsin.

Van Dyk, J., Barnett, R.B,, Cygler, J.E,, Shragge, P.C., 1993. Commissioning and quality assurance of treatment planningcomputers.*Int. J. Radiation Oncology Biol Phys*: 26, 261-273.

Van Elmpt ,W., Ezzell, G.A., Orton, C.G., 2009. EPID dosimetry must soon become an essential component of IMRT quality assurance. POINT/COUNTERPOINT.*Med. Phys*.**36**, 4325-4327.

Van Elmpt, W., McDermott, L., Nijsten, S., Wendling, M., Lambin, P., Mijnheer, B., 2008. A literature review of electronic portal imaging for radiotherapy dosimetry.*Radiother.Oncol*.**88**, 289–309.

Van Elmpt, W., Nijsten, S., Mijnheer, B.J., Dekker, A., Lamb, A., 2008b. The next step in patient-specific QA: 3D dose verification of conformal and intensity-modulated RT based on EPID dosimetry and Monte Carlo dose calculations *Radiother. Oncol*.**86,** 86–92.

Van Esch, A., Bohsung, J., Sorvari, P., 2002. Acceptance tests and quality control (QC) procedures for the clinical implementation of intensity modulated radiotherapy (IMRT) using inverse planning and the sliding window technique: experience from five radiotherapy departments. *Radiother.Oncol*.**65**, 53–70.

Van Esch, A., Depuydt, T., Huyskens, D.P., 2004.The use of an aSi-based EPID for routine absolute dosimetric pre-treatment verification of dynamic IMRT fields.*Radiother.Oncol*.**71**, 223–234.

Van Herk, M., 1991.Physical aspects of a liquid-filled ionization chamber with pulsed polarizing voltage.*Med. Phys*.**18**, 692-702.

Van Zijtveld M, Dirkx, M., De Boer, H.C.J., Heijmen, B.J.M., 2006.Dosimetric pre-treatment verification of IMRT using an EPID; clinical experience.*Radiother.Oncol*.**81**, 168–175.

Van Zijtveld, M., Dirkx, M., Breuers, M., De Boer, H., Heijmen, B., 2009.Portal dose image prediction for in vivo treatment verification completely based on EPID measurements.*Med. Phys*. **36**, 946–952.

Van Zijtveld, M., Dirkx, M.L.P., De Boer, H.C.J., Heijmen, B.J.M., 2007.3D dose reconstruction for clinical evaluation of IMRT pretreatment verification with an EPID.*Radiother.Oncol*.**82**, 201– 207.

Vanderstraeten, B., De Gersem, Duthoy W., De Neve, W., Thierens, H., 2006. Implementation of biologically conformal radiation therapy (BCRT) in an algorithmic segmentation-based inverse planning approach. *Phys. Med. Biol*. **51**, 277-286.

VeriSoft Operator Manual, version 2.11, PTW-Freiburg.

Wambersie, A., Gahbauer, R.A., 2001. Hadrons (protons, neutrons, heavy ions) in radiation therapy: rationale, achievements and expectations. *Radiochim.Acta*.B, 245–53.

Wang, C., Dai, J., Hu, Y., 2003. Optimization of beam weights for conformal radiotherapy using mixed integer programming. *Phys. Med. Biol*. **48**, 4065-4076.

Warkentin, B., Steciw, S., Rathee, S., Fallone, B.G., 2003.Dosimetric IMRT verification with a flat-panel EPID.*Med. Phys*.**30**, 3143–3155.

Webb, S., 1989. Optimization of conformal dose distributions by simulated annealing. *Phys.Med. Biol*. **34**, 1349- 1370.

Webb, S., 1998.Advances in treatment with intensity-modulated conformal radiotherapy Tumor.**84**,112–26.

Webb, S., 2001a.*Intensity Modulated Radiation Therapy*. *2nd ed.* Institute of Physics Publishing, Bristol, Philadelphia.

Webb, S., 2001b.A simple method to control aspects of fluence modulation in IMRT planning.*Phys. Med. Biol*. **46**, 187–195.

Webb, S., 2003.The Physical basis of IMRT and inverse planning.*Br. J. Radiol.* **76**, 678-689.

Wendling, M., Louwe, R.J., McDermott, L.N., Sonke, J.J., Van Herk, M., Mijnheer, B.J., 2006. Accurate two-dimensional IMRT verification using a back-projection EPID dosimetry method.*Med. Phys*. **33**, 259–273.

Wendt, T.G., Abbasi-Senger, N., Salz, H., Pinqurt, I., Koscielny, S., Przetak, S., Wiezorek, T., 2006. 3D-Conformal intensity modulated radiotherapy with compensators for head and neck cancer: clinical results of normal tissue sparing. *Radia.Oncolo*.**2**, 1-7.

Wiezorek, T., Banz, N., Schwedas, M., Scheithauer, M., Salz, H., Georg, D., Wendt, T.G., 2005. Dosimetric Quality Assurance for Intensity-Modulated Radiotherapy: Feasibility Study for a Filmless Approach. *Strahlenther.Onkol.***7**, 468-474.

Williamson, J.F., Thomadsen, B.R., Nath, R., 1995. *Brachytherapy Physics*. Eds. Madison (WI): Medical Physics Publishing.

Winkler P, Zurl B, Guss H, Kindl P, Stuecklschweiger G (2005). Performance analysis of a film dosimetric quality assurance procedure for IMRT with regard to the employment of quantitative evaluation methods.*Phys. Med. Biol.***50**, 643–654.

Winkler, P., George, D., 2006. An intercomparison of 11 a-Si electronic portal imaging devices of the same type: implications for portal dosimetry. *Phys. Med. Biol.***51**, 4189-200.

Winkler, P., Hefner, A., George, D., 2005. Dose-response characteristics of an amorphous silicon EPID. *Med. Phys.***32**, 3095–3105.

Winkler, P., Hefner, A., George, D., 2007. Implementation and validation of portal dosimetry with an amorphous silicon EPID in the energy range from 6 to 25 MV. *Phys. Med. Biol.* **52**, N355–N365.

Xia, P., Verhey, L.J., 2001. Delivery systems of intensity-modulated radiotherapy using conventional multileaf collimators.*Med. Dosim*. **26**, 169–177.

Xing, L., Jonathon, G.L., 2000. Computer verifications of fluence map for intensity modulated radiation therapy. *Med. Phys.***27**, 2084-2092.

Yan, G., Liu, C., Simon, T.A., Peng, L., Fox, C., Li, J.G., 2009. On the sensitivity of patient-specific IMRT QA to MLC positioning errors.*J. Appl. Clin. Med. Phys.***10**, 120- 128.

Yang, Y., Xing, L., 2005. Twoards biologically conformal radiation therapy (BCRT): selective IMRT dose escalation under the guidance of spatial biology. *Med. Phys*. **32**, 1473-84.

Yeo, I.J., Beiki-Ardakani, A., Cho, Y.B., 2004. EDR2 film dosimetry for IMRT verification using low-energy photon filters. *Med. Phys.***31**,1960–3.

Young, R., Snyder, B., 2001. IMRT (intensity modulated radiation therapy): progress in technology and reimbursement. *Radiol. Manage*. **23**, 20-26.

Zabel, A., Thilmann, C., Zuna, I., Schlegel, W., Wannenmacher, M., Debus, J., 2002. Comparison for forward planned conformal radiation therapy and inverse planned intensity modulated radiation therapy for esthesioneuroblastoma. *Br. J. Radiol.* ***75****, 356-361.*

Zeidan, O.A., StacyAnn, L.S., Sanford, L.M., Thomas, H.W., Twyla, R.W., Patrick, A.K., Katja, M.L., 2006. Characterization and use of EBT radiochromic film for IMRT dose verification. *Med. Phys*. **33**, (11): 4064–4072.

Zelefsky, M.J., Leibel, S.A., Gaudin, P.B., Kutcher, G.J., Fleshner, N.E., Venkatramen, E.S., 1995. Dose Escalation With Three-Dimensional Conformal Radiation Therapy Affects The Outcome In Prostate Cancer. *Int. J. Radiat. Oncol. Biol. Phys.***41**,491-500.

Zhu, X.R., Yoo, S., Jursinic, P.A., Grimm, D.F., Lopez, F., Rownd, J.J., Gillin, M.T., 2003. Characteristics of sensitometric curves of radiographic films, *Med. Phys.***30**, 912–919.

Zhu, T.C., et al 2009. In-air output ratio, S_c, for megavoltage photon beams. Report of AAPM Therapy Physics Committee. *Med.phys*.**36,** 5261-5291.